Deformation and micromechanics of granular materials in shear zones - investigated with the Discrete Element Method

Dissertation

zur Erlangung des Doktorgrades der Naturwissenschaften am Fachbereich Geowissenschaften der Universität Bremen

submitted for the doctoral degree in natural sciences at the Faculty of Geosciences of Bremen University

vorgelegt von

by

Ingo Kock

Bremen,
Januar/January 2007

Tag des Kolloquiums:

11.05.2007

Gutachter:

Prof. Dr. Katrin Huhn
Prof. Dr. Achim Kopf

Prüfer:

Prof. Dr. Michael Schulz
Prof. Dr. Heinrich Villinger

General outline and remarks

This thesis consists primarily of three manuscripts that have already been published or are currently under review by international scientific journals. These are Chapter I to Chapter IV. Furthermore, Chapter V is a published manuscript which was prepared in collaboration with Prof. Dr. K. Huhn and Prof. Dr. A. Kopf, and to which I contributed.

In the following sections and chapters, nomenclature is kept consistent. There is a distinction between ‘grain’ and ‘particle’. Grain is used in connection with natural samples and conditions, whereas particle refers to numerical specimens.

Chapter I outlines the general motivation for this thesis. The concepts of friction, failure of soil and rocks, and laboratory methods to evaluate shear strength are briefly introduced. One main goal of Chapter I is to review state-of-the-art scientific concepts necessary to place this thesis into a wider framework and beyond the scope of a single manuscript. Only then can specific objectives of an individual manuscript be outlined. Lastly, the numerical modelling technique is briefly presented, followed by the model and interpretation techniques I have developed myself.

The fact that the roughness of country rock and of geotechnical shear test walls does have an influence on localization patterns and shear strength of soil/fault gouge is demonstrated in **Chapter II.** When roughness is scaled by the maximum particle size of a sample, we show that there are threshold levels of roughness, below and above which shear becomes extremely localized. In between these thresholds, shear is distributed throughout the specimen.

Chapter III explores the effects of particle shape on the deformation behaviour of a numerical modelled ‘clay’ sample. Two key factors, sphericity and roughness, could be identified as relevant to frictional strength, shear zone development, and particle rotation with sphericity dominating over roughness.

In **Chapter IV** the concept of Chapter III is broadened. Here, the deformation behaviour of micro-sized layered stratigraphic units of modelled ‘silt’ and ‘clay’ is analyzed. We show that different deformation modes (sliding, rolling and rotation of particles) lead to different overall

frictional strength and localization phenomena. The ability of single particles to slide, roll or rotate is influenced by particle friction contrast.

Chapter V is a comparative study of numerical modelling and geotechnical/analogue tests. The presence and the concentration of clay minerals are major factors controlling the shear behaviour of sedimentary materials.

The last **Chapter VI** summarizes results and conclusions of previous chapters and connects these aspects to some concepts of Chapter I. Then, advantages and limitations of the numerical method are discussed. Lastly, an outlook of necessary future work is presented.

Abstract

This thesis was inspired by the lack of detailed (i.e. particle scale) knowledge concerning deformation processes of mechanically weak sediments, especially intrinsically weak layers on the basal shear plane of submarine landslides. It has been known for some time that many different parameters influence shear strength and localization features. This is true not only for sediments, but also for other kinds of weak layers, such as fault gouge. These parameters include for example mineralogy (e.g. smectite, illite, quartz), sediment composition (clay, silt), sediment structure and texture (microfabric), grain size distribution, excess pore pressure, magnitude of effective stress, and deformation history. However, to date it has not been possible to rank or to quantify the influence of each of these parameters. The main goal of this study is to analyze the influence of some of these parameters and, if possible, rank and quantify them.

Standard methods to examine shear strength of sediments and fault gouge are various geotechnical shear experiments. In these, a sample is sheared under defined conditions and resulting coefficient of friction, void ratio change, and other meaningful parameters are analyzed. Unfortunately, it is not possible to 'look' inside a shear box during a test and to analyze grain deformation behaviour on a microscopic scale. Therefore, this study employs a different approach to specifically address the problem of microscopic deformation processes. Here, a numerical modelling technique, the Discrete Element Method (DEM), is used.

The DEM is a numerical tool based on the behaviour of granular materials. Within some limitations, soils and fault gouge can be considered as granular. Thus, the DEM allows simulating deformation behaviour of weak layers. The DEM principle is based upon simple physical contact and motion laws and can reproduce a wide range of grain features and behaviour. The technique has already been used to model other kinds of granular deformation processes such as large and small scale deformation processes.

Utilizing the DEM a numerical shear box, very similar to geotechnical ring shear tests, was designed. Inside this box, a variety of different numerical 'samples' were generated. These 'sediments', or 'fault gouges', were designed with close specifications in each study (manuscript), respectively. During the numerical experiments a multitude of micromechanical parameters (particle displacement and rotation, microfabric evolution, coordination number,

sliding fraction, contact force distribution and orientation) were measured. These also encompass classical geotechnical measurements, such as coefficient of friction, void ratio or volume change.

It was not possible to study all parameters which might influence deformation. Therefore, the manuscripts concentrated on the study of:
(1) Surface roughness. This is suspected to have at least a second order influence on frictional strength. But so far it has been extremely difficult to study surface roughness systematically, mainly due to irreproducible boundary conditions in the laboratory.
(2) Clay particle shape. Geotechnical tests suggest that the shape of clay minerals has a strong impact on the deformation behaviour. The manuscript focuses on two aspects of particle shape: sphericity and roughness.
(3) Clay and silt stratification. It is unknown where exactly, single grain displacement accumulates in a sample during deformation in a complex layered setting. Thus, a detailed investigation of micromechanical particle deformation in such a setting was carried out.
(4) Clay and silt mixing. A well-known geotechnical relationship between clay fraction and frictional strength was tested numerically to validate and asses the comparability between laboratory and numerical shear box experiments.

Comparison between numerical and geotechnical experiments implied that results from numerical models could be applied to natural conditions, albeit with some limitations. As geotechnical data reflect, parameters (1) - (4) did have an influence on the microscopic deformation behaviour of sediments and fault gouge.
In Chapter II, threshold levels for boundary roughness are presented. Below a threshold boundary roughness of 0.25, low roughness led to low boundary and sample friction followed by complete mechanic decoupling of the boundary. Above a threshold level of 4, high roughness led to low boundary but high sample friction. The boundary could not decouple but a concentrated shear zone developed in its vicinity. Intermediate roughness between these levels led to intermediate frictional strength of the sample, but to highest friction for the boundary. Deformation inside the sample was distributed.
In the next chapter (Chapter III) particle sphericity and roughness could be identified as key parameters for deformation behaviour and localization. Microfabric development is controlled by particle interlocking and rotation. Since increasing roughness caused increasing particle interlocking, microfabric breakdown during shear was prevented and shear zone development

precluded. In contrast, breakdown of complex initial microfabric was enhanced by decreasing particle sphericity. This caused particle rotation to preferred angles, which resulted in low friction and increasing shear zone localization.

Subsequently, two types of layered specimens were studied in Chapter IV: (1) A ’silt’-’clay’-’silt’ assemblage and (2) a ‘clay’-‘clay’-‘clay’ package. Here, the contrast between particle friction of two layers was discovered to have a high impact on deformation behaviour. Differences in particle friction contrast controlled whether the dominant mode of granular deformation was particle sliding, rolling or rotation. When deformation mode changed inside the sample, localization features also varied. Overall localization structures were very similar to features found in nature and laboratory. Y-, P- and R_1 type shear planes were particularly abundant in the numerical ‘clay’ where also a distinct correlation between slip planes localization and particle alignment could be found.

The comparison of numerical and geotechnical experiments in Chapter V revealed clay size fraction to be an important control on frictional strength. With both methods a threshold value of 50% could be identified as the minimum amount of clay size fraction to induce a significant decrease in frictional strength in a sediment. Here, it was demonstrated that the combination of laboratory and numerical experiments allow to classify the influence of parameters controlling frictional strength, particularly since shear plane monitoring with the DEM allowed a direct control of the shear localization in all materials.

At the end of this thesis a ranking order of every single parameter is presented. In this ranking, it is important to distinguish between purely numerically derived conclusions and their implication for natural materials. Hence, within model limitations, grain roughness and clay size fraction exhibit maximum influence on frictional strength and localization of sediments and fault gouge. The impact of boundary surface roughness is smaller; followed by grain sphericity. The influence of stratigraphic layering is difficult to place into this ranking as it has a different impact in different settings.

Zusammenfassung

Die vorliegende Arbeit wurde dadurch angeregt, dass das Verständnis von Deformationsprozessen in mechanisch schwachen Sedimenten weiterhin lückenhaft ist, wenn man den Partikelmaßstab zugrunde legt. Dies gilt speziell für Schichten an der Basis von Abscherhorizonten submariner Rutschungen, deren Scherfestigkeit immanent ist. Seit längerer Zeit ist bekannt, dass die Scherfestigkeit und die Lokalisation der Scherflächen von vielen unterschiedlichen Faktoren abhängig sind. Dies gilt nicht nur für Sedimente, sondern auch für Störungsletten. Diese Faktoren beinhalten unter anderem die Mineralogie (Smektit, Illit, Quarz), die Sedimentzusammensetzung (Ton, Silt), die Sedimentstruktur und -textur (Mikrogefüge), die Kornverteilung, Porenüberdrucke, die Größe des effektiven Drucks und die vorhergegangen Deformationspfade. Es ist bislang nicht möglich, den Einfluss dieser Faktoren zu gewichten und zu quantifizieren. Ein Hauptanliegen dieser Studie ist es deshalb, den Einfluss von einigen dieser Faktoren zu analysieren, zu quantifizieren und zu gewichten.

Als Standardmethoden zur Untersuchung der mechanischen Festigkeit von Sedimenten und Störungsletten dienen verschiedene geotechnische Scherexperimente. In diesen wird eine Probe unter definierten Bedingungen eingespannt und geschert. Der Reibungskoeffizient, die Änderung des Porenanteils und andere aussagekräftige Kenngrößen werden ermittelt. Es ist leider nicht möglich während des Schervorgangs in diese Scherzelle ‚hineinzuschauen' und das Deformationsverhalten der Körner zu analysieren. In dieser Studie wurde deshalb ein anderer Ansatz gewählt, um speziell das Problem von mikroskopischen Deformationsprozessen zu analysieren. Der Ansatz beinhaltet die Anwendung einer Technik zur numerischen Modellierung, die Diskrete Elemente Methode (DEM).

Die DEM ist ein numerisches Verfahren, welches auf dem Verhalten granularer Materialien basiert. Mit einigen Einschränkungen können Sedimente und auch Störungsletten als granular betrachtet werden. Aus diesem Grund kann das Deformationsverhalten mechanisch schwacher Schichten mit dieser Methode simuliert werden. Das Prinzip der DEM beruht auf einfachen physikalischen Kontakt- und Bewegungsgesetzen und kann Merkmale und Verhalten von Körnern reproduzieren. Das Verfahren wurde bereits zur Modellierung von anderen granularen, sowohl groß- und kleinmaßstäblichen Deformationsprozessen genutzt.

Mit Hilfe dieser Methode wurde analog zu geotechnischen Ringscherexperimenten eine numerische Scherzelle entwickelt. In dieser Zelle wurde eine Vielzahl numerischer ‚Proben' erzeugt. Diese „Sedimente" und „Störungsletten" wurden je nach Bedarf innerhalb der Rahmenbedingungen der einzelnen Kapitel konzipiert. Während der numerischen Experimente wurde eine Vielzahl von mikromechanischen Parametern (Partikelbewegung und -rotation, Entwicklung des Mikrogefüges, Koordinationszahl, Anteil gleitender Partikel, Kraftverteilung und -orientierung) gemessen. Dies beinhaltete ebenfalls die Messung klassischer geotechnischer Kennzahlen wie Reibungskoeffizient, Porenanteil und Volumenänderung.

Es konnten nicht alle Faktoren, die das Deformationsverhalten beeinflussen, untersucht werden. Die Manuskripte konzentrieren sich deshalb auf:
(1) Oberflächenrauhigkeit. Diese hat vermutlich mindestens einen zweitrangigen Einfluss auf die Scherfestigkeit. Im Labor ist der Einfluss der Oberflächenrauhigkeit schwierig zu untersuchen, da sie unter Laborbedingungen nicht reproduzierbar ist.
(2) Kornform von Tonmineralen. Geotechnische Experimente haben ergeben, dass die Kornform von Tonmineralen einen großen Einfluss auf das Deformationsverhalten hat. Dieses Manuskript konzentriert sich auf zwei Merkmale der Kornform: Spherizität und Rauhigkeit.
(3) Schichtung von Ton und Silt. In einem komplexen, geschichteten System ist bislang nicht bekannt, an welchem Ort innerhalb einer Probe die Bewegung einzelner Körner kumuliert. Aus diesem Grund wurde eine Detailstudie zur Mikromechanik des granularen Deformationsverhaltens durchgeführt.
(4) Mischung von Ton und Silt. Hier wurde ein geotechnisch gut verstandener Zusammenhang zwischen Tonanteil und Scherfestigkeit im Modell getestet. Diese Experimente wurden durchgeführt, um die Vergleichbarkeit zwischen Laborversuchen und numerischen Versuchen zu überprüfen und einzuschätzen.

Vergleiche zwischen numerischen und geotechnischen Experimenten zeigen, dass Ergebnisse von numerischen Modellen mit einigen Einschränkungen auf Verhältnisse in der Natur anwendbar sind. Wie geotechnische Experimente haben vermuten lassen, existiert ein Einfluss der unter (1) - (4) genannten Faktoren auf das mikroskopische Deformationsverhalten von Sedimenten und Störungsletten.
In Kapitel II konnten Schwellenwerte für Oberflächenrauhigkeit ermittelt werden. Unterhalb einer Oberflächenrauhigkeit von 0.25 führte die geringe Rauhigkeit zu geringer Reibung,

sowohl der Oberfläche als auch der Probe, so dass die Oberfläche von der Probe mechanisch entkoppelte. Oberhalb eines Grenzwertes von 4 führte die hohe Rauhigkeit zu geringer Oberflächen- aber hoher Probenreibung. Damit fand keine mechanische Entkopplung statt; es bildete sich eine konzentrierte Scherzone in der Umgebung der Oberfläche. Eine mittlere Rauhigkeit zwischen diesen Grenzwerten ergab mittlere Reibung innerhalb der Probe, aber die höchste Reibung an der Oberfläche. Die Lokalisation der Scherflächen war dabei innerhalb der ganzen Probe verbreitet.

Im darauf folgenden Kapitel (Kapitel III) wurden Spherizität und Rauhigkeit von Partikeln als Schlüsselfaktoren identifiziert. Die Entwicklung eines Mikrogefüges ist abhängig von der Verzahnung und Rotation der Partikel. Da erhöhte Partikelrauhigkeit eine Steigerung der Verzahnung zur Folge hat, konnte das Mikrogefüge sich während der Verscherung nicht auflösen, so dass sich keinerlei Scherzonen bilden konnten. Im Gegensatz dazu wurde der Zusammenbruch eines Mikrogefüges durch die Verringerung der Spherizität gefördert. Das führte dazu, das Partikel zu Vorzugsrichtungen hin rotieren konnten, was wiederum zu geringer Reibung und erhöhter Scherzonenbildung beitrug.

Des weiteren wurden in Kapitel IV zwei geschichtete Proben analysiert: (1) Ein „Silt“-„Ton“-„Silt“ und ein (2) „Ton“-„Ton“-„Ton“ Schichtpaket. In diesen Tests zeigte sich, dass der Kontrast der Partikelreibung zwischen einzelnen Schichten einen großen Einfluss auf das Deformationsverhalten hatte Die Unterschiede im Partikelreibungskontrast steuerten den Modus der granularen Deformation, das heißt ob Partikel gleiten, rollen oder rotieren. Wenn der Modus innerhalb einer Probe wechselte, änderte sich ebenfalls der Ort von Scherflächen. Die ermittelten Deformationsstrukturen waren sehr gut mit in der Natur und im Labor vorkommenden Strukturen vergleichbar. Speziell in den „Tonen“ waren Y-, P- und R_1-Scherflächen in großer Zahl vorhanden. Zudem konnten Scherflächen und Partikelausrichtung korreliert werden.

Der Vergleich von numerischen und geotechnischen Experimenten in Kapitel V belegte den Einfluss des Tonanteils als einen Kontrollfaktor für Scherfestigkeit. Beide Methoden zeigten, dass der Tonanteil in einer Probe mindestens 50 % betragen muss, bevor es zu einer signifikanten Verringerung der Scherfestigkeit in einem Sediment kommt. Es konnte veranschaulicht werden, dass die Kombination von Laboruntersuchungen und Numerik die Klassifikation von Einflussgrößen auf die Scherfestigkeit erlaubt, gerade weil die DEM die Beobachtung von Scherflächen während der Deformation ermöglicht.

Am Ende dieser Arbeit steht eine Gewichtung der analysierten Parameter. In dieser Gewichtung ist es nötig, zwischen den Schlussfolgerungen die die numerischen Modelle erlauben und den Schlussfolgerungen für die Natur zu unterscheiden. Deshalb haben - im Rahmen der Modellrandbedingungen - Partikelrauhigkeit und Tongehalt den größten Einfluss auf die Scherfestigkeit und die Lokalisation von Scherbewegungen von Sedimenten und Störungsletten. Der Einfluss von Oberflächenrauhigkeit ist geringer, gefolgt von Partikelspherizität. Der Einfluss der Schichtung ist schwierig zu beurteilen, da sie in verschiedenen Umgebungen einen jeweils anderen Einfluss hat.

Table of contents

Chapter I - Motivation and Concepts

Chapter II - A systematic study on the influence of boundary surface roughness on deformation of granular materials

Chapter III - Influence of particle shape on the frictional strength of sediments - a numerical case study

Chapter IV - Numerical investigation of localization and micro-mechanics in a stratified soil specimen

Chapter V - Comparative numerical and analogue shear box experiments and their implications for the mechanics along the failure plane of landslides

Chapter VI - Summary

Appendix

Chapter I

1 Introduction

In the upper crust and its overlying sediments brittle deformation (shear and fracture processes) is abundant. Two examples are the formation of accretionary prisms at subduction zones and slope destabilization with associated submarine landslides. Despite the obvious differences between these examples, they have much in common.

A key feature of both accretionary prisms and submarine landslides is the need of a basal décollement, or shear plane (Fig. 1). Along this shear plane large displacements may be achieved.

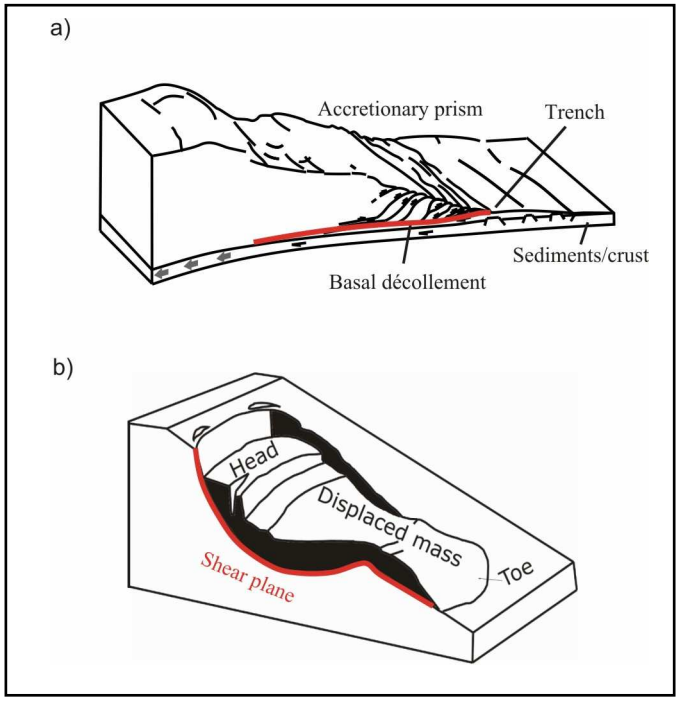

Fig. 1 Basal décollements and shear planes (red line). a) Sketch of accretionary wedge principle (modified from Cloos and Shreve, 1988). b) Sketch of landslide principle (modified from Varnes, 1978).

The initial formation of such basal shear planes, or décollements, depends on the mechanical properties of the rock or sediment, respectively. For deformation to localize at a specific plane in a given material, a shear plane has to be initiated or reactivated. Reactivation of pre-existent shear planes, e.g. in pre-existing fault gouge, is usually mechanically more favourable than formation of new shear planes in intact rock (Scholz, 2002). Formation of new shear planes occurs in materials which are characterized by a lower shear or frictional strength compared to the surrounding material (Dahlen, 1984; Hampton et al., 1996). These mechanically weak materials are commonly called ‘weak layers’. Studies of weak sediments, such as soils and fault gouge (e.g. Lambe and Whitman, 1969; Logan et al., 1979), have revealed much of their material properties. However, on a basic level and microscopic scale, much remains to be understood. For example, how a shear plane develops and why it evolves in a particular space and at a specific time is not yet fully understood. Analyzing these processes of localization and micromechanics requires the study of many influential parameters. These parameters include grain size distribution, grain properties (e.g. shape), pressure, etc.

The overall goal of this study is to analyze some of these parameters. The particular goals are described later in this chapter (section 4), since it is first necessary to understand some basic rock and soil mechanics principles (section 2, this chapter). The characteristics of weak layers and the deformation behaviour of soils and fault gouge are reviewed in section 3 of this chapter.

2 Basic concepts of friction and failure

2.1 Friction

Friction is a force acting on the contact plane of two bodies which opposes the relative motion of these bodies (Stöcker, 1994). In itself, friction is a reactive force which originates from the electromagnetic forces of atomic and subatomic particles (Persson, 1998).

Study of friction began with Leonardo da Vinci, but simple friction laws were first introduced by Amontons (1699) and later verified by Coulomb (1785; for an overview see Gao et al., 2004). The so-called 'Amontons' Law', or 'Coulomb friction law' consist of a simple empirical relationship where the frictional force F parallel to a surface scales with load L normal to a surface and (a material and boundary condition dependent) coefficient of friction μ:

(1) $F = \mu L$.

The coefficient of friction can also be described geometrically by the friction angle ϕ, so that $\mu = \tan\phi$ (Fig. 2). This relationship incorporates a wide range of conditions, such as dry and lubricated contacts, microscopic and macroscopic contacts, and rough and smooth surfaces. However, it fails when adhesion is introduced into the system and it is not valid for a wide range of loads and sliding velocities (Gao et al., 2004).

In the last century, Terzaghi (1925) and Bowden and Tabor (1950; 1964) analyzed friction in terms of applied load L, critical shear stress τ_c, critical normal stress σ_c and, importantly, area of real contact ΔA between two rough surfaces which increases with load. Critical shear stress τ_c is the yield stress during shear, whereas critical normal stress σ_c is the largest normal stress a material

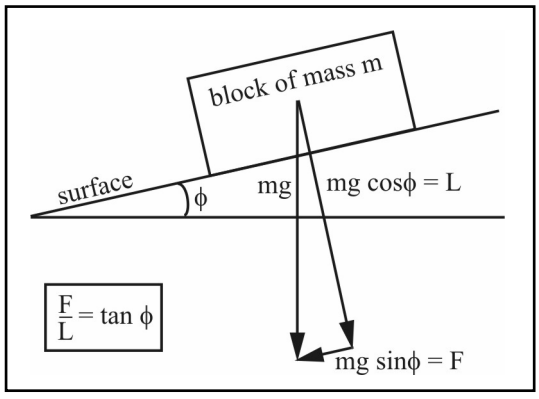

Fig. 2 Principle of friction for an inclined block. Note that tan ϕ = μ and is independent of weight mg.

can bear without plastic yielding (Persson, 1998). They found that:

(2) $F = \tau_c \Delta A$ and (3) $L = \sigma_c \Delta A$.

Combining these yields:

(4) $F = \frac{\tau_c}{\sigma_c} L$, so then, with eq. (1):

(5) $\mu = \frac{\tau_c}{\sigma_c} = \frac{F}{L}$.

These laws are empirical, and exhibit a variety of features which hold true under most conditions, but do not apply but other cases:

In principle, μ should be independent of surface roughness. This holds true, unless the surface is very rough, although a definite boundary for 'very rough' cannot be determined (Lambe and Whitman, 1969). Also, many experiments show that usually μ is independent of weight (Fig. 2; Persson, 1998).

There exists a difference between static and kinetic (= sliding) friction. The shear force necessary to initiate motion is mostly larger than the one needed to maintain motion. Thus, static friction is often larger than kinetic friction. The friction between two bodies rolling over one another, so-called rolling friction, is usually very low and lower than static and kinetic friction (Lambe and Whitman, 1969).

2.2 Failure

The analysis and prediction of small- and large-scale geological failure processes was developed along with the concept of friction. A widely accepted failure criterion for granular material is the Mohr-Coulomb criterion:

(6) $\tau = \tau_0 + \mu \sigma_N$.

The similarity to eq. (5) is striking, except that in this case τ and σ_N are shear and normal stress on any plane in a material with a cohesion of τ_0 and an internal friction μ (Scholz, 2002). For an intact material, internal friction μ cannot be determined. Thus, destructive tests have been developed to measure the shear strength of a material. Simply put, shear strength is defined as the value of τ when the material fails in a shear test and is often called τ_{crit}.

In its simplest form (i.e. cohesionless), eq. (6) becomes applicable to cohesionless soils with

(7) $\mu = \frac{\tau}{\sigma_N}$.

Failure can then be understood on a microscopic scale as failure between grains in a soil (Scholz, 2002). Friction μ in this case is the friction coefficient between adjacent grains, which from now on will be called the particle coefficient of friction $\mu_{(P)}$. It is impossible to determine the coefficient of friction $\mu_{(P)}$ for all individual grains in a material. However, even if this was accomplished it would still be impossible to predict the shear strength of the bulk material. Therefore, even for cohesionless materials, shear tests are necessary to determine shear strength.

2.2.1 Laboratory tests of shear strength

One of the goals of shear tests is to analyze deformation behaviour of samples and relate the results to naturally occurring processes. Therefore, testing conditions have to resemble natural conditions as closely as possible. This includes the amount of water. That water content of a soil or fault gouge significantly influences the state of stress was first demonstrated by Terzaghi (1925), who introduced the concept of effective stress. Water in pores between grains exhibits fluid pressure, so that the normal stress σ_N is reduced by pore pressure p_w to the effective stress $\sigma'_N = \sigma_N - p_w$. The Mohr-Coulomb failure law for effective stress then becomes

(8) $\tau = \tau_0 + \mu\sigma'_N$.

For low pressure regimes the (sometimes modified) direct and the ring shear experiments are suited best (Scholz, 2002). The advantage of the direct shear test is its simplicity, while a ring shear test device can accumulate large displacements (Bishop et al., 1971; Lambe and Whitman, 1969). The sketches in Fig. 3a,b show that, despite different setups, the underlying principle is the same for both tests: A sample is positioned between two rigid plates of arbitrary material (e.g. steel, porous ceramics, granite, etc.). First, a normal load is applied to the sample. Then the upper or lower half of the shear box is moved with a constant velocity while the other one stays fixed. The sample in between the walls starts to shear. The shear force necessary to move the wall is measured continuously. A graph that shows shear force or friction vs. displacement or strain produces a characteristic curve (Fig. 3c).

At the beginning, with increasing displacement, the shear force increases strongly. Depending on the type of material, volume of the sample can increase or decrease. At point b in Fig. 3c, the peak shear stress has been reached and the sample yields. In a lot of cases, the yield point is not as pronounced as shown in Fig. 3c since it is mostly a function of grain or mineral alignment after failure. After the material yielded, shear stress decreases. With increasing displacement, point c is reached. From now on, the material deforms without further volume

change if shear rate is held constant. This point is called the critical state strength. For some materials, e.g. clays, shear strength decreases further with increasing displacement, so that residual shear strength is reached at point d (Lambe and Whitman, 1969; Mitchell and Soga, 2005). Stable sliding occurs when friction does not vary with increasing displacement and can begin at points c or d.

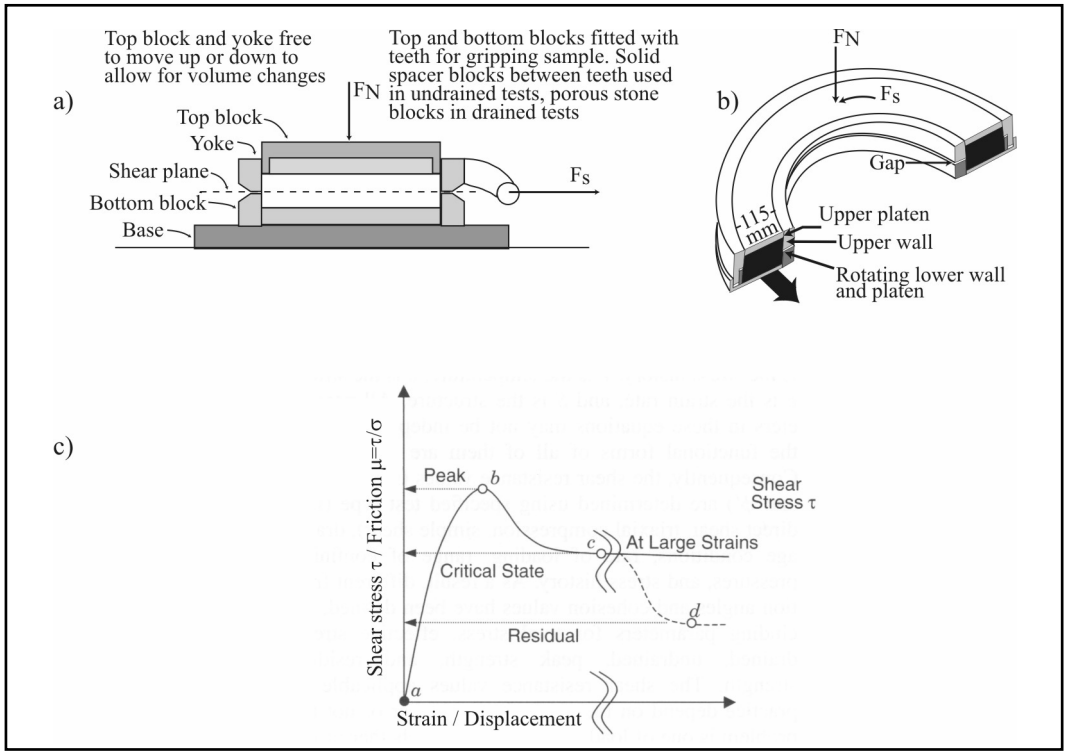

Fig. 3 Principles of laboratory tests of shear strength. a) Direct shear test (modified from Lambe and Whitman, 1969). b) Ring shear test (modified from Iverson et al., 1997). c) Idealized curve of measured shear strength data (modified from Mitchell and Soga, 2005).

Two general terms, hardening and weakening, can be used to describe the shape of a curve for shear strength. Hardening occurs if shear stress or friction increases, weakening if it decreases. In many cases these terms are combined with an apparent cause or observation, e.g. if shear stress increases with increasing strain, it may be termed strain hardening. If friction decreases when sliding velocity is stable during a shear experiment, the effect is termed velocity weakening.

In some cases, so-called stick-slip behaviour can be observed during a shear experiment. This means that there is an oscillating pattern of (1) stress drop with associated slip and (2) a period with no motion and a stress increase (Scholz, 2002).

Depending on the goals and objectives of a study, shear tests can be carried out under a variety of conditions. One possibility is that the sample shows zero humidity (e.g. dried in an

oven before testing); the other extreme is a water saturated sample. Considering eq. (7) it is evident that a saturated or wet sample exhibits lower shear strength than a dry one. For wet samples testing of shear strength may be conducted under drained and undrained conditions. If drainage is allowed, the water in the pores is allowed to move freely and excess pore pressure can dissipate, so that pore pressure inside the sample is in equilibrium and static (Lambe and Whitman, 1969). Undrained means that excess pore pressure is maintained during the testing procedure.

3 Deformation behaviour of soils and fault gouge

There are many questions still unsolved where deformation processes of soils and fault gouge are concerned. One key question is the identification and quantification of parameters that influence the shear strength of a particular sample; another is the question where and when failure will occur in the sample (localization). Tools to answer these questions are geotechnical shear tests and numerical modelling.

3.1 Composition of weak layers

There is no definitive rock or soil type that composes weak layers. Rather, they are characterized by their low relative mechanical shear strength compared to the surrounding rock or soil. Furthermore, a weak layer is not just one specific stratigraphic unit, but deformation takes place in well defined parts of a stratified sediment, so that a whole package belongs to a shear zone (Canals et al., 2004; Labaume et al., 1997; Maltman et al., 1997). Therefore, composition of that zone may vary. This study is limited to rocks that can essentially be described as granular materials. These are uncemented soils and fault gouge.

Despite several factors influencing the shear strength of soils and fault gouge (see section 3.2 in this chapter), low shear strength is commonly explained by their mineral composition and texture, which is confirmed by a large number of geotechnical experiments (e.g. Ask and Kopf, 2004; Kopf and Brown, 2003; Krantz, 1991; Lambe and Whitman, 1969; Marone, 1998; Mitchell and Soga, 2005; Saffer and Marone, 2003). In particular, clays exhibit lower shear strength than quartz, feldspar, calcite etc. (Mitchell and Soga, 2005; Saffer and Marone, 2003). Lupini et al. (1981) have shown a direct relationship between clay fraction and shear strength of sediments. These authors also suggest that most probably the alignment of tabular clay minerals during shear is the mechanism responsible for the low residual shear strength. Detailed microscopic analyses of deformed clay structures support this suggestion (Bennett et al., 1991b). However, detailed information about exact deformation mechanisms and processes at grain contacts during shear remain unobservable from analogue tests. For the

above reasons, soils and also fault gouge can be seen as a mixture of two end-members concerning grain size and mineral composition. In case of soil, these end-members are clay and silt, whereas for gouge the end-members are clay and granular rock fragments:

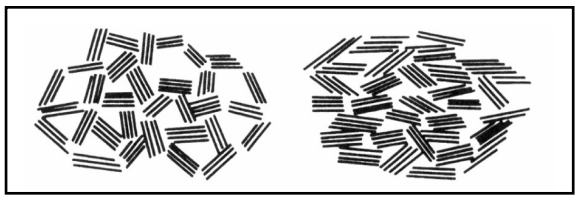

Fig. 4 Two examples of clay microfrabric (from Mitchell and Soga, 2005). Left: domains enclosing large voids, domains mostly touch mostly edge to face (dispersed). Right: domains enclosing small voids, domains touch each other both face to face and edge to face (aggregated).

Clays are silicate sheet minerals with a grain size <2µm (Mitchell and Soga, 2005). Depending on the structure and chemistry (especially the abundance of electrostatically bonded water molecules), clay minerals can be subdivided into various groups (Mitchell and Soga, 2005). Important groups include kaolinites, illites and montmorillonites (e.g. smectite). Characteristic of clay minerals is the elongated, tabular shape, regardless of the respective group. That means that the [001]-axis perpendicular to silicate sheet orientation is very short compared to the other directions, which is considered relevant to the deformational behaviour (see above). Another geotechnically important feature of clay minerals is the tendency to form associations during sedimentation (Mitchell and Soga, 2005). This leads to a variety of structures in an intact soil, called microfabric (Fig 4; Bennett et al., 1991b; Mitchell and Soga, 2005). The development of microfabric is steered by many mechanisms. For example, in an environment with high salinity, clay mineral aggregation increases due to the interplay between electrochemical forces of salt ions, surface charge of clay minerals, and the attractive van-der-Waals force. For example, clay minerals can built areas of parallel particle alignment, so-called ‘domains’ (Mitchell and Soga, 2005).

Clay microfabric is important for soil deformational behaviour for a variety of reasons. First of all, depending on the geometric arrangement, there is a defined amount of void space which can decrease with compaction or shear. Furthermore, this void space is usually filled with water, thereby increasing pore pressure and decreasing effective strength by a significant amount. Secondly, microfabric can disintegrate when boundary conditions change, e.g. pressure during burial or deformation, or salinity. Disintegration of microfabric would lead to different geotechnical properties. Thirdly, on a macroscopic scale, fabric anisotropy leads to mechanical property anisotropy, so that mechanic strength may significantly differ for different directions (Mitchell and Soga, 2005).

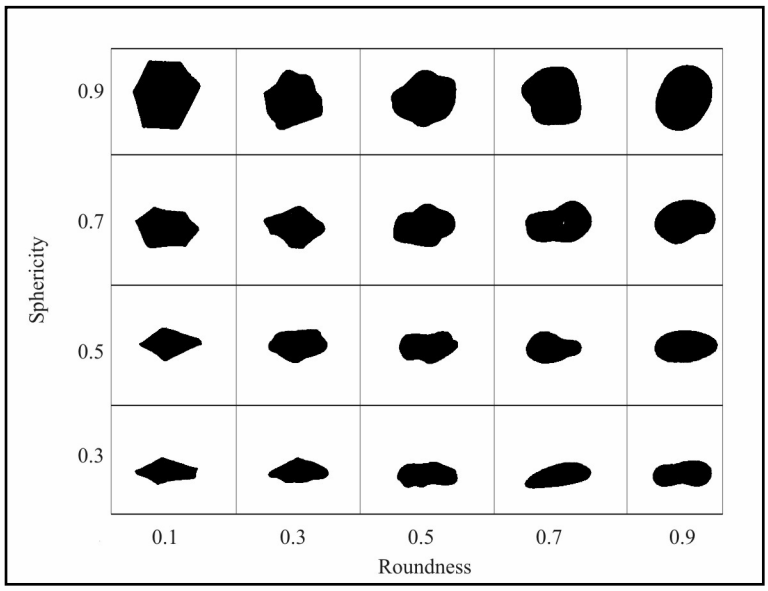

Fig. 5 Example of grain shape of silts (from Mitchell and Soga, 2005).

Silt is defined by a grain size ranging between 2μm and 63 μm (Heiling, 1988). Silt can consist of many minerals, but by far the most common is quartz, followed by small amounts of feldspar (Mitchell and Soga, 2005). Electrochemical surface forces also exist for silt grains, although they can be neglected for large grains. For small grains near the clay/silt distinction however, surface forces can have the same effect as for clays, so that complex microfabric may develop (Mitchell and Soga, 2005). In contrast to clay minerals, the minerals forming a silt exhibit a shape ranging from angular to spherical and from not rounded to well-rounded, which influences their geotechnical properties (Fig. 5; Mitchell and Soga, 2005).
An important parameter to characterize silts is their grain size distribution. A high abundance of small particles can for example fit in the void spaces created by the larger grains. Thereby, the void ratio and the water content are reduced, which can influence effective stresses. Grain size distribution of sediments is a process highly dependent on the environmental conditions and a wide range of statistical approaches has been employed to link deposition environment to grain size distribution (e.g. Weltje and Prins, 2003).

The granular rock fragments in fault gouge are a product of wear along faults surfaces and therefore can contain a variety of minerals, depending on the country rock. However, most common are quartz, clay minerals and feldspar. Since the term silt only describes grain size, a fault gouge can consist of silt sized grains. Grains of fault gouge can be angular or well-rounded and for small grains electrochemical surface forces can be active, so fault gouge can

also built up microfabric. Through comminution, grains in fault gouge are constantly destroyed and their size decreases. Through abrading wear on the fault surfaces new grains may develop. This process leads to a typical grain size distribution of fault gouge, which seems to obey a fractal or power law relationship (Sammis and Biegel, 1989).

3.2 Frictional strength

For clayey soils, the wealth of shear tests carried out to date supply a variety of parameters that influence shear strength (Mitchell and Soga, 2005). As already mentioned above, strength decreases when clay mineral fraction is increased (Kopf and Brown, 2003; Lupini et al., 1981; Saffer and Marone, 2003). This indicates that the reorientation of tabular clay particles and associated change of microfabric during shear has a significant influence on deformation. Among others, Rutter et al. (1986) suggest that this also holds true for fault gouges. There are some conclusions that may be drawn from this. First, grain shape may influence shear strength, but only few systematic studies have been carried out to systematically analyze this effect in the laboratory (Anthony and Marone, 2005; Mair et al., 2002; Mueth et al., 2000). Unfortunately, these studies concentrate on the differences between angular and round grains on a microscopic scale rather than the differences between elongated, tabular (e.g. clay) and approximately round (e.g. silt) grains. Second, grain properties such as the particle coefficient of friction $\mu_{(P)}$ can vary between two different minerals. According to Lambe and Whitman (1969) these differences may be due to irregularities on the surface of minerals on the nanometer scale. On these scales however, the effect of true cohesion due to electro-chemical bonding between molecules is difficult to separate from mechanical friction (Lambe and Whitman, 1969). Studies to evaluate the effect of particle coefficient of friction are in progress, but not yet published (Knuth et al., in press).

3.2.1 Observations from analogue tests

Logically, since grain rotation and/or sliding require space, the void ratio (porosity) of the specimen must have a direct effect on deformation. Hence, the measurement of void ratio during shear or compaction is one of the most widely used parameters to characterize deformation behaviour (Lambe and Whitman, 1969; Mitchell and Soga, 2005). This is true not only for clays, but also for silts and fault gouge (e.g. Lockner and Beeler, 2002).

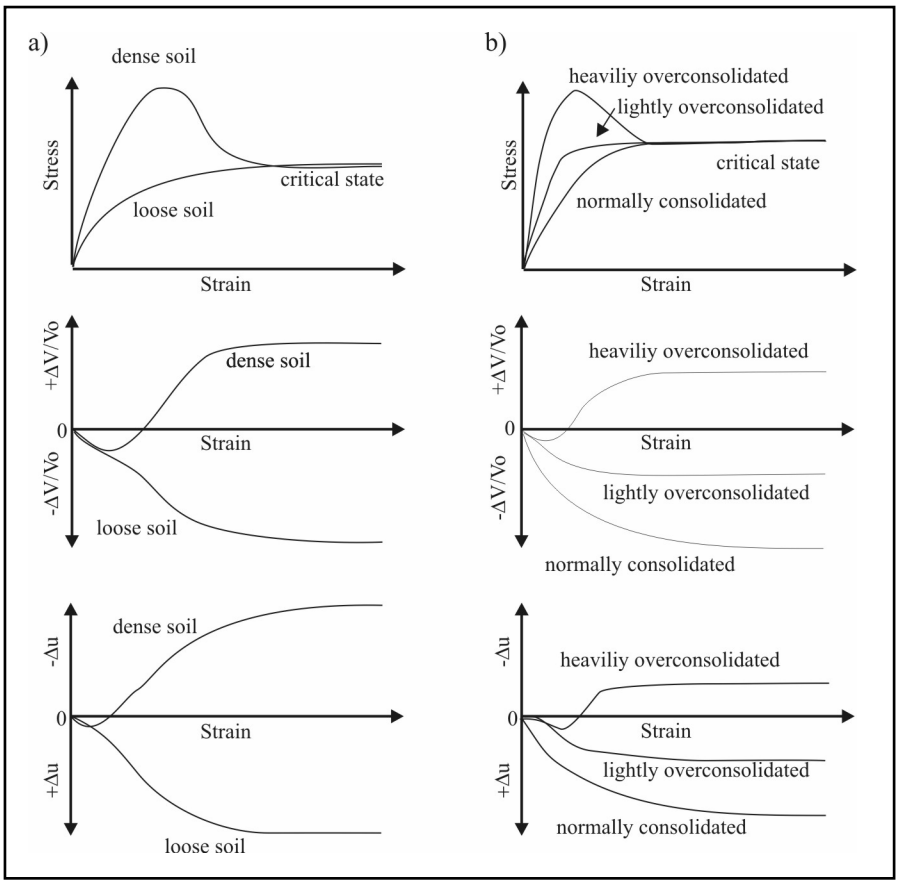

Fig. 6 Deformation behaviour of granular materials and clays (after Mitchell and Soga, 2005). a) Granular material. Top: Stress/Strain behaviour. Middle: Volume change/dilation. Bottom: Excess pore pressure. b) Clay. Top: Stress/Strain behaviour. Middle: Volume change/dilation. Bottom: Excess pore pressure.

For densely packed granular samples, the void ratio increases during shear (Fig 6a). For deformation to occur, the grains have to slide past another so more space has to be created. Overall volume and void space increases till the critical state strength (section 2.2.1, this chapter) is reached. This process is known as dilation (Fig. 6a). For a loose sample, the reverse is true. Induced shear results in contraction until the material deforms without further volume reduction. These observations are true for both soils and fault gouge (Marone et al., 1990).

The evolution of void space is closely related to the pore pressure (Mitchell and Soga, 2005). A sample is normally consolidated, when pore pressure equals the surrounding pressure (i.e. hydrostatic pressure in marine sediments), lightly overconsolidated when pore pressure is only slightly higher than surrounding pressure and highly overconsolidated when pore pressure is significantly higher than surrounding pressure. Overconsolidation is usually observed in clayey material and not in gouge or silts, since clay shows very low permeability.

For a shear test where drainage is enabled, different consolidation results in different amounts of volume change behaviour during shear. Normally consolidated and lightly overconsolidated clays experience volume reduction whereas highly overconsolidated clays show dilation (Fig. 6b). For undrained tests, pore pressure changes with shear displacement. Normally consolidated and lightly overconsolidated clays exhibit positive excess pore pressure and highly overconsolidated negative excess pore pressure (Fig. 6b), since excess pore pressure evolution is closely linked to microstructure development (Mitchell and Soga, 2005).

The mechanical strength of a material also depends on the magnitude of effective normal stress. Although the shear stress τ at failure increases with increasing effective stress σ'_N (e.g. Bishop et al., 1971), the residual shear strength $\frac{\tau}{\sigma'_N}$ (i.e. the coefficient of friction μ) decreases (Bishop et al., 1971; Kopf and Brown, 2003; Mitchell and Soga, 2005).

Another factor influencing deformation behaviour is the deformation history of a material. If a previously deformed material undergoes further deformation, the previously experienced changes in void ratio, grain reorientation, microfabric disintegration, pore pressure evolution, etc. determine future deformation behaviour (Mitchell and Soga, 2005). Peak strength decreases for previously deformed materials while the critical state coefficient of friction is independent of former stress history (Mitchell and Soga, 2005).

3.2.2 Microscopic behaviour

A parameter that influences both dilation and frictional strength is the grain size distribution (GSD). Dieterich (1981) tested the mechanical strength of gouges in a variation of the direct shear cell. The gouge samples used had a fine and coarse GSD and, importantly, a gouge with a GSD including all fractions. He observed that the fine-grained gouge showed highest strength, followed by the GSD with all fractions. The coarse-grained GSD sample exhibited the lowest strength. Dieterich (1981) concluded that mechanical strength depends on the relative amount of the fine grain size fraction. Following that pioneering study, numerous studies on the development of GSD during shear have been conducted (Biegel et al., 1989; Biegel et al., 1992; Blenkinsop, 1991; Gu and Wong, 1994; Logan and Rauenzahn, 1987; Mitchell and Soga, 2005; Rutter et al., 1986; Sammis and Biegel, 1989; Sammis et al., 1987; Sammis et al., 1986; Sammis and Steacy, 1994; Scott et al., 1994).

The goal of some of these studies was to develop a theoretical framework explaining the effect of GSD. One main feature that is controlled by the GSD are the contact forces between grains in the material. In any granular material external forces and stress (e.g. load or shear) are transmitted via forces between contacting grains. This transmission is not homogenous, so that some grains carry more load than others, thereby building so-called 'grain bridges' or 'contact bridges' connecting both shear zone boundaries (Means, 1976; Mitchell and Soga, 2005). It has therefore been suggested that fragmentation processes along these grain bridges govern deformation behaviour of gouge (e.g. Sammis et al., 1987). The relation between GSD, contact force distribution inside a material, and its deformation behaviour is very complex. This kind of micromechanical deformation behaviour has become a focus of numerical modelling in recent years and thus will be discussed later in section 3.4 of this chapter.

The roughness of the surrounding country rock or, in case of laboratory experiments, boundary walls, also has an influence on the frictional strength of a material (Biegel et al., 1992; Chambon et al., 2006; Scholz, 2002). This contradicts eqs. (2) to (5), where the area of real contact of two rough surfaces has been eliminated from the equation, and thus should have no influence on the coefficient of friction. The reason for this effect lies in the deformation of the contact areas themselves. These contact areas at asperities on a surface can deform elastically and/or plastically and their number may increase or decrease during shear (Scholz, 2002; e.g. by abrasive fault surface wear). Thereby, frictional strength is influenced to a degree which cannot be captured by eq. (5). This indicates that roughness may also influence the deformation of gouge and soils. Biegel et al. (1992) showed that during the initial phase of slip, smooth surfaces exhibit greater strength while for later displacement strength is larger for rough surfaces (strain hardening).

3.2.3 Rate and state friction laws

Recent studies of (simulated) fault gouge mainly focus on the development and enhancement of rate and state constitutive friction laws (RSF laws; Marone, 1998; Scholz, 1998). These laws are empirically derived laws, which relate laboratory stick-slip motion to the seismic cycle, so that an earthquake represents the 'slip' and the interseismic period the 'stick' phase (Marone, 1998; Scholz, 1998). These laws show that shear strength depends on sliding velocity and change of sliding velocity (Scholz, 1998). A feature of this model is that the distinction between static and dynamic friction disappears and that a large portion of seismic observations can be explained (Scholz, 1998). Important results include the introduction of

two new friction parameters (called (a-b)-parameter and critical slip distance D_c). For a more detailed outline of these laws, the reader is referred to Marone (1998) and Scholz (1998; 2002).

3.3 Localization

The accumulation of shear displacement in time and space (i.e. localization) in soils and fault gouge is very difficult to assess and still poorly understood. At first glance, this is surprising since in a lot of cases a distinct failure plane can be observed when shear testing was conducted in experimental setups similar to those in Fig. 3a. However, locations of these planes can be influenced by shear box geometry; for example, the setup of a direct shear box leads to a shear plane in between the two confining halves of the box (Fig. 3a). This means that, on a macroscopic scale, the location of displacement can be biased by shear box layout. On a microscopic scale, the onset of displacement localization is difficult to observe and therefore largely uninvestigated.

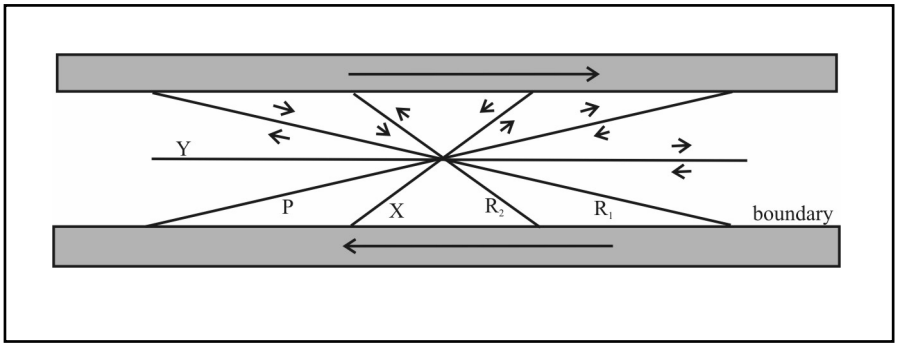

Fig. 7 Shear plane orientations in a shear zone (from Gu and Wong, 1994). Arrows in boundaries indicate overall sense of shear. Shear sense orientations at shear planes indicated by arrows.

In a general sense, displacement accumulation can either be completely distributed throughout a sample, or may be extremely localized as a sharp discontinuity on one discrete shear plane. In a lot of cases, shear localizes in so-called shear (or deformation) bands, which represent zones of shearing and volumetric deformation (Aydin et al., 2006). In nature and in the laboratory, these shear bands follow a clearly defined geometry, which usually is most obvious in clay-bearing rocks (Rutter et al., 1986). Furthermore, inside these macroscopic shear bands the same geometry can be observed for slip planes on a grain scale level (e.g. Mair et al., 2002). The nomenclature of this geometry mainly follows Berthe et al. (1979) and Logan et al. (1979), but is based on observations from Riedel (1929). In Fig. 7 the orientations of structural features are shown (nomenclature based on Logan et al. (1979) and Riedel (1929)).

The most dominant plane is usually the R_1-plane, which often lies about 45° inclined to the shear direction (Rutter et al., 1986). However, in clay-rich material, planes oriented between 135° and 180° in shear direction (Rutter et al., 1986) may first form during shear, supposedly due to the alignment of platy clay minerals (Gu and Wong, 1994). This is called the P-foliation or P-orientation. P- and R_1- shears are thought to form early during deformation (Gu and Wong, 1994; Rutter et al., 1986; Scholz, 2002). At a later stage during deformation, shear zones or slip planes oriented exactly parallel to the shear sense may also form inside the material. These Y-surfaces often are located directly in the middle of the shear zone (Gu and Wong, 1994; Rutter et al., 1986) or, as commonly observed in the laboratory, at shear zone boundaries (Mair et al., 2002). Additionally, a set of minor surfaces such as R_2 and X shears exist, which are inclined at a very high angle to the shear zone (Gu and Wong, 1994).
Displacement accumulation on each of these surfaces and their respective duration of activity differs. Due to their orientation, Y-surfaces can accumulate very large displacements and are thought to be active for a long time, once they have formed (Rutter et al., 1986; Scott et al., 1994). In contrast, R_1-, R_2- and P- oriented surfaces can only accumulate a restricted amount of slip, since these surfaces are limited by shear zone boundaries (Gu and Wong, 1994; Rutter et al., 1986). It is thought that therewith the duration of activity of one slip surface is limited. Once the maximum amount of displacement has been reached another, parallel oriented shear plane, forms (Scott et al., 1994).

Despite the well-described internal geometry of these shear zones, the mechanism of their formation and particularly their kinematics are not understood. Rutter et al. (1986) have mentioned that Y-surfaces may deflect P- and R_1- oriented surfaces, so that particles may be offset and distorted. It is often assumed that the parameters influencing shear strength also play a significant role in determining if and how such a shear surface pattern evolves. With regard to this, Gu and Wong (1994) state that in clay-rich material the P-orientation develops first, succeeded by high-angle slip planes. In quartz dominated gouge, grain comminution and particle size reduction are necessary for R_1 shears to evolve after which other modes of shear localization are activated (P, Y, R_2, X; Gu and Wong, 1994).
Furthermore, it seems to be the case that the degree of localization is displacement-rate related. Beeler et al. (1996) showed that a high degree of localization occurs with small displacements at the beginning of an experiment. When displacement is larger, Y-planes form which extend to a network of multiple Y-planes. Moreover, localized deformation was coexistant with low strength and distributed deformation with high strength.

Mair et al. (2002) showed that visibility of localization can be stress-dependent. For a low stress regime, where grain fracture is considered negligible (5 MPa), no visible localization fabric could be observed. In contrast, for higher stresses R_1 slip planes and Y-surfaces were observed. Y-planes were evident both in the middle part and at the boundaries of the sample.
Also, rate and state laws are applied to localization phenomena, which shows that the dependence of strength on strain rate (i.e. velocity weakening/hardening, see above) is different for localized and distributed shear (Marone et al., 1992)

3.4 Numerical modelling

Recently, numerical modelling has been employed to investigate more closely the influence of all the parameters described above. The advantage of numerical modelling in these cases is a complete control of boundary conditions. For example, in laboratory tests which study the influence of surface roughness, it is impossible to achieve the exactly the same surface shape for surfaces which have nominally the same roughness (Biegel et al., 1992). This problem can be overcome by numerical modelling.
A variety of numerical models to simulate granular materials such as the Discrete Element Method (DEM, Cundall and Strack, 1978, see Appendix), the Lattice Solid Model (LSM, Mora and Place, 1994), and other methods (Oda and Iwashita, 1999) exist. These numerical modelling approaches have already confirmed some inferences that were made from laboratory data, e.g. the heterogeneous distribution of contact forces between single particles (Oda and Iwashita, 1999; Rothenburg and Bathurst, 1993; Thornton, 2000). Ng (1994; 2004), Rothenburg and Bathurst (1992a; 1992b; 1993), Thornton (2000) concentrated their studies on very general effects of particle shape on deformation behaviour and used elliptical and ellipsoidal shaped particles. Most researchers use the more common disc and spherically shaped particles (Abe and Mair, 2005; Antonellini and Pollard, 1995; Campbell et al., 1995; Cundall, 1987, 1989; Cundall and Strack, 1978, 1979, 1983; Guo and Morgan, 2004; Kuhn, 2003; Liu et al., 2004; Liu et al., 2003; Mora and Place, 1994; Morgan, 1999; Morgan and Boettcher, 1999; Oda and Iwashita, 1999). In general, elliptically shaped particles capture the deformation behaviour of granular materials such as sands better. However, inefficient algorithms which significantly increase computing time present a grave disadvantage of elliptical particle DEM simulations.
Hence - since in this study only the more efficient algorithms for circular and spherical particles are used - this review concentrates on results obtained from similar models (here: DEM & LSM). For the algorithms involved (only for the more common DEM after Cundall and Strack (1978)), the Appendix chapter offers a complete description. Besides the control of

all boundary conditions a major feature of the DEM is its ability to access all particle parameters in a particle assembly. Thus, for example particle displacement and evolution of particle stresses can be studied in detail on a microscopic level enabling the analysis of microscopic localization patterns.

3.4.1 Observations from numerical models

With regard to this, a microscopic DEM study by Antonellini and Pollard (1995) showed that deformation within a fault zone is controlled by the particle size distribution (PSD). They observed that the growth of a shear band starts with local dilatancy and then grows into a fully developed shear band. Further and more detailed work in this direction has been done by Morgan (1999) and Morgan and Boettcher (1999). These authors used a setup comparable to laboratory ring shear tests to study micromechanics as well as localization. They could show that the particle coefficient of friction $\mu_{(P)}$ controls particle tendency to slip (low $\mu_{(P)}$) or roll (high $\mu_{(P)}$) when subjected to shear stress. Furthermore, they observed that a higher abundance of small particle led to stabilization of frictional strength, which has also been observed in the laboratory (Biegel et al., 1989). In the numerical models deformation was regularly alternating between distributed and highly localized shear. Distributed shear occurred at multiple subhorizontal slip planes and localized shear at discrete particle contacts. Localization geometry in these cases was very similar to structures outlined above with existing R_1, P and Y slip surfaces.

In the same study (Morgan, 1999) it was shown that the mechanical strength of a material depends on the magnitude of normal stress, which is in concordance with laboratory results (section 3.2, this chapter). This could be verified later in a related study (Guo and Morgan, 2004).

A disadvantageous effect observed by Morgan (1999) however, is the relatively low frictional strength of simulated granular samples compared to natural ones. This observation can be largely attributed to (1) extensive particle rolling when granular matter is modelled by perfectly spherical particles and (2) a 2-D effect. This 2-D effect has been studied by Hazzard and Mair (2003) with the DEM. They consistently obtained slightly higher frictional strength for perfectly spherical particles that were modelled 3-D compared to 2-D. This has to be kept in mind when frictional strength of modelled 2-D particle assemblies is interpreted. The other effect, extensive particle rolling, is clearly dependent on particle shape. Guo and Morgan (2004) conducted comparative 2-D DEM studies on the effects of particle shape on the frictional strength of a sample. Since their focus lay on the modelling of angular fault gouge,

they used particle shapes which resemble angular grains. Here, friction increased with increasing angularity.

Not only the shape of grains, but also their ability to break apart plays a role for frictional behaviour of natural and laboratory soils and fault gouge (section 3.2, this chapter). Crushing of soil particles has been investigated by Cheng et al. (2004). They modelled lightly overconsolidated soils, where yield surfaces were defined by grain breakage. For heavily overconsolidated soils, grain breakage was confirmed as the reason for decreasing peak friction with increasing stress.
For fault gouge, Abe and Mair (2005) suggest that grain fracture in DEM simulations produces fault gouge with roughly the same particle size distribution as in laboratory experiments (see above). Furthermore, the mix of angular and spherical grain fragments resemble those generated in laboratory experiments from Mair et al. (2002).

3.4.2 Interparticle and stick-slip behaviour

As seen above, most authors concentrate their studies on the behaviour of fault gouge. There are few authors who concentrate on modelling soil: fabric of clay grains was modelled by Chen and Anandarajah (1996), Anandarajah (1994; 1997; 1999), Anandarajah and Lavoie (2002). The main goal of these studies was to develop algorithms to model the electro- and physico-chemical behaviour of clay during compression (van-der-Waals attraction, cementation, etc.). Main results are that the van-der-Waals force contributes to overconsolidation in natural clays and that it holds potentially unstable clay microstructure together until a threshold stress level during compression is reached.

Forces in a granular material are only transmitted only by interparticle contacts. This leads to a strong inhomogeneous force distribution inside a compressed material (e.g. Radjai et al., 1998). Thus, contact bridges develop, where only a very small number of contact points support the majority of the load. This is called the strong force network. Vice versa, the majority of the contact points which carry only little load, are called the weak force network. When a granular sample is sheared, the contact networks are changed, or destroyed and reformed. Hence, the contact force distribution may be used to explain underlying micromechanical processes during deformation. Aharonov and Sparks (2004) found that during the lock-up phase of stick-slip motion of a granular layer, the weak contacts start to slip initially. When enough weak contacts are sliding, the whole system becomes weaker and particles building up the strong force network also move by buckling and particle rotation

(Aharonov and Sparks, 2004); this is the slip phase. The complete stick-slip cycle is accompanied by major rotation of the inner force/stress orientation.

Stick-slip motion has also been studied extensively by other authors (Abe et al., 2002; Mora and Place, 1998; Place and Mora, 2000). These studies suggest that fault gouge shows gouge layer thinning and, for large displacements, particle reorganisation, so that during the slip-phase, sliding becomes highly localized in a thin shear zone (Place and Mora, 2000). Furthermore, rate and state constitutive friction laws were implemented in numerical simulations (Abe et al., 2002). These models produce results comparable to laboratory conditions (Abe et al., 2002). Similarly to Morgan (1999), Mora and Place (1998) observed a dependence between the particle coefficient of friction and the amount of rolling in a fault gouge layer.

4 Goal of this work

The overall goal of this study is the analysis of failure processes of weak layers in all kinds of geological settings, but it was inspired by failure processes on the basal shear plane of submarine landslides. Questions remaining to be answered include why destabilization or failure occurs at specific points in time and space, while at other locations, the sediment or fault gouge remains undeformed. As can be seen from the previous sections of this chapter, there remains much to be understood. The influence on shear strength and localization of parameters such as grain shape, clay content, boundary roughness, etc., has been recognized. However, there are simply too many interacting parameters to quantify the impact of one specific parameter on shear strength and localization. Therefore, the objective here is to quantify and, if possible, rank the influence of some selected parameters on deformation behaviour. This is done via parameter sensitivity studies utilizing numerical modelling on a microscopic scale.

The parameters to be analyzed are not selected arbitrarily. Criteria are the applicability of the numerical tool (the Discrete Element Method, see below) to model a parameter and the extent of previous knowledge gained from analogue tests. Thus, the main target are parameters which so far are not or not completely understood and are hard to study under natural and laboratory conditions. With regard to this, four parameters were chosen: Surface roughness (of faults and shear cell walls), particle shape of modelled ‘clay’ and ‘silt’, stratification as well as mixing of ‘clay’ and ‘silt’.

(i) Surface roughness

For example, surface roughness (e.g. of faults and shear box walls) is known to influence shear strength and localization, but is extremely difficult to study under laboratory conditions and thus has not yet been analyzed in depth. Hence, influence of surface roughness on deformation behaviour is a selected target in this study. The following questions are addressed in particular:

(1) What is the effect of surface roughness on:
   a. The development of distributed or localized shear?
   b. The frictional strength measured close to the surface and inside the material?
   c. Mechanical processes on the grain scale level (micromechanics)?

(2) What are the implications for shear zones, laboratory tests and numerical models?
   a. Can results from this study help to assess natural processes?
   b. Do these results help to interpret laboratory tests?
   c. Are specific values of surface roughness characteristic of specific geological conditions?

(ii) 'Clay' particle shape

When comparing deformation behaviour of elongated clay grains to angular or spherical silt grains, it is clear that the shape of clay grains is crucial for their deformation behaviour (section 3, this chapter). On a microscopic level, however, individual clay grains and clay domain deformation behaviour under shear is not understood. Therefore, the study of 'clay' particle shape and its relation to deformation processes is the next objective. Two features of particle shape controlling parameters were studied more closely: Sphericity (elongation) and roughness.

In particular, we varied the sphericity and roughness of single, simulated 'clay' particles to address the following questions:

(1) What influence do sphericity and roughness of 'clay' particles have on:
   a. Slip plane and shear zone location, orientation and abundance.
   b. Microfabric, domain evolution and single particle rotation.
   c. Frictional strength, volume strain and porosity.

(2) Is this influence comparable to natural conditions?
   a. Is it possible to achieve direct comparability between natural grains and modelled particles?

(iii) 'Clay' and 'silt' stratification

Once the influence of 'clay' shape was determined sufficiently, more complex simulations were carried out. Since weak layers in natural settings can consist of more than one lithological stratum, where one or more slip planes or shear zones may be active, the focus now shifted to the complicated interaction between sheeted lithologies. Two lithologies were simulated, a 'clay' layer sandwiched between two 'silt' layers, and a 'clay' layer between two 'clay' layers with slightly different properties. Particle shape of the 'clay' was a geometry selected from the previous experiment (see ii). In these settings, the contrast between the respective coefficients of particle friction $\mu_{(P)}$ was varied systematically to determine:

(1) What influence do friction contrasts in stratigraphic sequence have on:
   a. Localization patterns: Where do slip planes and shear zones form? At the base, top or intermediate part of a stratigraphic unit?
   b. Frictional strength and localization: Do shear planes always form in the weaker layer or are there exceptions? If exceptions exist, how realistic are they in terms of natural conditions?
   c. Deformation mechanisms: It is known that sliding and rotation depend on the particle coefficient of friction $\mu_{(P)}$. Do friction contrasts on the particle scale level affect this behaviour?

(2) How do the two settings differ?
   a. Is there a significant difference of localization patterns and frictional strength?
   b. How do micromechanical deformations modes (sliding, rolling and rotation) change for each setting?

(iv) 'Clay' and 'silt' mixing

To evaluate our numerical models it is necessary to compare them with measurements gained from natural materials. Therefore, a comparative study with numerical and geotechnical tests (ring and direct shear experiments done by Prof. Dr. A. Kopf) was conducted. Since the influence of clay fraction on frictional strength is well-documented for geotechnical tests (section 3, this chapter), this study concentrated on evaluating this feature for numerical tests. Furthermore, Scanning Electron Micrographs (SEM, done by Prof. Dr. A. Kopf) were taken from the analogue sample to compare localization features of numerical and geotechnical tests

(1) Do numerical and geotechnical tests agree:
   a. with the overall frictional strength of samples?
   b. with friction increase/decrease with varying 'clay' content?

c. with localization patterns after deformation?

(2) Advantages and disadvantages of each method:

a. What advantages and disadvantages can be found for each method?

b. How sensible is a combination of both methods to analyze a specific problem (e.g. slope failure)?

(3) Role of pore fluids:

a. Do differences between methods show influence of pore fluid pressure?

For all these studies the same numerical modelling technique was used: The Discrete Element Method (DEM).

4.1 Method

The DEM is based upon a granular model approach which represents an ideal tool to simulate grain-to-grain mechanics (Cundall and Strack, 1978). For a complete overview of the DEM principle, refer to Appendix. The DEM simulates numerous interacting particles as discs in 2D. The particles have distinct properties, such as a particle coefficient of friction $\mu_{(P)}$, and interact according to simple physical contact and motion laws. We use a commercially available DEM code (*P*article *F*low *C*ode 2D by Itasca, 2004). PFC2D provides an environment with basic DEM algorithms and an interface with C++ programming language. The complete code for the model setup and analyzing tools was written by myself to specifications outlined in section 4.1.1 and 4.1.2 in this chapter.

The advantage of numerical modelling is the control of 100% reproducible boundary conditions which allows changing only one parameter while all the others remain constant. Thus, the influence of one parameter can be quantified. Besides the control of boundary conditions, the most advantageous feature of numerical modelling is the instantaneous availability of all data in space and time during the model run. This allows not only analysis and interpretation at the initial and final stages of an experiment, but continuous monitoring during its simulation. At each point of time, position, velocity, rotation, forces, moments and number of neighbouring particles can be accessed for each particle. A peculiar feature of PFC2D, not common to any other DEM code, is the ability to combine spherical particles which may overlap. These clusters or clumps were used to simulate elongated ‘clay’ particles, where three or more spheres merge into one ‘clay plate’.

4.1.1 Model setup

A feature that the models should fulfill was resemblance to shear processes occurring under natural conditions. Furthermore, comparability to laboratory tests and other numerical simulations was required. Most important, however, was the scale. To understand deformation behaviour of soils and fault gouge, the DEM was employed from a microscopic point of view. That means that our models are scaled to natural conditions, so that DEM particles exhibit the same size as natural grains. These requirements led to the basic model setup in Fig. 8, a micro-scale artificial shear box. This shear box is basically comparable to a geotechnical shear device:

There is a fixed bottom wall and a top wall which is movable in the x- and y-direction to transfer shear rate and normal stress onto the numerical sample. Both walls correspond to the upper and lower porous plate of a true shear cell. Shear rate always was 10^{-6} µm/s, which is comparable to many analogue experiments. Normal stress σ_N was always 5 MPa. In many cases, this value is the starting point for analysis of fault gouge mechanics (e.g. Saffer and Marone, 2003) and in some cases the upper boundary for geotechnical tests regarding soil mechanics (Mitchell and Soga, 2005). Thus, a whole range of experimental studies was available for comparison. Furthermore, 5 MPa is considered as a stress regime where grain fracture is minimal or non-existent (Mair et al., 2002). This is important from the modelling point of view, since particle fracture is not yet realised in our simulations.

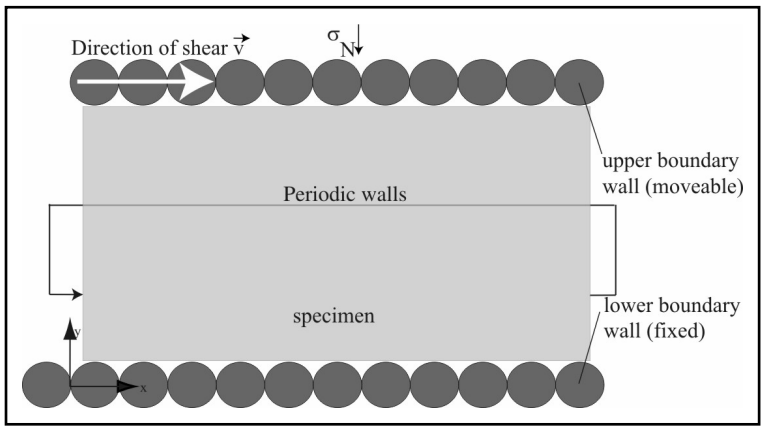

Fig. 8 Principle of numerical shear box. Dark grey: boundary particles. Light grey: place where the specimen is generated. For each specimen, see specifications in Chapter II-V.

Boundary particle size varies only in Chapter II, since boundary roughness is the modelled target parameter. In the other chapters, boundary particle size is constant (20µm diameter). Right and left walls were periodic; particles approaching the right boundary reappeared from

the left. Thus, the model was able to produce large amounts of strain/displacement, which makes the numerical model comparable to analogue ring shear tests. In most cases, shear box width was 200μm, but sometimes a deviation from that rule was necessary (see below). Note that since a constant normal stress should be maintained at the upper wall, shear box height varied during each model run.

In between these walls, the numerical sample (i.e. the 'silt', 'clay' and mixtures) were generated. Then, normal stress was applied to the upper boundary and the particle assembly was compressed. After compression, shear was applied. Sample configuration varies from chapter to chapter, due to model objectives outlined earlier: In Chapter I, the sample is pure 'silt', since boundary surface roughness is the variable parameter. Chapter II incorporates pure 'clay', since only 'clay' particle shape is investigated. Thus, in Chapter III, the specimen is stratified 'silt' and 'clay' and in Chapter IV a mixture of 'silt' and 'clay' particles. Sample configuration is explained in detail in every respective chapter.

It is very important to note that there is a difference between particle properties and overall macroscopic behaviour. In (our) simulations, initial particle properties are *assigned,* such as the particle coefficient of friction $\mu_{(P)}$. Particle properties are therefore denoted with sub- or superscript (P). Macroscopic behaviour and macroscopic properties of the particle assembly have to be *measured* (with the techniques outlined below), such as the overall coefficient of friction $\mu_{(M)}$. Macroscopic properties are thus denoted with sub- or superscript (M).

4.1.2 Analyzing techniques and tools

For each individual experiment, a set of analyses were carried out during model runs. Besides the measurements widely used in the laboratory, there are some techniques which are solely available in numerical studies. These allow studying micromechanics on a particle scale more closely.

Analyses were performed in the following ways:

(1) Instantaneous visualization:

In PFCD2D the displayed particles can be coloured. This was done using an alternating colouring to visualize the deformation process.

(2) Strain/Displacement:

Shear box strain was monitored by measuring horizontal wall displacement in relation to instantaneous shear box height. Both were measured continuously. For example, at a wall

displacement of 100µm and a box height of 120µm, strain was 83.3%. 200% of strain was reached in all model runs to make sure residual friction was achieved.

(3) Volume strain:

From continuous shear box height measurements, an analogue to 3-D volume strain could be calculated. The term volume strain was kept, but volume V is calculated by shear box height multiplied by shear box width. Volume strain δV then could be computed by

$$\delta V = \frac{V - V_0}{V_0} \quad (9)$$

where V is the instantaneous and V_0 the initial volume. Thus, positive values show dilation, negative values contraction. Volume strain was monitored at each 0.1% strain increment.

(4) Void ratio and void ratio change:

Since shear box and all particle volumes are known, void ratio ν could be determined by dividing shear box volume by total particle volume. From this, void ratio change, i.e. 2-D porosity, could be computed with

$$\delta \nu = \frac{\nu - \nu_0}{\nu_0}, \quad (10)$$

where ν is the instantaneous and ν_0 initial void ratio.

(5) Tracking of localization features:

At the beginning of each model run (after compression), particle displacement (x and y direction) and rotation was zero. After shear was induced, current particle position, current particle orientation (especially for 'clumps'), particle radius, accumulated particle displacement and accumulated rotation was monitored and written to file output at each 0.1% strain increment. Thus, a displacement vector and rotation scalar was available for each particle. With the GMT software package (Wessel and Smith, 1991) these data were processed.

The displacement field was separately gridded for each direction, so that an absolute horizontal and vertical displacement field was available. Then, also with GMT, normalized gradients from these displacement fields were calculated. These gradients consequently showed areas of low and high relative displacement. These areas indicate where a high amount of displacement localized and thus visualized slip planes and shear zones.

For rotation, the data were simply mapped with GMT, so that a colour code could be assigned to the particles' accumulated angle of rotation which was then plotted. Therewith, rolling of 'silt' and rotation of 'clay' particles could be visualized.

Especially for the elongated 'clay' particles, both the angle of rotation and the final orientation of particles were important. Basically, this was achieved with the same procedure as for rotation. With GMT, a colour code was assigned to particle angle of orientation, then plotted. Therewith, the evolution of 'clay' microstructure, particularly domains of preferred grain orientation could be shown.

(6) Frictional strength:

The interaction between all particles determines the deformation behaviour of the whole particle assembly. Therefore, overall friction $\mu_{(M)}$ was calculated using eq. (7). Overall normal stress is known, so only overall shear stress τ for the complete particle assemblage has to be calculated. There are in principle two ways to accomplish that:

a. Maximum resemblance to analogue shear tests is the calculation of wall friction. Here, shear stresses acting on all particles of both walls are summed up and then averaged.
b. A feature that can not be calculated in an analogue test is the calculation of an average friction for all particles in a particle assembly. To measure this, shear stresses of all sample particles are summed up and averaged.

Detailed outlines of complex calculation algorithms used for stress determination are given in the Appendix.

(7) Sliding fraction:

Sliding fraction is a micromechanical parameter which can be used to monitor deformation modes at contacts between particles. The sliding fraction gives the percentage of particles in a defined volume which do slide past another.

(8) Coordination number:

One particle may be neighbouring numerous particles. The actual number of contacts is given by the coordination number. This number allows assessment of how densely a particle assembly is packed so that micromechanical conclusions for dilation and contraction can be drawn.

(9) Contact forces:

The magnitude and the direction of acting contact forces between particles were monitored at each 1% strain increment. With GMT, these orientations and magnitudes could then be processed and plotted in histograms or rose diagrams.

Chapter II

A systematic study on the influence of boundary surface roughness on deformation of granular materials

Submitted: Ingo Kock & Katrin Huhn, Tectonophysics

Abstract

Geotechnical laboratory studies indicate that surface roughness does have some influence on the mechanical strength of fault gouge and soil. Systematic tests supply that the control of roughness in a laboratory test is hard to achieve. To overcome this problem we employ numerical modelling with the Discrete Element Method. With a numerical shear test we analyzed the effect of boundary roughness on deformation and frictional strength of a microscopic granular sample.

Variation in boundary roughness led to differences in stress transmission onto the sample. Depending on the maximum particle diameter of the sample, we found an upper and lower threshold level of roughness. In between these values, deformation was distributed throughout the sample. For a roughness smaller than the lower threshold value, no internal deformation occurs. Above the upper threshold value, deformation concentrates into many slip planes along the boundaries.

1 Introduction

Assessing the frictional properties of rocks and soils encompasses many different experiments. Two typical tests to measure shear strength of materials are the direct shear test (e.g Lambe and Whitman, 1969) and the ring shear test (Bishop et al., 1971). The former test is the oldest and simplest one. Here, the soil specimen rests inside a box consisting of two halves which can be displaced relative to each other. During the test a confining force is applied and the shear force necessary to cause displacement is recorded (Lambe and Whitman, 1969). In contrast, the latter one utilizes a ring in which the specimen is placed. Similarly, a confining pressure and circular movement are applied to the top ring. Thus, larger displacements can be accumulated (Bishop et al., 1971; Lambe and Whitman, 1969). A feature all types of laboratory experiments have in common is the need of a sufficiently rough wall surface, so that shear stress transmission from the box to the specimen can be achieved and slip directly at the boundary is prevented.

Some systematic studies on the influence of shear box surface roughness on the deformation behaviour and mechanical strength of rocks and soils exist (Anthony and Marone, 2005; Biegel et al., 1992; Dieterich, 1981; Marone and Cox, 1994; Sammis and Steacy, 1994). In general, these studies supply that for large displacements, increasing surface roughness causes an increase in mechanical strength. Chambon et al. (2006) supply that shear zones form directly at the boundary for both a rough and a smooth surface, but with significantly different interior deformation of the sample. These studies are also relevant for natural conditions and also apply to natural fault surfaces (Biegel et al., 1992; Dieterich, 1981) . That means that surface roughness of faults and country rock does play a role for deformation behaviour of faults.

However, a problem of these laboratory studies is control of the boundary conditions. Biegel et al. (1992) acknowledged that despite careful specimen preparation, shear box boundary walls (Westerly granite) of nominally the same roughness showed discrepancies in surface height (asperity) distribution. Furthermore, wear and abrasion of boundaries leads to changing of roughness during an experiment.

When considering natural shear zones or geotechnical tests, there are two types of roughness that can be important: (1) Overall roughness which is defined by the shape of the fault surface or boundary wall and (2) microscopic surface roughness. For example, the overall shape of walls in a direct shear box resembles a saw-tooth (e.g. Stenzel), while in a ring shear device

(e.g. Wykeham Farrance Bromhead ring shear) the wall is smooth with an indentation. Simultaneously, the walls can be composed of different materials, e.g. porous ceramics, non-porous steel or natural rocks, which exhibit a distinct microscopic surface roughness (e.g. Scott et al., 1994).

We conducted numerical modelling studies on the effect of boundary roughness on deformation of granular materials. For our simulations we use the Discrete Element Method (DEM), a technique based on a granular model approach. This method has a wide range of applications and has successfully been used for numerical investigation of micromechanical behaviour of granular materials (Abe and Mair, 2005; Guo and Morgan, 2004; Hazzard and Mair, 2003; Huhn et al., 2006; Kock and Huhn, 2006; Morgan, 1999; Morgan and Boettcher, 1999). We use a numerical testing setup which resembles a ring shear box setup.
Goals of our study are the analysis of localization and rotation patterns, to quantify differences in boundary and internal friction, and force distribution in a numerical granular material all as a function of boundary roughness. The advantage of such numerical tests over analogue ones is the control of a finite set of boundary conditions. Therefore, our numerical study varies only one shear box configuration parameter - roughness - while all others were held constant.
Some work regarding numerical simulation of surface roughness and its relation to granular shear zones has already been done by Jensen et al. (1999). Compared to them, we use a wider range of surface roughness and different methods to achieve a more detailed analysis of the micromechanics involved in deformation.

2 Method

2.1 The Discrete Element Method

In the applied 2D DEM code PFC2D (Cundall and Strack, 1978; Itasca, 2004), spherical particles interact according to simple physical contact laws. This tool allows the numerical modelling of deformation processes of granular material. The granular modelling approach with PFC2D so far implies that fluids are not considered. Additionally, we did not take grain fracture into account.
Inherent to the modelling approach are particle microproperties which have to be defined, such as particle coefficient of friction $\mu_{(P)}$. These parameters control particle - particle interaction. In contrast, overall properties, such as macroscopic friction $\mu_{(M)}$ of a particle assemblage have to be computed as the result of all particle interactions.

The complete numerical description of the code is outlined by Cundall (1987; 1989), Cundall and Strack (1978; 1979; 1983) and Itasca (2004). Short overviews are given in Antonellini and Pollard (1995), Kock and Huhn (2006) and Morgan and Boettcher (1999).

2.2 Modell

We developed a numerical shear box (Fig. 1a; Table 1; Table 2) which is comparable with other numerical DEM simulations (e.g. Guo and Morgan, 2004; Huhn et al., 2006; Kock and Huhn, 2006; Morgan, 1999; Morgan and Boettcher, 1999) and analogue ring shear experiments (e.g. Ask and Kopf, 2004; Kopf and Brown, 2003; Saffer et al., 2001; Saffer and Marone, 2003).

The lower and upper boundary wall of the shear box consisted of particles whose diameter and geometry was constant for each experiment, but varied between experiment series to reproduce different roughness. Our numerical sample embedded in this box resembles natural silt (Fig. 1a; Table 1). As silt grains appear approximately spherical in shape in nature (Bennett et al., 1991b), the numerical 'silt' is simulated by ideal spherical particles. Diameters

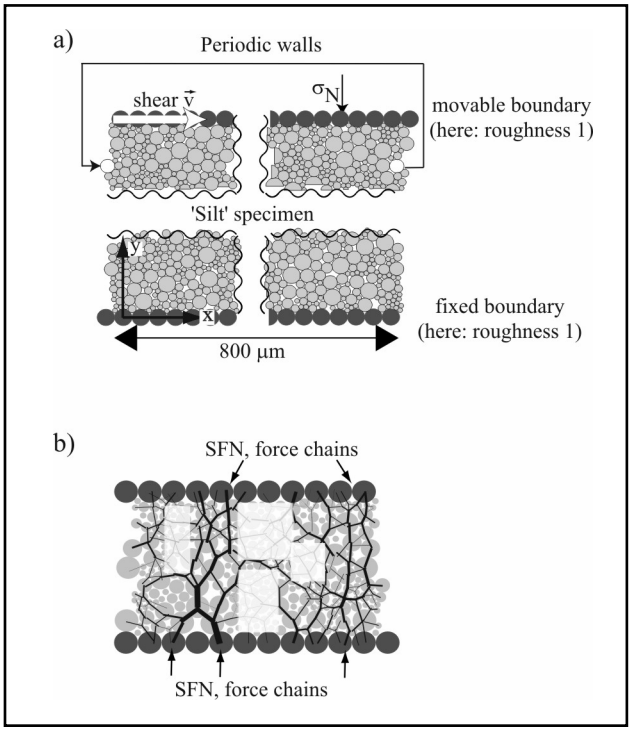

Fig. 1 a) Cutoff of DEM model of 2D shear box experiment. Arrows show the periodic feature of the box: both white particles on either side are the same particle. Indicated in medium grey is the 'silt', comprising of spherical particles. Dark grey are boundary particle 'walls'. b) Sketch of force partitioning. Black bars indicate forces between particles; their thickness is scaled to force magnitude. Arrows indicate beginning of strong force network (SFN) and force chains extending from the top and bottom wall. Transparent white boxes show areas of weak force network (WFN).

of these particles are log-normal distributed (e.g. Füchtbauer, 1988; Tucker, 1981) and range between 5.6µm to 20µm and a peak value at 10µm. This particle size distribution (PSD) was constant in all experiments.

We defined roughness according to a fixed reference frame. The reference frame in our case is maximum particle diameter of the 'silt'. Accordingly, a roughness of 1 equals a wall particle diameter of 20µm. Other roughness were referenced to this (Table 2). So a roughness of 20 meant that a wall particle had 20 times the diameter of maximum particle size in experiment R20 (400µm). In most cases, shear box width was held constant at 800µm. Hence, the number of wall particles varied simulating a different roughness. To let the wall consist out of at least 2 particles, shear box width was increased to 1600µm for experiment R40.

Table 1: Fixed properties and configuration of numerical models.

Properties:	All experiments
Height [µm] (initial)	560
Normal stress σ_N [Pa]	$5x10^6$
Shear velocity [µm/s]	6
Particle number:	3895
Particle properties	
Normal stiffness k_N [N/m]	$1x10^9$
Shear stiffness k_S [N/m]	$1x10^9$
Density ρ [kg/m³]	*
Diameter [µm]:	5.6 - 20
Particle coefficient of friction □$_{(P)}$	0.1

In a second experiment series, shear box walls were not built up by particles rather by smooth walls (Experiment T, P; Table 2). These were designed to compare configuration of a direct (experiment T) vs. a ring shear apparatus (P) used in laboratories (Stenzel direct shear and Wykeham Farrance Bromhead ring shear). In experiment T walls were saw-tooth shaped while experiment P had smooth walls with an indentation. Considering differences between the highest and lowest point of a wall, these experiments had a roughness of 12.0 and 7.0.

To achieve maximum comparability, experiments were all executed in the same way (Table 1). The lower wall remained fixed in x- and y-directions throughout all experiments. As the upper wall could move in the x- and y-direction, shear ($\tau_{(M)}$) and normal stress ($\sigma_{N,(M)}$) were induced upon the specimen. Shear rate and normal stress were constant at 1µm/s and 5MPa, respectively. Hence, shear box height varied during each experimental run.
Left and right box boundaries were periodic, so that particles which moved out of the right side reappeared on the left. That way, large quantities of strain (200%) could be modelled.

Table 2: Variable properties and configuration of numerical models.

	Experiments						
Properties:	**R0.05**	**R0.1**	**R0.125**	**R0.25**	**R0.5**	**R1**	**R2**
Roughness	0.05	0.1	0.125	0.25	0.5	1.0	2.0
Width [µm]	800	800	800	800	800	800	800
Number of balls per wall	800	400	320	160	80	40	20
Properties:	**R4**	**R8**	**R10**	**R20**	**R40**	**(T)eeth**	**(P)ocket**
Roughness	4.0	8.0	10.0	20.0	40.0	12.0	7.0
Width [µm]	800	800	800	800	1600	800	800
Number of balls per wall	10	5	4	2	2	n.a.	n.a.

2.3 Measurements

Throughout the experiments up to shear strains of 200%, different macroscopic material properties were measured.
Internal deformation was analyzed at the final stage of the experiments. After 200% strain, relative displacement and angle of rotation ('rolling') of each particle were calculated. Relative displacement was computed by recording absolute displacement continuously and calculating normalized gradients of these data with GMT (Wessel and Smith, 1991). Displacement gradients and angle of rotation monitor internal deformation and mark the position of slip planes and shear zones (Guo and Morgan, 2004; Huhn et al., 2006; Kock and Huhn, 2006; Morgan and Boettcher, 1999).
Macroscopic friction $\mu_{(M)}$ was calculated by measuring shear stress $\tau_{(M)}$ divided by applied normal stress $\sigma_{N,(M)}$. We computed shear stress $\tau_{(M)}$ in two ways: (1) The average shear stress acting on both walls which gives friction of potential detachments along the walls $\mu_{(M),basal}$

and (2) the average shear stress acting on the specimen, the internal friction $\mu_{(M),interior}$ of the material.

A feature of granular materials is their heterogeneous internal force distribution between particles (e.g. Radjai et al., 1998). The total amount of forces partitions in a strong and a weak force network (Fig. 1b). Strong force network means that the minority of contacts carries the majority of force; thereby building force chains connecting the upper and lower boundary. Equivalently, the majority of contacts carrying the minority of force are called the weak force network. To determine the influence of roughness on the evolution of these networks, force orientations and magnitudes between particles were calculated at the beginning and at the end of each model run. Magnitudes were then normalized by the mean acting force between particles. Values above the mean belong to the strong force network, below to the weak force network. The analysis of force networks allows us to closely examine changes of micromechanical behaviour inside the specimen as a function of boundary roughness.

Furthermore, the total number of contacts acting on the walls and the average coordination number of a wall particle or a wall segment were calculated. Computation of these features enables us to examine for example how force transmission form walls to sample changes with roughness.

3 Results

3.1 Internal deformation

Roughness had an obvious effect on localization patterns (Fig. 2). Below a roughness of 0.5 no internal slip planes and only negligible particle rotation could be observed (Fig.2, R0.25) except at the top wall. The roughness threshold level for interior deformation was 0.5. At this level, slip planes and particle rotation occurred further away from the walls, but the intermediate part still showed no internal deformation features (Fig.2, R0.5). An increase of roughness to values >0.5 and <4.0 led to more distributed slip planes and abundant rolling inside the specimen (Fig.2, R1.0-R2.0). Furthermore increasing wall particle size to 20.0 showed multiple slip planes and rolled particles at the bottom and top position of the upper and lower boundary walls, respectively. No slip planes and rolling were observed in the 'pockets' between these particles.

Experiments T and P showed significant differences. Experiment T showed a concentration of slip and rotation at the boundary edges, but also a measurable amount of internal deformation in the specimen (Fig 2). In contrast, experiment P only displayed some localization features along the walls, especially around the base/top of the pockets.

3.2 Friction

For the two types of friction (basal and internal) different results were calculated. In case of friction measured inside the material, a clear trend to increasing friction with increasing roughness could be observed: For a roughness of 0.25, average friction was $\mu_{(M),interior}$= 0.23 (Fig. 3a). In this experiment, friction showed stick-slip behaviour (e.g. Scholz, 2002) with a very regular oscillation around 0.23 (Fig. 3b). For roughness between 0.5 and 2.0, average $\mu_{(M),interior}$ ranged between 0.35, 0.38 and 0.4 for experiments R0.5, R1.0, and R2.0, respectively (Fig. 3a). Complete stable sliding could not be reached, since variability of these curves was still relatively high, but without an oscillating pattern. Furthermore increasing roughness to 20.0 resulted in highest friction values of ~0.55.

Lowest friction values of 0.14 exhibited experiment P and thus did not fit in the trend of increasing friction with increasing (Fig. 3a). Friction of experiment T did show a slight drop to 0.4. Both of these experiments showed only slight variability in their curves, so stable sliding was reached.

For basal friction $\mu_{(M),basal}$, no systematic trend was obvious and values were consistently lower than for interior friction (Fig. 3a). For the lowest roughness in experiment R0.25, lowest friction of $\mu_{(M),basal}$ = 0.06 was measured. Here, the curve once more showed a regular oscillating pattern (Fig. 3b). Increasing roughness to 0.5, 1.0, and 2.0 led to highly variable curves with average $\mu_{(M),basal}$ of 0.16, 0.176, and 0.17, respectively (Fig. 3a). Furthermore increasing roughness to 20.0 showed lower friction values of 0.098. Experiment T exhibited highest peak wall friction and average friction values in the upper range with $\mu_{(M),basal}$ = 0.17. In contrast, experiment P showed intermediate wall friction values.

Fig. 2 (next page) Deformation features of selected experiments. a) Relative horizontal displacement plots after 200% strain. b) Particle rotation after 200% strain.

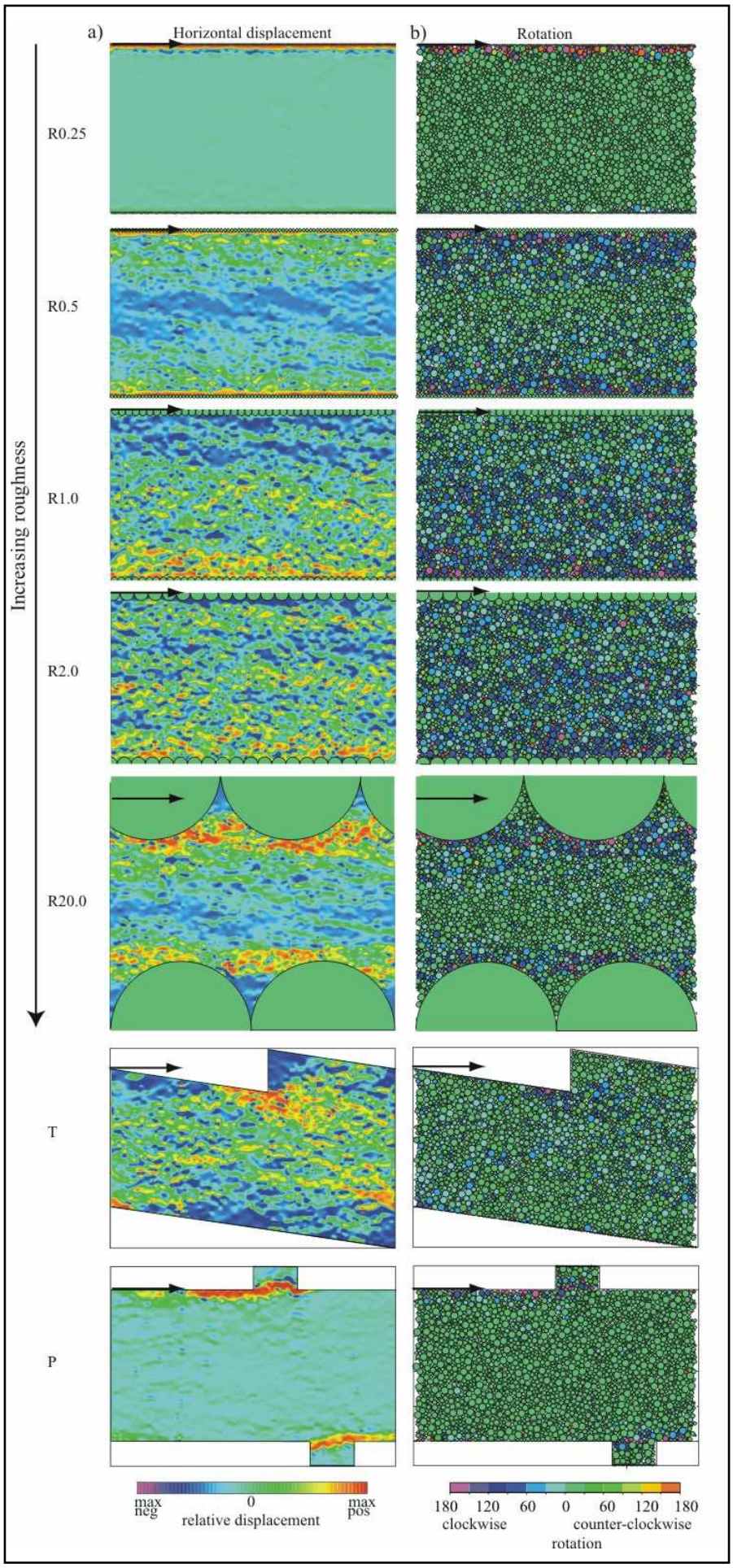
a)
Horizontal displacement
b)
Rotation
Increasing roughness
R0.25
R0.5
R1.0
R2.0
R20.0
T
P
max neg
0
max pos
relative displacement
180 120 60 0 60 120 180
clockwise
counter-clockwise
rotation

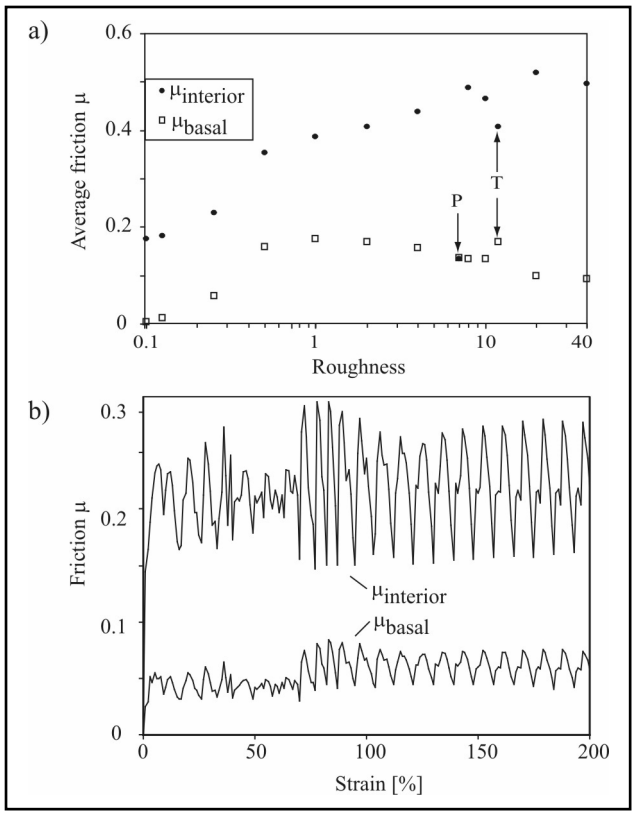

Fig. 3 Macroscopic friction for all model runs. a) Average friction. b) Basal and interior friction for experiment R0.25.

3.3 Contact force distribution and orientation

At the beginning of each experiment, the force orientations of the strong and weak network were distributed evenly. Hence, in Fig. 4 only the orientation of the strong and weak contact forces networks at the final stages of some experiments are shown exemplarily. For low roughness of 0.25, only a slight reorientation of strong forces towards shear direction could be observed; there are still abundant orientations around 0° (Fig. 4, R0.25). Orientation of weak forces did not change significantly. When roughness was increased to 0.5, contact forces reorient themselves into shear direction. Reorientation is greater for strong contact forces. Furthermore increasing roughness showed no change in this trend. In all experiments, contact forces reoriented along shear sense.

Experiment T and P also showed progressing reorientation of contact forces after 200% strain. However, experiment T still shows a sharp peak at 0° orientation angle.

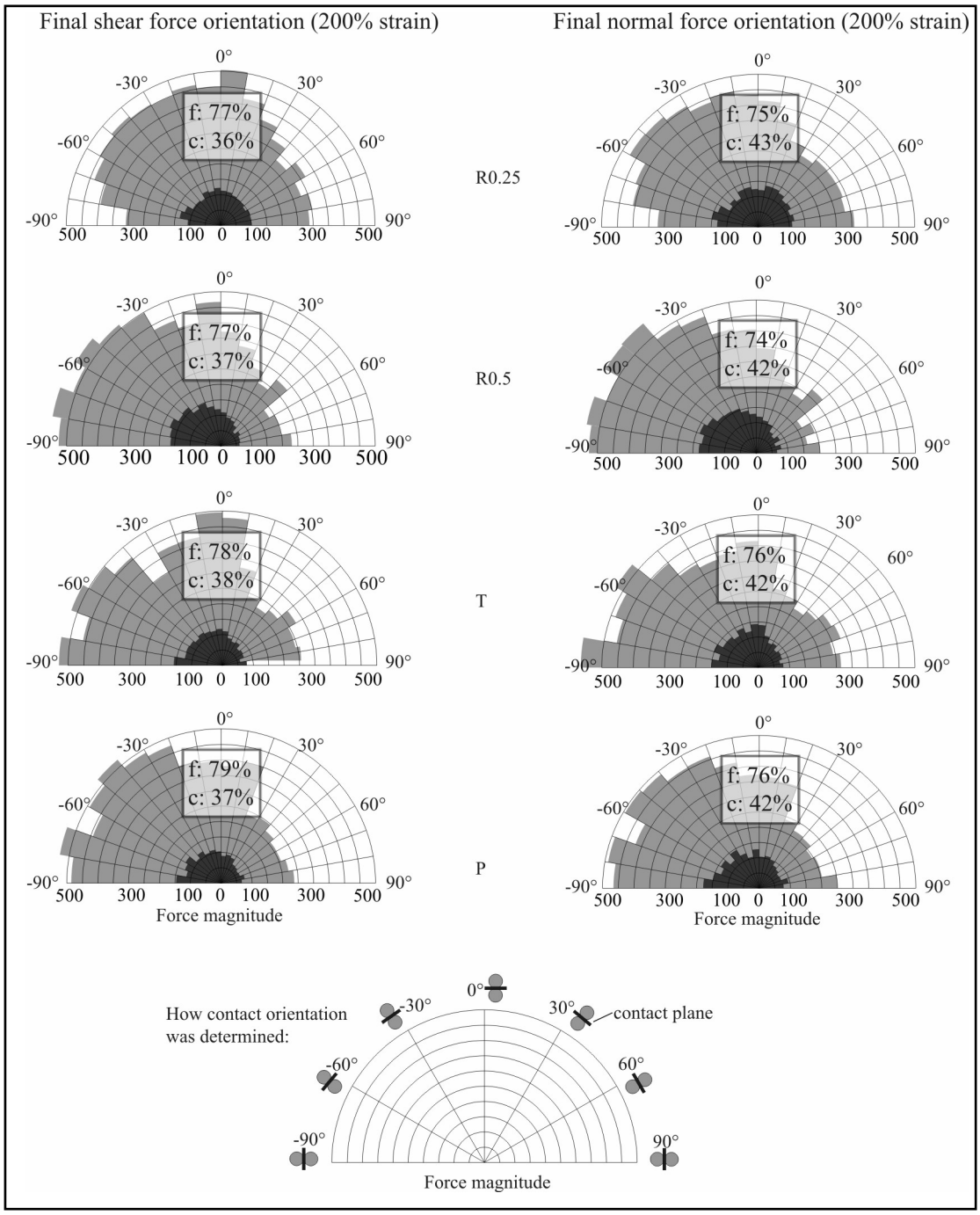

Fig. 4 Orientation and magnitude of particle forces. Magnitudes are scaled by mean force. Grey: strong force network (Force magnitude above mean force). Black: weak force network (Force magnitude below mean force). Numbers in boxes are: f: percentage of force transmitted by strong force network; c: percentage of contacts which belong to strong force network.

3.4 Wall contacts

The total number of particle contacts depends on wall roughness (Fig. 5a). For low roughness < 0.25, contact numbers reached values of more than 250. High roughness > 4 yielded contrasting tendencies, so that number of particle contacts decreased strongly. Intermediate roughness exhibited particle contact numbers lying on a plateau around 200.

The average coordination number of each particle, or segment, comprising the wall, also depends on wall roughness but shows a different trend (Fig. 5b). Increasing roughness exhibits a steady increase of coordination number.

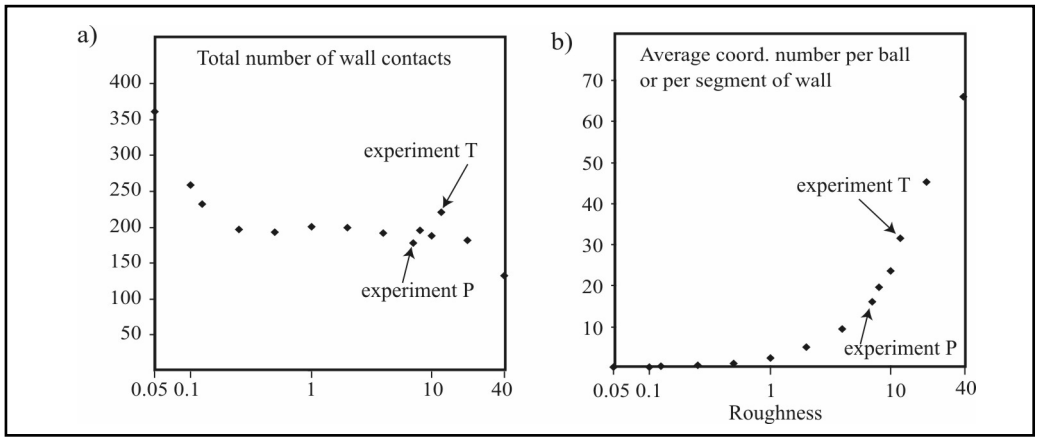

Fig. 5 Wall properties. a) Total number of contacts for top and bottom wall. Number is averaged from 0 to 200% strain. b) Coordination number per wall particle/segment from top and bottom wall. Number is averaged from 0 to 200% strain.

4 Discussion

Roughness of boundary walls or country rock is a sensitive parameter which influences geometry of shear zones, general deformation behaviour (active/non-active stick-slip), frictional strength of the material and the basal friction along a boundary detachment.

Low basal friction indicated detachments closely related to the wall positions, which was the case for R0.25 and R20.0 which simulate two extreme end members of boundary roughness. For R0.25 the walls decoupled and slid over the sample (Fig 6a). Contact force orientation supplies that stress transmission from the wall to the sample was prohibited. For R20, the detachment lay close to the wall (Fig. 6b), but the interface was broader and wall decoupling did not happen, stress transmission was still active. Both these observations are in concordance with laboratory measurements from Chambon et al. (Chambon et al., 2006) Intermediate roughness (0.25 < roughness < 4) between the two extreme cases led to distributed shear (Fig. 6c).

The reason for different ability to transmit stress onto the sample was the geometry of the walls which significantly influenced particle contact number and coordination number. For low roughness, the total count of contacts was high, but coordination number was low, so that stress was only transmitted via few relevant contacts. Since the whole shear force acting on the sample relied on such few contacts, the whole wall began to slide, if few contacts slipped. The orientation of interior force chains remained almost unaffected from this. When the wall was slipping, the only contact forces which could reorient were those of the very few particles where slip occurred. Shear force orientation within the sample was solely depended on contact force orientation of interior particles and independent of wall particles.

For high roughness, shear stress from a wall particle was transmitted to fewer particles altogether, but since coordination number was higher, stress was transmitted via more relevant contacts. If slip occurred between a wall and few neighbouring sample particles, sliding of the complete wall could not begin.

Thus, when sliding occurred, particle forces between wall and all adjacent sample particles had to reorient into a direction indicating sense of shear. This reorientation then was transmitted by the strong and weak force network to all particles within the sample.

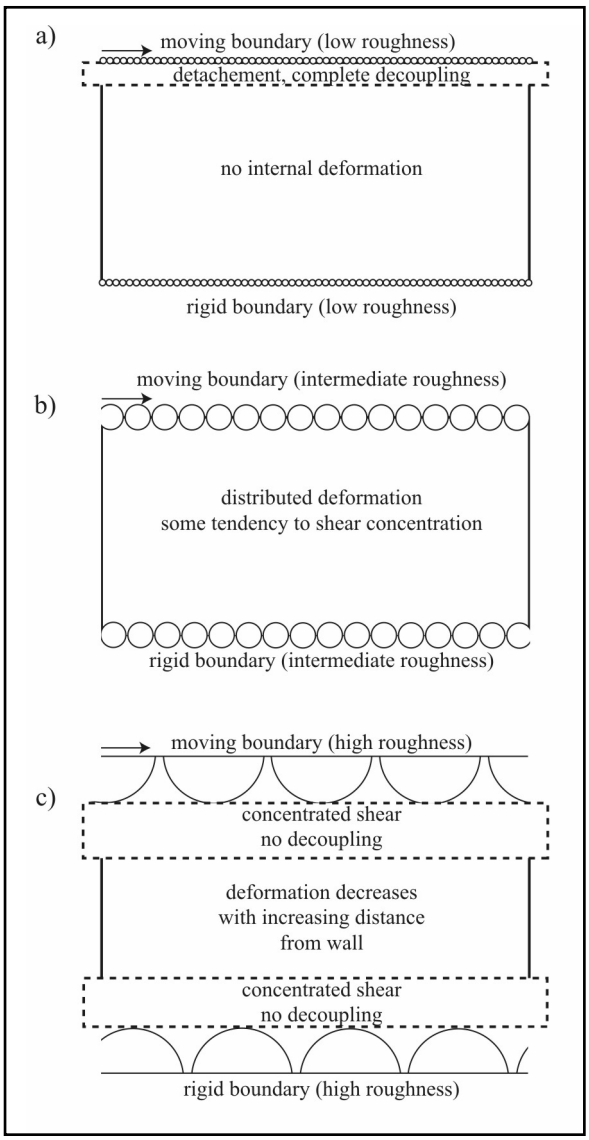

Fig. 6 Conceptual model for deformation behaviour in relation to boundary roughness. a) Low roughness, highly below the maximum particle size. b) Intermediate roughness, around maximum particle size. c) High roughness, highly above maximum particle size.

4.1 Implications for natural conditions

For natural materials, the results indicate that deformation of rocks and soils does not only dependent on their respective material properties, but also on the roughness of the country rock and its relation to the material's maximum particle size. The influence of grain comminution has been discussed in the previous section, but for natural fault zones the progressing of wear is hardly understood. As fault gouge develops by wear of fault surfaces (e.g. Scholz, 2002), surface roughness of faults continuously changes (Wang and Scholz, 1994). However, from our study some inferences could be made regarding the relation of fault surface roughness and grain size distribution (GSD) of the gouge. We suppose that different surface roughness implies different geologic settings or different stages of deformation progression. A high surface roughness of a fault may indicate that deformation has not progressed very far and fault displacement is low, since the difference in asperity height and PSD still is great. Intermediate roughness of ~1 means, that the country rock is essentially similar to the sample material. Low roughness then would indicate that shearing occurs at pre-existent unconformities, e.g. lithological boundaries or that the fault already has accumulated much displacement. The latter would indicate that wear has already reached the steady state stage (Wang and Scholz, 1994).

4.2 Implications for numerical experiments

Our numerical study shows a strong influence of roughness on shear, deformation, localization, friction and micromechanics of the numerical sample. Other DEM and LSM models are likely to also be affected, so differences in deformation behaviour of fault gouge observed by other modellers (Guo and Morgan, 2004; Mora and Place, 1994; Morgan, 1999; Morgan and Boettcher, 1999) can at least partly be explained. Our results also confirm observations from Jensen et al. (1999), who stated that shear at boundaries becomes a simple frictional sliding problem for smooth walls. Therefore, when conducting numerical experiments, the effect of surface roughness of boundaries has to be considered, when results of models are discussed.

Our results indicate that by choosing a defined roughness for a model, it is possible to influence the default mechanical behaviour of the complete material: For example, a rough boundary implies that slip interfaces will concentrate at boundaries. This kind of setting may be relevant for models, where the goal is to model pre-existing detachments or basal décollements of large scale tectonic settings. Intermediate roughness on the other hand is best suited to investigate distributed deformation, and where the focus of study lays in the start of

localization of an intact specimen. Low roughness experiments may be of interest to analyze the transition from stick-slip like displacement to smooth sliding, but are not applicable to study internal deformation of soils or fault gouge.

4.3 Laboratory experiments

Within the limitations of our model (e.g. no grain fracturing), we can transfer our results to laboratory conditions. Biegel et al. (1992), Chambon et al. (2006), Dieterich (1981) and Sammis and Steacy (1994) observed an influence of roughness on the strength and on localization patterns in their laboratory shear experiments. However, they did not observe an upper or lower threshold roughness, since they used only 3 (2) different instances of roughness and a very angular grain shape.

Our results indicate that for laboratory experiments, where localization, friction, time and rate friction laws are studied, scaling of roughness in relation to particle size should not be a neglected parameter. To preclude the existence intense shear at test setup boundaries, a roughness in the order of the PSD should be chosen.

Furthermore, in a complex setting rouhghness may at least be a supplement to explain frictional strength. For example, Dieterich (1981) showed that strength increased with the relative amount of fine grain size fraction. He concluded, that grain comminution in a gouge would then increase frictional strength of the gouge. Additionally, the frictional strength could be increased because the relative surface roughness of the boundary increased. That could only happen if grain comminution decreases maximum grain size which was demonstrated in laboratory studies by Gu & Wong (1994).

In case of laboratory experiments to model large scale tectonic processes, such as sandbox studies, roughness of materials to simulate potential detachments also may be important. In such large scale experiments it has been recognized that the properties of a material which simulates properties of real rock have to be carefully chosen (e.g. Koyi, 1997; Lohrmann et al., 2003). The same should apply to the boundary conditions, e.g. in case of sandbox prism evolution, to the underlying basal interface or a weak intermediate layer, which should have appropriate surface roughness not only to cause deformation, but to scale to real conditions to achieve results that are comparable to nature. For example, to model basal décollements, a great roughness would be needed. Thereby, a detachment forms at the boundary, but complete decoupling is prohibited and forces are still transmitted to the upper layers.

5 Conclusions

We have shown that boundary roughness of shear cells and host rocks has a significant influence on shear localization and micromechanics. Stress transmission close to the boundaries varies with roughness via the number of relevant contacts. Forces acting between particles can only be influenced by shear stress, if a roughness threshold level is exceeded.

There exists a lower threshold level of 0.25 for shear box walls or host rock in relation to the maximum particle diameter inside the specimen. Below this roughness, no internal deformation occurs. The boundary then behaves as one side of a detachment interface.

There exists an upper threshold level of 4. Above this level deformation concentrates into many slip planes thereby creating distributed shear. These slip planes themselves localize at the respective top and bottom of the boundary asperities.

In between threshold levels deformation becomes distributed throughout the sample. Types of deformation include slip and rotation, both of which coincide on the area where they happen.

Roughness of country rock influences deformation behaviour of faults. When particle size distribution of a fault gouge or a soil equals the roughness of country rock, deformation may be distributed by default. If PSD and roughness are highly different, shear will likely be concentrated around the boundary, either by complete decoupling or by concentrated shear zones along the boundaries.

For laboratory analogue conditions boundary roughness controls deformation behaviour. Thus, by choosing a specific boundary roughness, a specific geological setting is pre-defined.

Acknowledgements

Funding for this research has been received through Deutsche Forschungsgemeinschaft via the Research Center Ocean Margins (RCOM). This is RCOM publication # xxx.

We thank reviewers. We owe many thanks to our colleague Achim Kopf from the Research Center Ocean Margins for advice and discussions.

Chapter III

Influence of particle shape on the frictional strength of sediments - a numerical case study

Published: Ingo Kock & Katrin Huhn, Sedimentary Geology, 2006,
*d*oi:10.1016/j.sedgeo.2006.07.011

Abstract

Numerous direct and ring shear tests supply that composition and texture of sediments are crucial for shear and frictional strength. We simulate particle interactions on a micro-scale level during shearing with a numerical shear box using the Discrete Element Method (DEM). Based on the granular model approach detailed information about slip localisation and rates, forces at particle contacts, as well as particle rotation can be quantified as function of particle shape, stress conditions, and shear rate. Our numerical experiments show that the deformation behaviour of 'clay' is largely controlled by their particle shape. Two key factors, sphericity and roughness, could be identified as relevant for frictional strength, shear zone development, and particle rotation with sphericity dominating over roughness.

Decreasing sphericity leads to complex initial microfabrics whose breakdown with increasing strain is caused by particle rotation. Preferred particle orientation favours low friction, decreasing volume strain, and the evolution of particle domains of similar orientation. Decreasing roughness results in particle interlocking of different degrees which obstructs slip and rotation to preferred orientations so that friction is high and volume strain positive.

Spatial and temporal shear zone development depends on the roughness of particles. Increasing roughness precludes shear zone development and particle domain evolution. Shear zone localisation depends on particle sphericity. Increasing sphericity leads to more localised but vertically dilated deformation.

1 Introduction

During the last decades, numerous geotechnical experiments were carried out to determine the mechanical behaviour of sediments under static and dynamic stress conditions. These experiments indicate that the composition and texture of sediments are crucial for their shear strength and friction coefficient (μ) (e.g. Ask and Kopf, 2004; Kopf and Brown, 2003; Krantz, 1991; Marone, 1998; Saffer et al., 2001; Saffer and Marone, 2003). Lowest friction was measured for clay-rich sediments under different stress conditions whereas sandy materials showed a stronger frictional strength (Bos et al., 2000; Logan and Rauenzahn, 1987; Lupini et al., 1981; Morrow et al., 2000; Morrow et al., 1992; Saffer and Marone, 2003). Hence, the presence of clay minerals could be identified as an important controlling parameter for the shear strength of sediments (e.g. Huhn et al., 2006; Saffer and Marone, 2003). Today it is widely accepted that faults or shear zones are characterized by occurrence of clay minerals, e.g. at basal shear planes of gravitational mass flow events, at basal detachments, at active convergent margins, or at microscopic failure zones (Ask and Kopf, 2004; Hampton et al., 1996; Kopf and Brown, 2003; Morrow et al., 1992; Müller-Vonmoss and Kohler, 1993; Saffer and Marone, 2003).

To gain a deeper insight into the influence of sediment texture on the mechanical behaviour of clays, only few studies have been carried out which combine Transmission Electron Microscopy (TEM) of clay minerals with analogue experiments (e.g. Djéran-Maigre et al., 1998). Detailed microscopic analyses of deformed clay structures supply the tabular geometry of clay grains as a crucial parameter for their mechanical behaviour (Bennett et al., 1991a). In addition, it has been suggested that the alignment of tabular clay minerals leads to the reduction in frictional strength (Lupini et al., 1981; Saffer et al., 2001; Saffer and Marone, 2003) whereas Müller-Vonmoos and Kohler (1993) give the small grain size as an important property. However, detailed information about exact mechanisms occurring during the shear process at grain contacts remain unobservable from analogue tests.

Hence, the main purpose of our study is to examine influences of particle shape for the mechanical behaviour of a material package on a micro-scale level. In particular, we study the role of particle sphericity and roughness in four steps: (1) variation of particle configuration; (2) development of slip planes and shear zones; (3) degree of particle rotation and domain evolution; (4) relationship between friction, volume strain, porosity, and material texture.

Since we want to quantify the influence of particle shape on deformational behaviour of sediments, we adopted microstructure/texture of clays and silts as observed by various authors

(e.g. Bennett et al., 1991b; Lambe and Whitman, 1969; Mitchell and Soga, 2005). We compare the mechanical behaviour of different tabular 'clay' shaped particles and an ideal spherical 'silt'. Throughout this study the term grain is used for natural sediment and the term particle for the modelled material.

We developed a numerical shear box using the Discrete Element Method (DEM; Cundall and Strack, 1978). This technique has been successfully applied to investigate influences of particle shape in high pressure shear zones (e.g. Guo and Morgan, 2004; Morgan, 1999; Morgan and Boettcher, 1999), the evolution of shear bands in sandstone (e.g. Antonellini and Pollard, 1995), and kinematics of submarine mass movements (Campbell et al., 1995).

2 Sedimentological background - Microscopic texture of sediments

Clays are clastic sediments with a grain size <2µm (Heiling, 1988). The most important clay mineral groups are kaolinites, illites, and montmorillonites (e.g. smectites) which are characterized by different grain shapes. Kaolinites have a hexagonal sheet-like structure, but often aggregations of grains are rolled together (Köster and Schwertmann, 1993; Mitchell and Soga, 2005). Illites display a sheet-like configuration with irregular bordered and blurred edges or a rod like structure with blurred or spliced endings (Köster and Schwertmann, 1993). Smectites are often parallel aligned thin sheets with irregular edges and thicknesses (Mitchell

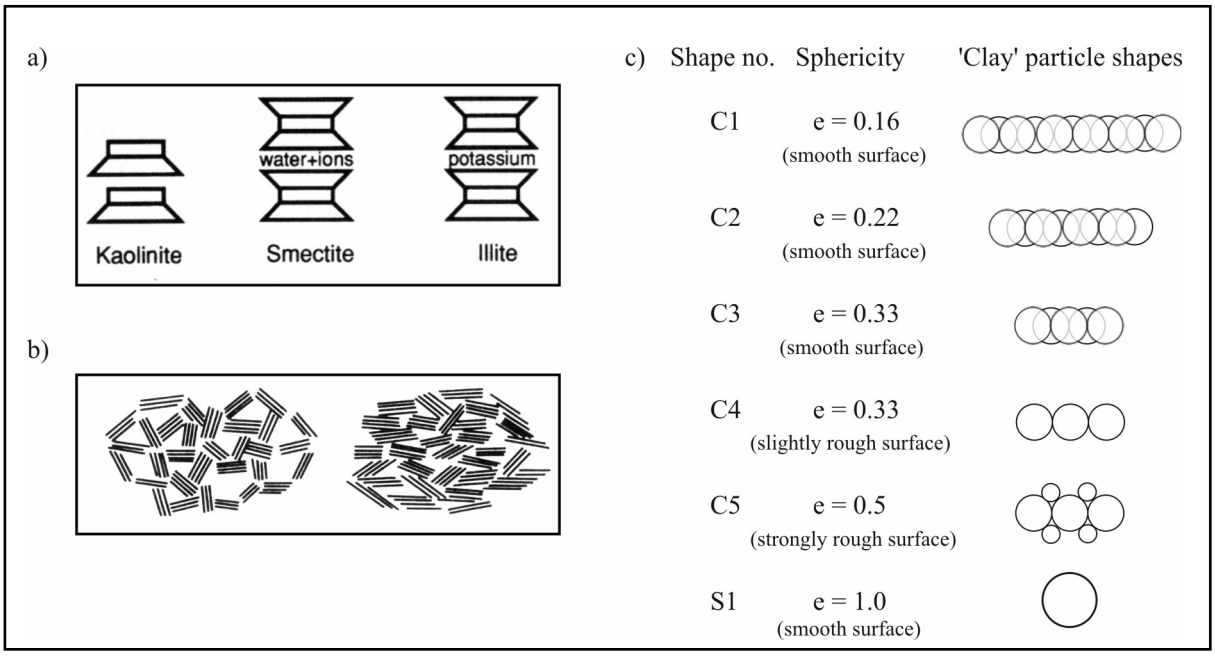

Fig. 1 a) Different types of clay grains. Modified from Mitchell and Soga (2005). b) Sketch of clay grain associations (domains). Left: edge to face association building a bookhouse structure. Right: edge to face and face to face association building various book-sheet structures. Modified from Mitchell and Soga (2005). c) Particle shapes used in numerical models. Sphericity is short vs. long axis.

and Soga, 2005) and a bent or folded shape (Lagaly and Köster, 1993) or lamellas of board- or rod-like crystals (Köster and Schwertmann, 1993).

This mineral organization of clay on a microscopic scale is based on electrostatic forces, e.g. the attractive van-der-Waals force (Bennett et al., 1991b). For this reason, clay grains are composed of multiple layers of single clay minerals (Fig.1a). In addition, clay microfabric consists of many grain associations (domains; Fig 1b). A domain describes a region with parallel clay grains (Bennett et al., 1991b; Mitchell and Soga, 2005). These domains may be stacked in different ways. The different types of grain associations are termed by their appearance, e.g. book-sheet, stair-step, card-house, bookhouse, etc. (Bennett et al., 1991b; Mitchell and Soga, 2005) or by their mode of association (edge to edge, edge to face, face to face; Fig. 1b). Furthermore, different microfabric structures contribute to different mechanical behaviour due to internal kinematic constraints when the fabric has to change during deformation (Lambe and Whitman, 1969; Mitchell and Soga, 2005).

Hiltmann and Stribrny (1998) compiled characteristic grain features such as diameter and thickness of single layers and the number of layers for kaolinite, smectite and illite (Table 1) which serve as input parameters for our simulations. Opposite to tabular clay minerals silt grains are characterised by a rounded shape with diameters of 2µm to 63µm and often show a log normal distribution in sediments (e.g. Füchtbauer, 1988; Tucker, 1981). However, compared to clay minerals, silt grains can assumed to be approximately spherical particles with a sphericity of ~1 (e.g. Bennett et al., 1991b).

Table 1: Clay mineral and grain characteristics.

Mineral features from Hiltmann and Stribny (1998)	**Kaolinite**	**Smectite**	**Illite**
Layer thickness [nm]	0.71	0.91	0.91
Min. number of layers	25.00	5.00	5.00
Max. number of layers	80.00	12.00	80.00
Min. diameter of mineral [nm]	100.00	30.00	100.00
Max. diameter of mineral [nm]	5000.00	300.00	5000.00
Calculated grain features			
Min. thickness of grains [nm] (layer thickness * min. number of layers)	17.75	4.55	4.55
Max. thickness of grains [nm] (layer thickness * max. number of layers)	56.80	10.92	72.80
Min. sphericity (Min. thickness of grain / Min. diameter of grains)	0.18	0.15	0.05
Max. sphericity (Min. thickness of grain / Min. diameter of grains)	0.57	0.36	0.73

3 Model Configuration

3.1 Discrete Element Method - PFC2D

The Discrete Element Method (DEM) is a numerical modelling technique based on the description of the mechanical behaviour of granular materials. We use the commercial 2D Particle Flow Code (PFC) by Itasca, Inc.® (Itasca, 2004) based on the DEM theory by Cundall and Strack (1978). A material is built up by ideal spherical particles (discs, cylinders, spheres). These particles may be bonded together to form complex particle shapes (Fig. 1c). The particles interact according to physical contact laws.

In Appendix B we briefly present the algorithms involved in the numerical code. A complete description of the numerical procedure is given by Cundall and Strack (1978; 1979; 1983), Cundall (1987), and Itasca (2004).

As a consequence of the granular approach material properties of a single particle determine particle-particle interactions and therewith the microscopic deformational behaviour (Cundall and Strack, 1979). It is important to note that the macroscopic properties of a material package, e.g. the bulk friction of a particle assemblage ($\mu^{(M)}$), result from the interaction of all particles and differ clearly from the assigned microproperties (e.g. particle coefficient of friction $\mu_{(P)}$). These macroproperties have to be calculated from shear box experiments (e.g. Morgan, 1999).

In the appendix as well as in the following sections assigned microproperties are denoted with subscript (P) and measured macroproperties are denoted with the superscript (M).

This granular approach also implies that fluids are not considered in the model and that particle breakage under high stress conditions has not been taken into account.

3.1.1 Numerical shear box

Consistent with analogue shear box experiments we developed a 2D numerical shear test (Fig. 2c; Table 2). We used two shear boxes with identical configurations but different dimensions: (1) a small box was used to investigate 'clay' sediments. This box consisted of an upper and a lower boundary wall made of 10 identical spherical discs with a diameter of 20µm. So the total width of the shear box was 200µm. (2) A larger box was used for 'silt' particles. The upper and lower wall of this box consisted of 40 identical spherical discs of a diameter of 20µm, resulting in a total width of 800µm.

In both shear boxes the lower wall was fixed whereas the upper one could move in x- and y-direction to induce normal ($\sigma_N^{(M)}$) and shear ($\tau^{(M)}$) stresses (Fig. 2c). To hold the normal

stress $\sigma_N^{(M)}$ at a constant value (5MPa) at each calculation cycle, a servo algorithm was applied to the upper boundary. Therefore the height of the shear box was variable. The initial height was regularly 140µm and 650µm for the small and large box, respectively. Left and right box boundaries were periodic walls so that particles which moved out of the right boundary reappeared on the left one (Fig. 2c). Approx. 6000 particles were randomly positioned inside this box to create the numerical 'sediment' layer. These model configurations were held constant during all experiments.

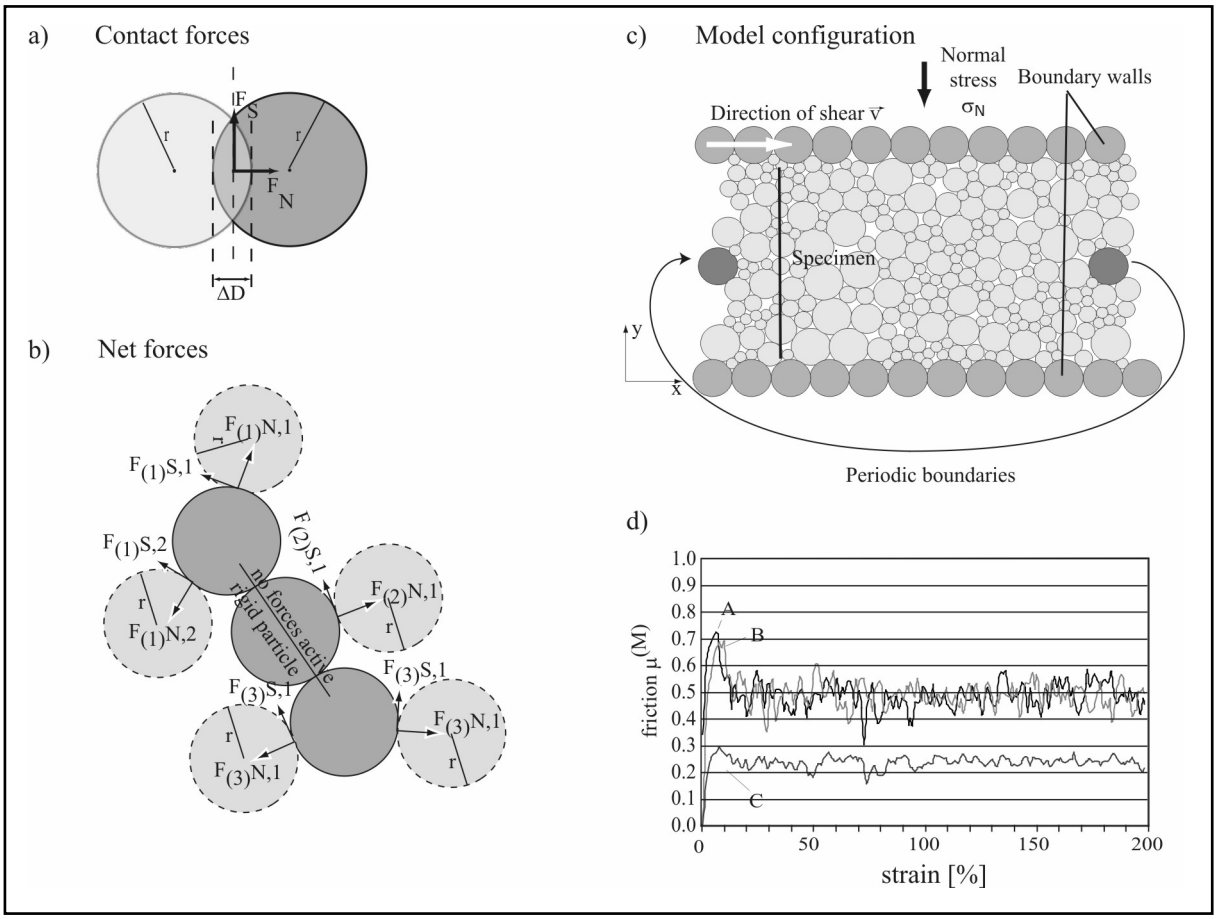

Fig. 2 a) DEM principle of contact force calculation b) DEM principle of net force calculation using rigid particles. Dark grey particles: rigid particle with no internal force calculation. Light grey particles: particles in contact with rigid particle. c) Shear cell design. Dark grey particles: example of double particle due to periodic boundaries. Medium grey particles: upper and lower wall boundaries, light grey particles: material particles. d) Curve A and B: Calibration of shear velocity. Calibration was done with 'silt' experiment using fully spherical particles (e=1.0). Macroscopic friction $\mu^{(M)}$ was used as the calibration parameter. Curve A: Shear velocity 30m/s without density scaling. Curve B: Shear velocity 1µm/s using density scaling. Differences between curve A and curve B are small. Peak friction of curve B is slightly lower than in curve A and slips (drops in friction) occur at different strain increments. However, in general Curves A and B show only minor differences in overall shape.

Curve C: Shear velocity 30m/s without density scaling. Results for friction $\mu^{(M)}$ are calculated using the method Morgan (1999) described and are similar to those in Morgan (1999).

To investigate influences of particle shape or sediment type simulations with 6 different shaped particles were run. Our shear tests enclosed size distributions ranging from pure medium 'silt' to different 'clay' types. 'Silt sediments' were represented by fully spherical particles with a log-normal distribution ranging from 5.6µm to 20µm and a peak value at 10µm (shape S1, Fig. 1c). The variety of clay minerals in natural systems and their calculated sphericity spectra (Table 1) were represented by five different rigid agglomerations built up by 3 to 11 single ideal spherical particles of diverse diameter (shapes C1 to C5, Fig. 1c). The short axis always had diameters ranging from 2µm (C1-C4) to 2.65µm (C5), the long axis of 6µm to 12µm. These particle shapes differed in sphericity ranging from 0.16 to 0.5 (C1 to C3, C5) and in roughness ranging from smooth to strongly rough (C3 to C5). All 'silt' and 'clay' particles were able to move translationally and rotationally in the x- and y-direction.

Table 2: Properties and configuration of numerical models.

Shear box properties	shear box 'silt'	shear box 'clay'
Width [µm]	800	200
Height [µm]	560 (initial)	140 (initial)
Normal stress σ_N [Pa]	$5x10^6$	$5x10^6$
Shear velocity [m/s]	30	30
Ball number	Approx. 6000	Approx. 6000
Particle properties		
Normal stiffness k_N [N/m]	$1x10^9$	$1x10^9$
Shear stiffness k_S [N/m]	$1x10^9$	$1x10^9$
Density ρ [kg/m³]	2600	2600
Radii [µm]	5.6 - 20	short axis: 2 - 2.65 long axis: 6 - 12
Particle friction $\mu_{(P)}$	0.2	0.1

In accordance to the DEM theory we defined microscopic material properties for each particle: coefficient of friction was chosen from literature as $\mu_{(P)}$=0.1 for the 'clay' particles (e.g. Saffer et al., 2001). Since we studied influences of particle shape, coefficient of friction for 'silt' particles was defined as $\mu_{(P)}$=0.2, opposite to natural systems where µ~0.6 (e.g. Kopf and Brown, 2003). However, numerical experiments in Huhn et al. (2006) showed no significant differences in deformational behaviour and frictional strength between particle friction of $\mu_{(P)}$=0.2 and $\mu_{(P)}$=0.6 in case of pure 'silt'. In addition, particle stiffnesses $k_{(P),N}$, $k_{(P),S}$=$1x10^9$ N/m were held constant for both types of material (Table 2). Since modelling was done on the grain scale level, particle density was not chosen from bulk rock density of silt or

clay, but according to mineral densities for quartz and clays such as kaolinite, illite and montmorillonite as $\rho_{(P)}$=2600 kg/m³ (e.g. from Lambe and Whitman, 1969).

After generating the specimen, the servo algorithm was used to compact the particle assemblages. After compaction a constant shear rate was applied to the upper boundary wall (Fig. 2c). The desired shear rate had to be determined by careful testing for reasons outlined below. As can be seen from Eq. 7 in Appendix B, the timestep *dt* depends to a great extent on particle mass. Due to particle size, particle mass is very small which leads to a very small timestep of ~ $4*10^{-12}$s. Since we wanted to model strain up to 200% to make sure constant residual friction is reached, this would correspond to several weeks of real time for a single simulation. To achieve results in a reasonable amount of time, it is possible to scale the particle densities up and achieve a greater timestep. This only affects inertial masses and has successfully been used in recent works (e.g. Morgan and Boettcher, 1999). However, in our code mass scaling was limited to single particles and therefore could not be used for 'clay' shaped particles. For this reason we increased the applied shear rate for the upper boundary wall. Careful testing yielded that in our simulations a shear rate of 30m/s resembles a shear rate of 1µm/s (Fig. 2d) which is widely used in analogue and numerical shear tests (e.g Morgan, 1999; Morgan and Boettcher, 1999; Saffer and Marone, 2003).

3.1.2 Measurement and techniques

Similarly to analogue and numerical experiments (Ask and Kopf, 2004; Guo and Morgan, 2004; Huhn et al., 2006; Kopf and Brown, 2003; Marone, 1998; Morgan, 1999; Morgan and Boettcher, 1999; Saffer et al., 2001; Saffer and Marone, 2003) we utilized several parameters for analysis of our experimental runs.

(1) To visually determine shearing progress, layers were coloured so layer distortion and disturbance could be determined visually. (2) Localization of slip planes and shear zones was calculated through the monitoring of relative displacement of all particles during the shear process. (3) Developments in 'clay' microfabric were measured by particle rotation patterns and by monitoring the evolution of particle domains. (4) Additionally, volume strain and porosity change were calculated at each 0.1 strain increment. (5) Shear strength of the particle assemblage was measured continuously and is expressed by assemblage peak and average friction. A detailed description of the measurement processes involved is provided in Appendix C.

4 Results

Although the DEM supplies numerous information at each time step or strain increment we selected specific model steps for our interpretations which exemplified typical features or trends.

4.1 Layer distortion and shear zone development

The initial particle configuration after compressing the specimen showed few differences between the experiments (Fig. 3a). Differences were obvious in box height and layer appearance. Height differences were small, ranging on the order of a few micrometers. For the smooth particles initial height decreased with increasing sphericity. Measured heights were: 116µm for experiment C1 (sphericity e=0.16), 113µm for experiment C2 (e=0.22) and 112µm for experiment C3 (e=033). On the other hand, increasing roughness led to greater box heights. For the slightly rougher particles in C4 (e=0.33) observed height was 115µm and for the roughest particles in model C5 (e=0.5) 154µm.

The differences in layer geometry depended on differences of particle package. This led to the somewhat crinkled appearance of layers primarily in model C1 and C2, which exhibited the lowest sphericity. This effect decreased with increasing sphericity while particle roughness had no effect.

After 200% strain localised deformation or shearing had occurred in all model runs (Fig. 3b). A direct relationship between degree of distortion and particle shape could be observed. In experiment C1 the entire material package showed strong disturbances, especially in the upper four layers. With increasing sphericity distortion decreased (model C2). The upper four layers of experiment C2 were nearly undisturbed despite a small disruption of layer 2. In this case distortion mainly occurred in layers 5-11. A further increase in sphericity resulted in even less distortion (C3). Only the upper 4 layers showed substantial disturbances while the lower packages remained nearly unchanged. On the opposite disturbance was limited to the 3 lowest layers for fully spherical particles in the 'silt' experiment (S1) whereas the upper parts were not affected.

Similarly, variation of particle roughness also had an effect on layer distortion (Fig. 3b). Compared to the other experiments, increasing the particle roughness in model C4 resulted in only slight distortion of all layers. Here, the degree of layer thickening and thinning decreases from top to bottom. Furthermore increasing the roughness in experiment C5 resulted in almost undisturbed lower layers (9 to 11) while the upper layers displayed strong thickening and thinning features. This relationship between particle shape and deformational behaviour,

particularly strain localisation, could also be monitored from horizontal displacement fields (Fig 4a). In case of low particle sphericity (e=0.16, model C1) high relative displacements confirmed the existence of thin slip planes. These slip planes interconnect creating shear zones which laterally extending over the entire shear box. This led to two distinct and coherent shear zones localized close to the upper wall and in the intermediate part of the shear box. Both shear zones exhibit low vertical dilation (Fig. 4a, C1). Slip plane angles are presented in a rose diagram (Fig. 4b) and were mainly oriented sub-horizontally varying between 20° and -25° (Fig. 4b, C1).

Fig. 3 (next page) a) Initial configuration for each particle shape. b) Final configuration after 200% strain for each particle shape. Coloured layering is for visualisation only and does not represent particle properties.

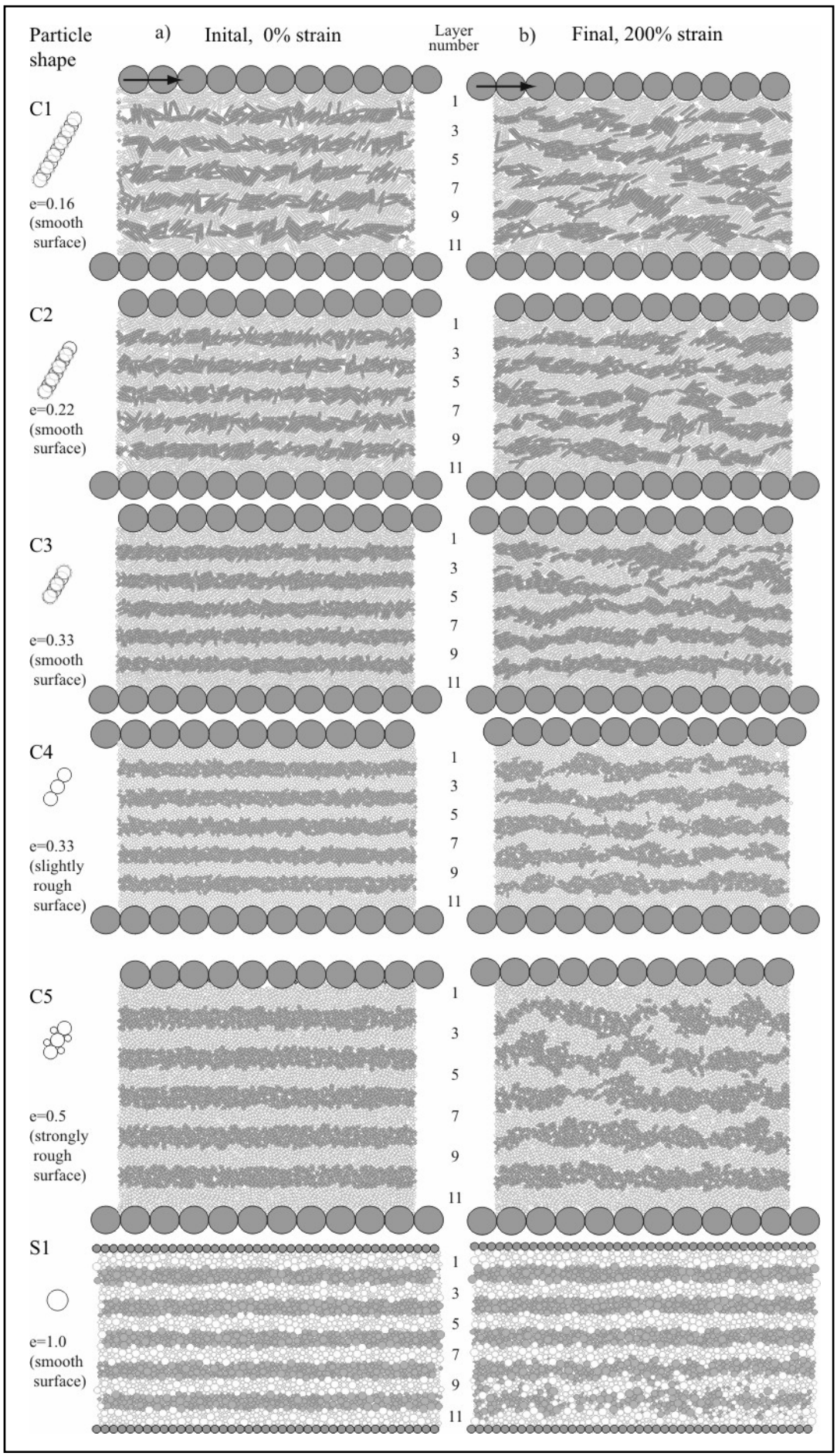
Particle shape
a) Inital, 0% strain
Layer number
b) Final, 200% strain
C1
e=0.16 (smooth surface)
C2
e=0.22 (smooth surface)
C3
e=0.33 (smooth surface)
C4
e=0.33 (slightly rough surface)
C5
e=0.5 (strongly rough surface)
S1
e=1.0 (smooth surface)
1
3
5
7
9
11

With increasing sphericity (e=0.22, model C2) a trend to stronger strain localisation along a single but more distinguished coherent shear zone with higher vertical dilatation was observed (Fig. 4a, C2). This shear zone was located in the intermediate part of the shear box. Coevally, most slip plane angles were oriented horizontally with only very minor peaks at 20° and -30° (Fig. 4b, C2). A further increase of sphericity (e=0.33) in experiment C3 led to an even more distinguished, vertically dilated, and coherent shear zone compared to model runs C1 and C2 (Fig. 4a). This shear zone included almost all existing slip planes in the shear box and is located in the upper half of the shear box. Overall, slip plane length and slip plane frequency in this experiment had decreased. Slip plane angles of ~18° and ~-28° are almost as frequent as slip planes of 0° (Fig. 4b, C3).

In the case of fully spherical particles, slip planes only developed in the lower part of the material, creating a coherent shear zone which was broader compared to previous model runs (Fig. 4a, S1). Orientation of slip planes had a slight peak at the horizontal direction. However, 40°, 20°, -15°, -25°, and -50° were almost as frequent as 0°.

Increasing the roughness resulted in a decrease of shear plane length and an increase of slip plane activation and frequency (e=0.33, C4; Fig. 4a). Slip planes were largely oriented sub-horizontally, with few interconnections and concentrated in the upper and intermediate part of the material. Therefore, significantly less coherent shear zones were located in these parts of the material. Additional increase in roughness led to an increase in slip plane number. These slip planes were primarily located in the material's intermediate and upper part. Interconnection of slip planes decreased resulting in a completely distributed shear zone (Fig. 4a, C5).

Fig. 4 (next page) Development of slip planes and shear zones: a) Normalized relative displacement fields after 200% strain. High relative displacement (red) indicates existing slip planes, interconnecting slip planes indicate shear zone. Blue arrows show shear zone localisation and are absent in model C4 and C5 due to distributed slip localization. Note that the plot S1 is downscaled by a factor of 4 b) Frequency rose diagrams of slip plane orientation. Slip plane angles are relative to horizontal orientation. Number of slip planes: C1: n=156, C2: n=159, C3: n=139, C4: n=222, C5: n=265, S1: n=41.

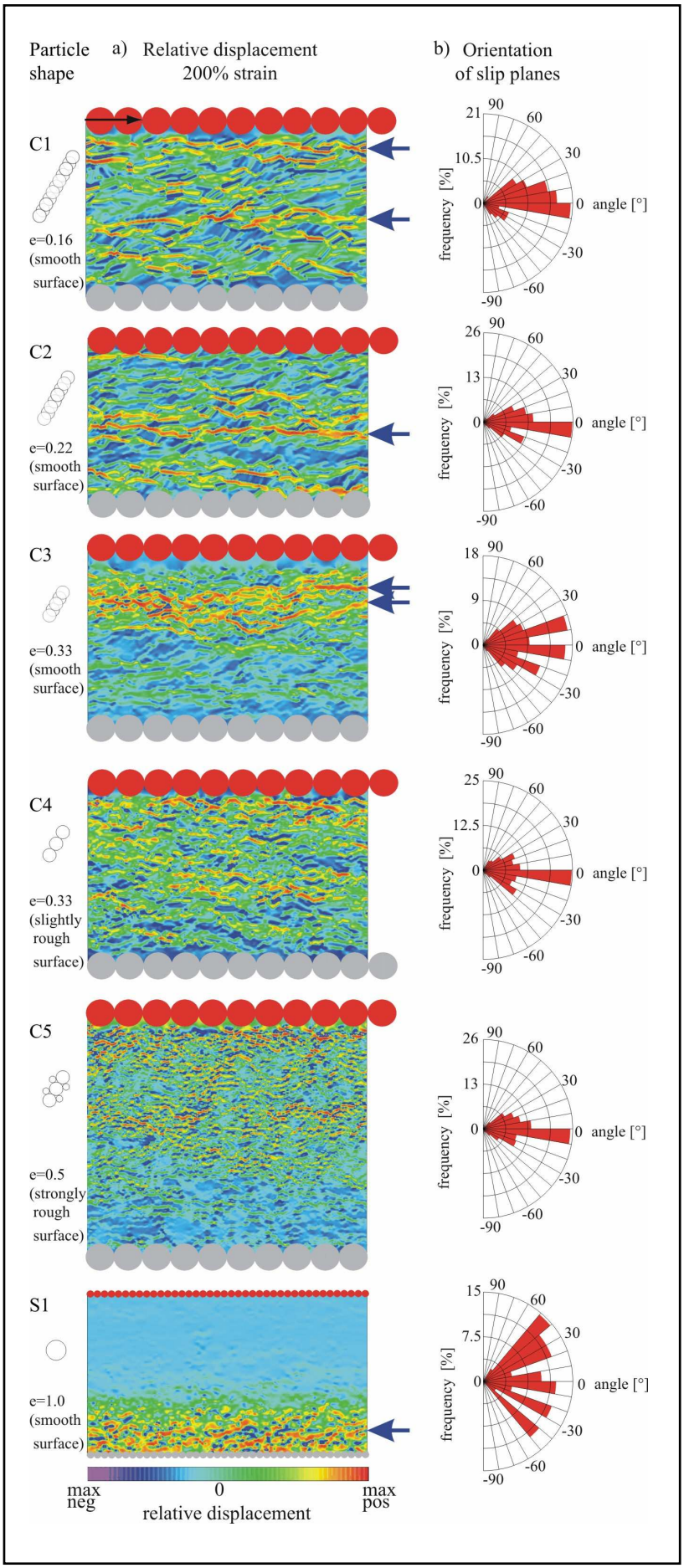
Particle shape
a) Relative displacement 200% strain
b) Orientation of slip planes
C1
e=0.16 (smooth surface)
C2
e=0.22 (smooth surface)
C3
e=0.33 (smooth surface)
C4
e=0.33 (slightly rough surface)
C5
e=0.5 (strongly rough surface)
S1
e=1.0 (smooth surface)
max neg
0
max pos
relative displacement
frequency [%]
angle [°]
90
60
30
0
-30
-60
-90
21
10.5
26
13
18
9
25
12.5
15
7.5

4.2 Particle domain evolution and rotation

The initial procedure of generating all specimens produced randomly oriented particles. The effect of particle shape on the deformational behaviour was shown by analysis of single particle rotation, which enabled particles to take up preferred positions during shear and to form domains of similar orientation. This analysis was performed only upon 'clay'- shaped particles.

At the final stage of strain (200% strain) particle orientation for experiment C1 (e=0.16) showed a strong bias towards sub-horizontal and horizontal angles (0° and 180°, Fig. 5). Additionally, particle orientation mainly plotted between 10° and 40° with a pronounced peak at the 10°-15° bin. Overall, only a few individual particles were oriented with their long axis steeper than that and altogether less than 2.5% were oriented between 60-120°. Increasing sphericity (experiment C2, e=0.22) resulted in a tendency of the particles' long axis to rotate to slightly higher angles with the peak laying at 30°. Compared to the previous model run, fewer particles rotated to angles between 0°-30° and more particles to 30°-60°. In this case more than 2.5% of particles were oriented between 60°-70°. A further increase of sphericity (experiment C3, e=0.33) showed the main peak of particle orientation again at 10°-15° (Fig. 5). An increasing number of particles compared to previous experiments now exhibited orientation angles above 60° whereas sub-horizontal and horizontal orientation were not as frequent as before.

Compared to experiment C3 (e=0.33) increasing roughness in experiment C4 (e=0.33) resulted in a tendency to a more distributed orientation angle frequency, including angles steeper than 60°. Although most angles still were (sub)horizontally oriented (0°, 180°) and although there is a pronounced peak at the 20-30° bin, there were now more angles oriented between 60°-120° than in experiment C3. Furthermore increasing roughness (C5, e=0.5) increased this tendency towards a more distributed frequency and towards steeper angles with the peak frequency still laying at 20°-30°.

Compressing the specimen until stable normal pressure of 5MPa was reached led to building of particle microfabric even before shearing was started (Fig. 6).

Experiment C1 (e=0.16) showed numerous particle domains with book-sheet structures and embedded single particles. Here, domains mostly consisted of 5-7 single particles (Fig. 6a), whereas also larger and smaller domains did occur. Increasing sphericity for the smooth particles to e=0.22 and e=0.33 in experiments C2 and C3, respectively, showed no relevant changes in domain organisation.

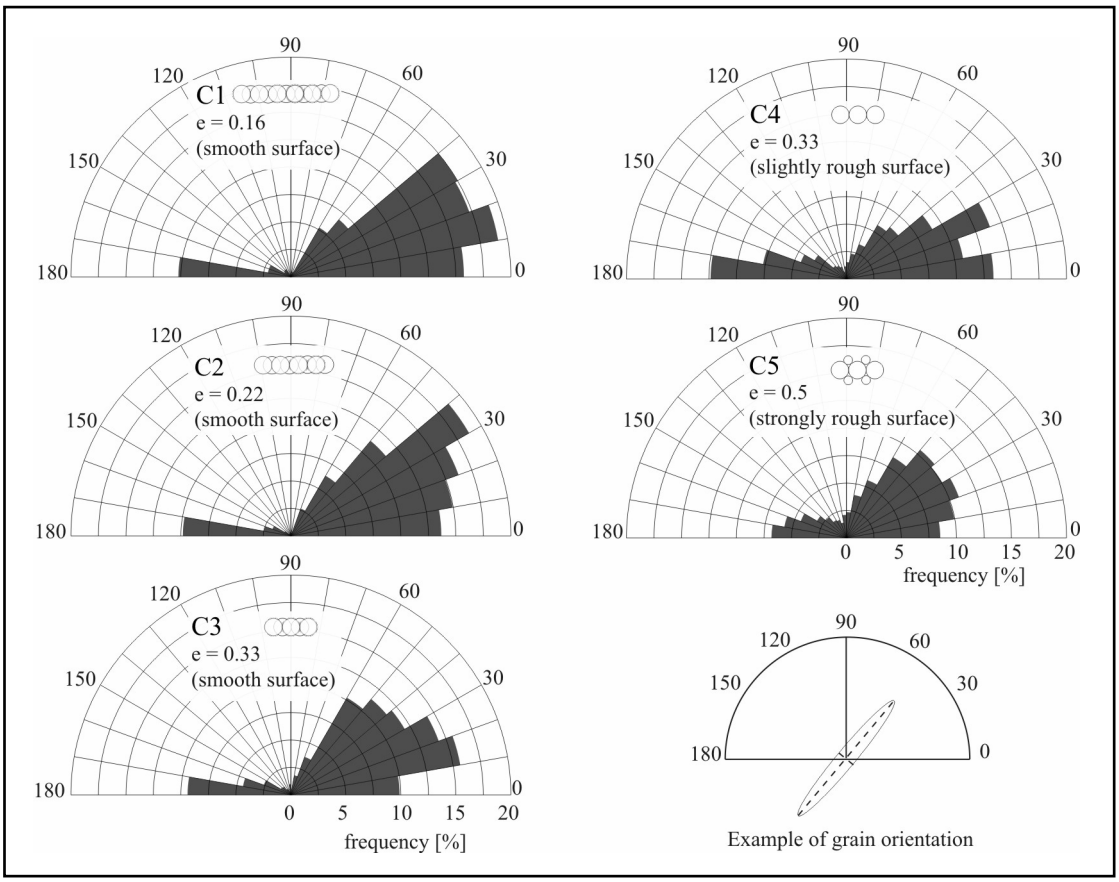

Fig. 5 Particle orientation at 200% strain. Bottom: Example of how orientation was determined.

Increasing the roughness in experiment C4 (e=0.33) had also little effect on the initial domain configuration. The number of particles per single domain had increased producing large stacks of particles. In contrast, a further increase in roughness resulted in lower particle numbers per domain in experiment C5 (e=0.5).

During shear domain configuration changed significantly in most model runs. In case of experiment C1 (e=0.16), domain dimensions increased strongly (Fig. 6b, C1). Occasionally extremely large structures evolved consisting of several domains with nearly the same orientation. The different sphericities of e=0.22 and 0.33 in experiments C2 and C3 showed no influence on the spatial and temporal domain evolution. Both models mirrored increasing domain dimensions and the building of large structures comparable to model C1.

Opposite, increasing roughness caused no change in spatial domain distribution in model C4 and C5 (Fig. 6b) during shear. In both simulations, number and dimension of domains were constant during the whole experiments.

Fig. 6 (next page) Particle domain evolution. Particle shapes are displayed as idealised ellipses. a) Initial stage: 0% strain. Blue arrows indicate average sized domains, green arrows large sized domains. b) Final stage: 200% strain. Black arrows indicate large structures consisting of several domains.

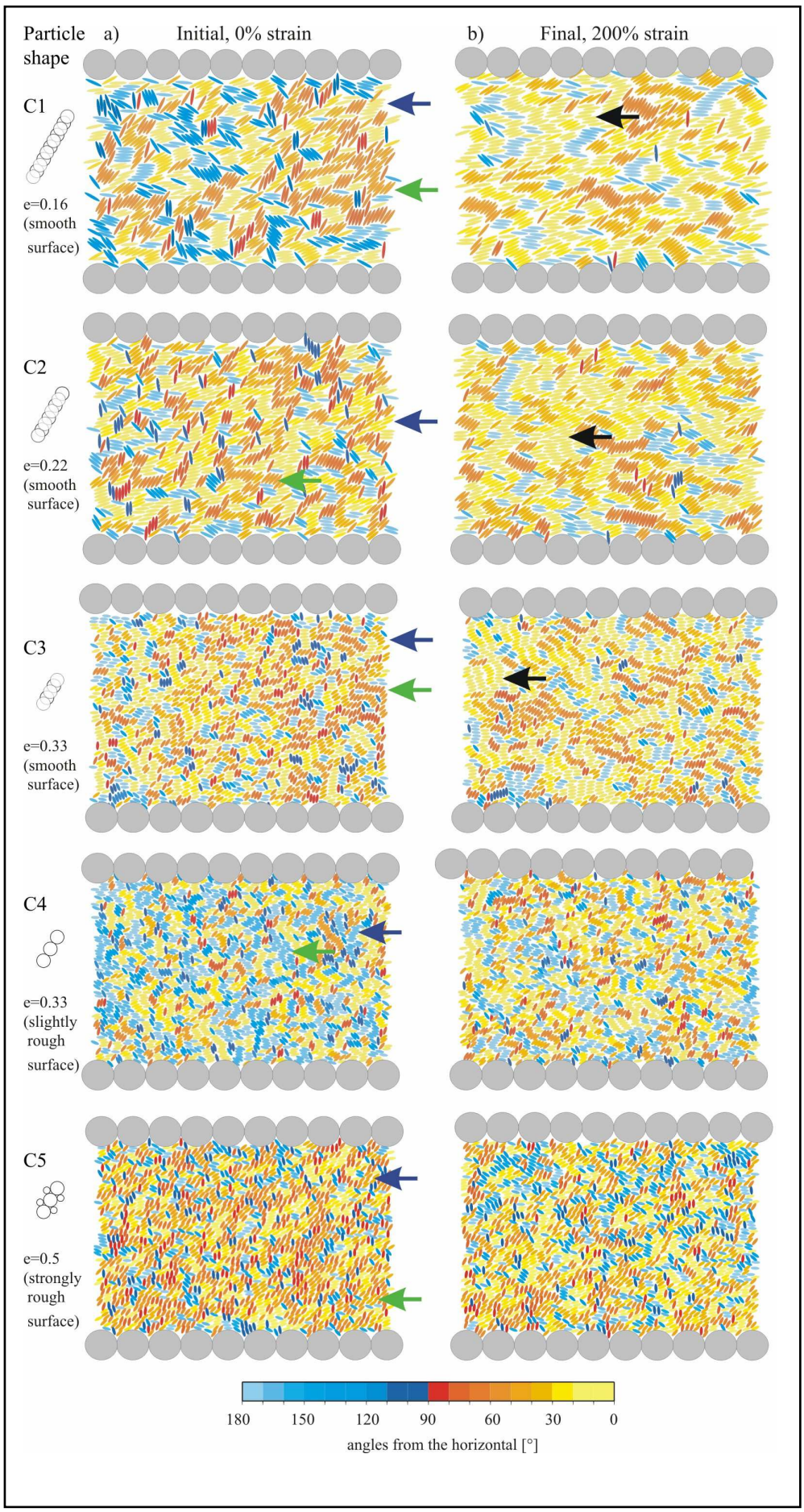
Particle shape
a) Initial, 0% strain
b) Final, 200% strain
C1
e=0.16 (smooth surface)
C2
e=0.22 (smooth surface)
C3
e=0.33 (smooth surface)
C4
e=0.33 (slightly rough surface)
C5
e=0.5 (strongly rough surface)
180 150 120 90 60 30 0
angles from the horizontal [°]

4.3 Frictional strength, volume strain and porosity change

In all experiments macroscopic friction ($\mu^{(M)}$) was calculated continuously during the entire model run. Therefore, detailed information about temporal evolution of $\mu^{(M)}$ as a function of strain was available for all experiments (Fig. 7a). After initiation of shear stress, friction increased in all tests. However, constant residual friction was always reached at least after 150% strain, so that the presented values for residual friction are the calculated average from 150% strain to 200% strain. Peak values of friction correspond to the maximum value of $\mu^{(M)}$ reached during the whole experiment.

Increasing the sphericity resulted in increasing friction. Experiments C1 to C3 showed residual values of μ =0.147, μ =0.150 and μ =0.186, respectively (Fig. 7a). Additionally, curve shapes of these experiments were comparable. These curves showed rapid increase during < 1% strain after which stable friction with low variation was reached. Friction increased when sphericity was set to 0.5 (C5). In this case the shape of the curve also changed, so that a peak value of $\mu^{(M)}$=0.33 at 15% strain was attained after which a gradual decrease to a residual $\mu^{(M)}$=0.23 occurred showing moderate variability.

Fully spherical particles (e=1.0) in experiment S1 exhibited extremely high peak friction of $\mu^{(M)}$=0.72 before it dropped to the residual value of $\mu^{(M)}$=0.498 showing strong variability.

Increasing the roughness caused friction to rise to high peak values of $\mu^{(M)}$=0.6 (C4). Subsequently, $\mu^{(M)}$ stayed at this level varying strongly about ~0.53. These particles with highest roughness (C5) showed frictional behaviour described in the previous paragraph.

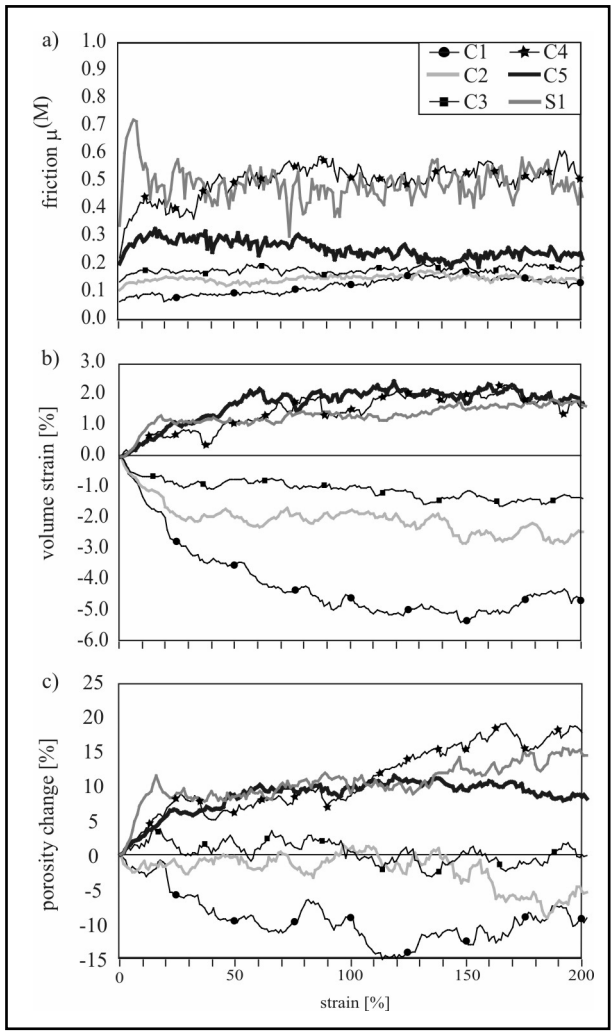

Fig. 7 a) Friction $\mu^{(M)}$ for all model runs. b) Volume strain δV for all model runs. c) Porosity change δv for all model runs.

The volumetric strain (Fig. 7b) showed comparable development for experiments C1 to C3 (e=0.16; e=0.22; e=0.33). The volume decreased rapidly immediately after shearing and continued to decrease gradually. At the end of the experiment the volume strain decreased by -5%, -2.5% and -1.5% for models C1, C2, and C3, respectively. So in general smooth particles exhibited decreasing negative volume strain with increasing sphericity. Furthermore increasing sphericity in experiments C5 (e=0.5) and S1 (e=1.0) led to a positive volume strain of approx. +2%, indicating a material volume increase (Fig. 7b).
In contrast to experiments C1 to C3 increasing roughness in models C4 and C5 (e=0.33; e=0.5) resulted in positive volumetric strain. Both of these experiments showed a rapid increase of volume strain after which values varied about +2%.

There was a strong correlation between volume strain and porosity change. Thus, results for porosity and porosity change showed the same tendencies as the volume strain (Table 3; Fig 7c). Initial porosity in case of the smooth particles went down about -10% and -5% for experiments C1 (e=0.16) and C2 (e=0.22) while it varied about zero for experiment C3 (e=0.33). For the 'silt' experiment S1 (e=1.0) porosity increased rapidly when shearing started to reach the peak value of 15% at 200% strain.
Increasing roughness in experiment C4 (e=0.33) led to the highest increase in porosity of 18% while a further increase of roughness (C5, e=0.5) resulted in lower porosity increase of ~9%.

5 Discussion

Our results show that particle rotation, domain evolution, shear zone development, frictional strength, volume strain, and porosity change are a function of particle sphericity and roughness. Sphericity and roughness exhibit a unique impact on the evolution of 'clay' microstructure and shear zone localization.

5.1 Interaction of microstructure and friction

Friction is highest for the pure 'silt' model S1 and lowest for the most elongate particle C1 (e=0.16; Table 3). Since typically rolling friction is assumed to be lower than sliding friction, the question arises why ideal spherical 'silt' particles exhibit higher friction values than tabular 'clay' particles although 'silt' could rotate unobstructed by their particle shape.
With decreasing sphericity the particles built up a complex initial microstructure showing domains with book-house structures similar to natural clay materials (Fig. 1b). When shear stress was induced, this microstructure broke down. Volume and porosity decreased, particles rotated to more preferred orientations, material assemblage contracted and shear strength was

reduced. In our experiments, this effect decreased with increasing sphericity. Due to the lower initial volume and porosity, the breakdown of microfabric in experiments C2 and C3 could not be as strong as for particles with lowest sphericity (C1). As a consequence assemblage contraction was lower resulting in increasing shear strength. Accordingly, highest shear strength was measured with the fully spherical particles in model S1 (e=1.0). In this case, rotation of fully spherical particles did not cause a strength reduction and microstructure breakdown was impossible. Consequently, dilation occurred, leading to an increase in shear strength (Morgan, 1999).

Table 3: Summary of selected results.

Experiment [sphericity]	Initial height after compression [µm]	Final height after shear [µm]	Average friction $\mu^{(M)}$ (150% - 200% strain)	Peak friction $\mu^{(M)}$	Initial porosity [%]	Final porosity [%]
C1 [0.16]	116	111	0.147	0.182	19.0	17.2
C2 [0.22]	113	110	0.150	0.176	15.9	15.0
C3 [0.33]	112	111	0.186	0.212	12.5	12.5
C4 [0.33]	115	117	0.53	0.6	17.5	20.6
C5 [0.5]	158	161	0.23	0.33	21.0	22.8
S1 [1.0]	437	444	0.498	0.72	11.0	12.6

The effect of roughness on microstructure can be best observed by comparing particle shapes C3 and C4 with identical sphericity (e=0.33) and different roughness. Volume strain was negative for smooth particles and very high for rough particles. This occurred because a rougher particle shape enhanced the capability of interlocking particles (Fig. 8a). This effect was also observed by Guo and Morgan (2004) for angular shaped particles. Accordingly, shearing induced different effects on the rough particles' microstructure compared to the smooth particles' microstructure (C1-C3): For model C4 rotation and slip occurred while volume increased which resulted in an increase of shear strength (Marone et al., 1990). Unexpectedly, a further increase in roughness (C5; e=0.5) led to lower shear strength compared to experiment C4 (e=0.33). We suppose this is caused by different interlocking capabilities of particle types C4 and C5. Both particle types are able to interlock perfectly if their long axes are oriented parallel to each other, leaving no room for shear to occur except to move perpendicular to that parallel orientation (Fig. 8 a,b). If particles are not oriented parallel to each other only particle shape C1 still has the possibility to interlock perfectly (Fig. 8c). In contrast, particle type C5 can not interlock perfectly in this case leaving a void

between particles (Fig. 8d), which explains the higher initial porosity and box height in this experiment.

This also explains the peak and subsequent decreasing values of $\mu^{(M)}$ for C5. During the first stages of shear, slip and rotation were obstructed by interlocking particles and low volume, which led to high friction. When volume increased, slip and rotation could happen more easily and particle reorganisation progressed resulting in a decrease of friction at a later stage in this experiment.

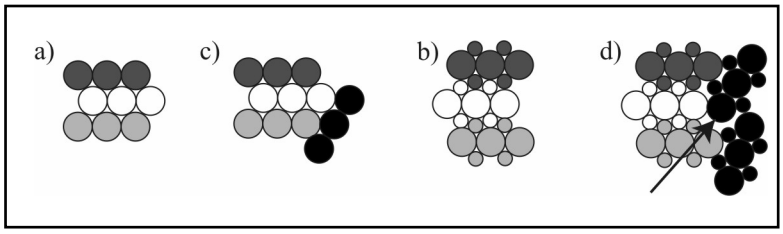

Fig. 8 Particle interlocking mechanism a) Perfect interlocking of parallel particles of shape C4 b) Perfect interlocking of parallel particles of shape C5 c) Perfect interlocking of non-parallel particles of shape C4 d) Imperfect interlocking of non-parallel particles of shape C5. Arrow indicates void space.

5.2 Shear zone localisation

Our results indicate that there is a direct relationship between domain evolution (Fig. 6b), shear zone localization (Fig. 4a), and particle roughness. We suppose that the absence of coherent shear zones is a result of the lack of large sub-horizontal domains in case of rough particles.

Evolution of large domains with preferred particle orientation only occurred in the case of smooth particles (C1-C3) and was precluded in both cases of rough particles (C4 and C5). Similarly, coherent shear zones only developed in the case of smooth particles and although more slip planes existed in experiments with rougher particles where no coherent shear zones developed.

The ‘silt’ model is a special case since its ideal spherical particles could not built domains. The localization in this case may be due to the particle size distribution of the ‘silt’. Morgan and Boettcher (1999) showed that strain localization to a large extent depends on particle size distribution. Although they used higher normal loads (70MPa) these results may applicable to our models.

Localisation of slip planes to a single shear zone with stronger vertical dilation was enhanced with increasing sphericity. In these cases, single shear zones showed a tendency to form at lower positions inside the shear box, especially for the pure ‘silt’ model. However, domain evolution cannot be the dominant controlling parameter for localization, since the trend to

single shear zones is observed in experiments C1-C3 (smooth particles) where domain evolution was similar and for the 'Silt' experiment as well, where domain evolution was impossible. We suppose that in these cases single particle rotation is the major factor for localisation of shear zones because higher sphericity particles could more easily rotate locally to preferred orientations when shear stress was acting on them. For the bulk material, this resulted in above mentioned increase of friction and lower decrease of volumetric strain.

5.3 Natural equivalents

Comparing our modelling results with analogue experiments for natural clays and silts reveals differences and similarities:

The modelled volume strain for smooth 'clay' shaped particles (C1-C3) is similar to analogue experiments conducted with normally consolidated and lightly overconsolidated clays (Lambe and Whitman, 1969; Mitchell and Soga, 2005). Volume strain for smooth 'silt' particles is comparable with natural dense soils (Lambe and Whitman, 1969; Mitchell and Soga, 2005). Results for the rough particles (C4, C5) are similar to heavily overconsolidated clays (Lambe and Whitman, 1969; Mitchell and Soga, 2005).

Our shear experiments with shape C3 showed a shear zone located in the medium part of the material as well as slip planes oriented at ~18° and ~-28°, which is similar to a shear zone and Riedel shears in a clay sediment sheared in an analogue shear box (Huhn et al., 2006).

Almost all particle shapes showed comparable friction $\mu^{(M)}$ as in nature. Saffer et al. (2001) calculated μ~0.30 for sliding friction of dry smectite powders at 5MPa normal stress, whereas $\mu^{(M)}$=0.25 at 200% strain was a bit lower (Table 3) in our simulation. Furthermore, values of $\mu^{(M)}$ for particle shapes C1-C3 (Table 3) exhibit the frictional strength of smectite powder sheared in Kopf and Brown (2003) at 5MPa and in Ask and Kopf (2004) with normal stresses <1MPa. However, these experiments were conducted under wet conditions and effective stresses were reduced so comparisons may not be strictly applicable to our modelled 'dry' conditions. Comparable results for the 'silt' particles were reached by quartz mineral standards in Kopf and Brown (2003) under saturated conditions. Since the results for shear strength and friction of analogue and numerical shear experiments are similar we suppose that the deformational mechanisms and behaviour of the numerical particle shapes exhibited may be transferred - with restrictions - to natural clay.

These restrictions are grain fracture and pore fluid interaction. Grain fracture is a process that may start even at low pressures and is highly dependant of particle size (Mitchell and Soga, 2005). It is yet unclear to which extent grain fracture plays a role concerning clay

deformation, but the breakage of aggregates of clay, e.g. clay domains observed in Fig. 6, may be similar to grain breakage and relevant to clay deformation behaviour (Mitchell and Soga, 2005).

The role of pore fluids during deformation is significant. In saturated specimen, effective stress is reduced due to pore fluid pressure. Different electrolytic concentrations of water (e.g. freshwater vs. seawater) result in different electro and electrochemical interactions between water and clay molecules. These processes have a high impact on cohesion, swelling behaviour, etc. of clay minerals.

Chen and Anandarajah (1996) and Anandarajah (1999) examined methods to implement repulsive and van-der-Waals forces into Discrete Element simulations. Anandarajah and Lavoie (2002) conducted DEM consolidation experiments using those methods. They concluded that the van-der-Waals forces hold unstable clay microstructures together until a threshold stress level is reached. Transferring these results to our shear experiments may lead to somewhat higher peak and average shear strength.

6 Conclusions

Our numerical experiments attest that the deformation behaviour of clay is mainly controlled by their particle shape which directly influences the specimens' ability to dilate or contract. Different particle sphericity and roughness lead to fundamentally different deformation mechanisms. Decreasing sphericity caused complex initial microfabrics whose breakdown with increasing strain is caused by particle rotation to preferred angles. These preferred angles favour low friction since slip occurs more easily. Increasing roughness results in particle interlocking of different degrees which obstructs slip and rotation to preferred orientations so that friction is high and volume strain positive.

The existence of shear zones depends on the roughness of particles. Increasing roughness of particles precludes shear zone development, because particle domains of similar orientation cannot evolve due to interlocking.

The localisation of shear zones depends on particle sphericity. Increasing sphericity leads to more localised but vertically dilated deformation since higher sphericity results in particle rotation to preferred angles.

Some of our experiments show remarkable resemblance to analogue experiments conducted with dry and saturated clay powders. Especially the roughest particle showed similar results in the stress-strain response which are similar to dry tests conducted on smectite powder (e.g.

Saffer et al., 2001). Smooth tabular particles of low sphericity showed similarities to tests conducted under completely dry conditions.

7 Outlook

Based on these results we will implement fluids in our shear box experiments to test the effect of pore pressure and electrostatic forces on the deformational behaviour of clay rich and silty sediments. The expansion into 3D is favourable to test the influence of sheet-like particle geometries on deformation.

Acknowledgements

Funding for this research has been received through Deutsche Forschungsgemeinschaft via the Research Center Ocean Margins (RCOM). This is RCOM publication #0410.

We thank Julia K. Morgan, Maria V.S. Ask, and David Saiang for very constructive reviews. We also thank our college Achim Kopf from the Research Center Ocean Margins for fruitful discussions on analogue shear tests, sediment physics, and material behaviour.

Appendix A – List of symbols

e	sphericity, dimensionless
$F_{(P),N,S}$	interparticle force; normal and shear [N]
$k_{(P),N,S}$	particle stiffness; normal and shear [N/m]
$\Delta D_{N,S}$	particle overlap, normal and shear [m]
$F_{(P),Net}$	total net force acting on one particle [N]
$M_{(P),Net}$	total net moment acting on one particle [Nm]
$m_{(P)}$	particle mass [kg]
$I_{(p)}$	particle moment of inertia [kgm²]
$\ddot{x}$	translational acceleration [m/s²]
$\dot{\omega}$	rotational acceleration [rad/s²]
dt	timestep [s]
$\mu_{(P)}$	particle coefficient of friction, dimensionless
$\rho_{(P)}$	particle density [kg/m³]
n	particle number
F_{smax}	maximum shear force [N]
τ_{crit}	critical shear stress [Pa]
σ_N	normal stress in Mohr-Coulomb equation [Pa]

μ_C	coefficient of friction in Mohr-Coulomb equation, dimensionless
C	cohesion in Mohr-Coulomb equation [Pa]
$\sigma_N^{(M)}$	macroscopic normal stress acting on particle assemblage [Pa]
$\tau^{(M)}$	macroscopic shear stress acting on particle assemblage [Pa]
$\mu^{(M)}$	macroscopic friction of particle assemblage, dimensionless
$\overline{\sigma}_{ij}^{(M)}$	average stress tensor of defined volume in particle assembly; i,j = 1,2
$\sigma_{(p),ij}$	stress tensor for a single particle; i,j = 1,2
$V_{(P)}$	particle volume [m³]
δV	normalized volume strain, dimensionless
V	instantaneous volume of particle assembly [m³]
V_0	initial volume of particle assembly [m³]
$\delta\nu$	normalized porosity change, dimensionless
ν	instantaneous 2 dimensional porosity of defined volume in particle assembly
ν_0	initial 2 dimensional porosity of defined volume in particle assembly

Appendix B – DEM theory

Particles interact at common contact points caused by given boundary conditions, e.g. loads or shearing forces (Fig. 2a). If particles interact elastic deformation occurs. This results in a repulsive contact force F_N acting normal to the contact plane as well as a shear force F_S parallel to that plane. These contact forces can be calculated using the particle overlap $\Delta D_{N,S}$ which scales with the elastic deformation (Cundall and Strack, 1978; Itasca, 2004):

(1) $F_{(P),N} = k_{(P),N} * \Delta D_N$ (2) $F_{(P),S} = k_{(P),S} * \Delta D_S$.

$k_{(P),N}$ and $k_{(P),S}$ are inherent particle stiffnesses (normal and shear, see Table 2) which, together with particle friction $\mu_{(P)}$ and density, govern the deformational behaviour at inter-particle contacts. In case of spherical particles (3D), the overlap can be calculated by the non-linear Hertz -Mindlin theory (Mindlin and Deresiewics, 1953). We use the 2-dimensional version of the PFC code so that the overlap is calculated using a linear relationship.

For each particle P the total net force $F_{(P),\,Net}$ and the total moment $M_{(P)}$ are computed with

(3) $$F_{(P),Net} = \sum_n (F_{n,N} + F_{n,S})$$

(4) $$M_{(P),Net} = \sum_n (F_{n,S} * r_{(P)})$$

where *n* particles are interacting with particle P and $r_{(P)}$ is the particle radius (Fig. 2b).
Calculation of contact forces is followed by computation of particle acceleration and rotation using Newton's second law:

(5) $F_{(P),Net} = m_{(P)} * \ddot{x}$ (translational motion)

(6) $M_{(P),Net} = I_{(P)} * \dot{\omega}$ (rotational motion)

where $m_{(p)}$ is the particle mass, $I_{(p)}$ the moment of inertia, and $\ddot{x}$ and $\dot{\omega}$ the translational and rotational acceleration acting on the particle. To achieve a steady-state particle assembly and to prohibit particles from oscillating (Morgan and Boettcher, 1999) a damping force must be introduced into the system. We use a form of damping which acts upon the force applied to each particle (Cundall, 1987; Itasca, 2004).
To calculate particle displacement vectors these equations need to be integrated. This is done with a model inherent scheme, where the time-step dt for integration is calculated. The time-step is calculated as the minimum value of *dt* with

(7) $dt = \sqrt{m_{(P)} / k_{(P)}}_{N,S}$

for all possible combinations of particle parameters (e.g. Cundall and Strack, 1978, 1979, 1983; Itasca, 2004).
Maximum shear force at the contact point (F_{Smax}) is limited to the critical shear force, given as

(8) $F_{S\max} = \mu_{(p)} F_{(P),N}$

which defines when contact slip will occur. For natural materials failure criterions are empirical and based on phenomenological descriptions of soil behaviour (Mitchell and Soga, 2005). The most widely used criterion for strength is the Mohr-Coulomb criterion for brittle deformation

(9) $\tau_{crit} = \mu_C \sigma_N + C$

where σ_N is normal stress, μ_C is the coefficient of friction and C is cohesion, which for all particles in our models is zero. The critical shear stress (τ_{crit}) is shear stress at the failure plane and is equivalent to F_{Smax} in equation (8). This means that progressive breaking of contacts along discrete planes in our numerical model reproduces fracture and fault propagation in nature (Strayer and Suppe, 2002).

Appendix C – Measurement theory

First of all, applied strain was calculated from the displacement of the upper boundary wall relative to the instantaneous shear box height. Additionally, absolute shear box height was

used to monitor volume strain δV which was calculated by $\delta V = \frac{V - V_0}{V_0}$ where V is the instantaneous and V_0 the initial volume. Also computed was 2D porosity change, i.e. the void ratio $\delta \nu = \frac{\nu - \nu_0}{\nu_0}$.

At the beginning of the experiment the 'sediment' was subdivided into horizontal equidistant coloured layers to monitor localised deformation by observed offsets and distortion of these strata. To quantify deformation rates absolute displacements in x- and y-direction of each ball were measured for each 0.1% strain increment, so that a displacement vector for each particle was available. These data were processed with the GMT software package, gridded, and mapped (Wessel and Smith, 1991). A gradient calculation algorithm was then used to emphasize areas of normalized relative displacement. These displacement field plots enabled us to map slip planes within the material, since high relative displacement indicates localised slip (Morgan and Boettcher, 1999). The number of slip planes was then counted and their respective angle towards horizontal orientation calculated.

Additionally the particle orientation was monitored at each 1 % strain increment. Orientation angles were measured from horizontal (0°) over vertical (90°) to horizontal again (180°). This allowed us to observe the changes in each particle's orientation as well as the development of larger domains of particles of similar orientation.

The macroscopic friction $\mu^{(M)}$ for the material package was then calculated by measuring the assemblage shear stress $\tau^{(M)}$ normalized by constant applied normal stress with $\mu^{(M)} = \frac{\tau^{(M)}}{\sigma_N{}^{(M)}}$,.where $\sigma_N{}^{(M)}$ = 5MPa. The shear stress $\tau^{(M)}$ can be computed in various ways. One possible solution is to calculate the shear stress acting on the boundary walls, which is similar to how shear box stresses of analogous experiments are calculated and which Morgan (1999) used in numerical experiments. However, since we are more interested in the friction inside the specimen, we use the relationship for stress calculation outlined in Itasca (2004) for a defined volume in the material package. This was done by calculating the mean stress $\overline{\sigma}_{ij}{}^{(M)}$ of a defined volume inside the material with

$$(10)\quad \overline{\sigma}_{ij}{}^{(M)} = \left(\frac{1-\nu}{\sum_n V_{(P)}}\right)\sum_n \sigma_{(p),ij} \; * V_{(p)} \quad , \text{i=1,2; j=1,2}$$

where $\sigma_{(p),ij}$ is the stress tensor for a single particle, $V_{(p)}$ the particle volume, n the particle number and ν he porosity within the shear cell. Using this relationship $\tau^{(M)} = \overline{\sigma}_{ij}^{(M)}$ with i=1; j=2.

The differences of $\tau^{(M)}$ when it is computed in both ways are shown in Fig. 2d (curve A and curve C).

Chapter IV

Numerical investigation of localization and micromechanics in a stratified soil specimen

Submitted: Ingo Kock & Katrin Huhn, Journal of Structural Geology

Abstract

For many geological deformation processes the existence of a mechanically weak layer is presumed. For these weak layers, clay sediments or clayey fault gouge seem to be a likely candidate. They are supposed to be a focus of displacement und thus crucial for slip plane and shear zone development. There is an ongoing debate concerning the exact nature of shear localization in these layers. To address this question, we use numerical shear box tests utilizing the Discrete Element Method (DEM). Our focus lies on localization patterns and micromechanical properties of stratified 'silt'-'clay'-'silt' and a 'clay'-'clay'-'clay' specimen. We systematically vary the coefficient of particle friction of each layer to analyze localization and micromechanics of the material.

Our results indicate that overall frictional strength of a material package is a result of different deformation modes which also govern localization phenomena. Especially friction contrasts on the particle scale significantly govern the deformational behaviour of our material. An important role plays the ability of single particles to slide, roll or rotate, which to a large extent is influenced by particle friction. We show that localisation switches from one layer to adjacent ones even if differences of material properties are very small. Furthermore, localization is often concentrated in only one layer leading to a complete decoupling of the other layers und thus building a shear zone where high displacement can be accumulated.

1 Introduction

Shearing processes at the upper brittle crust are always attributed to the existence of mechanically weak layers. These are characterized by a lower shear or frictional strength compared to the surrounding material (Dahlen, 1984; Hampton et al., 1996). The low shear strength of a potential shear zone can be explained by their lithology. Hence, clay sediments exhibit lower shear strength compared to silts (Mitchell and Soga, 2005). In addition, Lupini et al. (1981) have shown that there is a direct relationship between clay size fraction and shear strength of sediments. The reason for the low frictional strength of clays is the mechanical behaviour of tabular clay minerals: More precisely, it is the alignment of platy clay minerals during shear deformation and the breakdown of the microstructure (Mitchell and Soga, 2005). As sediments can be considered as a granular material, grain-grain interactions are mostly responsible for the deformational behaviour of materials (Mitchell and Soga, 2005; Oda and Iwashita, 1999). Grain sliding, rolling, and rotation are microscopic deformation modes which influence micromechanics and microstructural evolution. For example, the distribution of stresses is not homogenous and some grains carry more load than others (e.g. Jaeger et al., 1996).

In nature, weak layers are not homogenous stratigraphic units. Numerous distinct shear planes are formed and reactivated repeatedly creating a shear zone. Hence, deformation takes place in well defined parts of a stratified sediment, even if the whole package belongs to a shear zone (Canals et al., 2004; Labaume et al., 1997; Maltman et al., 1997). However, highly resolved description of shear plane development in terms of space and time is very difficult in nature as well as under laboratory conditions. To date, the evolution of a shear planes in a stratified sediment is relatively unknown. It is still uncertain where most displacements are accumulated: on top, intermediate, or at the base of a shear zone. A detailed description and analysis how shear localizes in a weak layer needs to be done on a microscopic scale.

The general aim of this paper is to shed light on the question where microscopic shear zone localization occurs in stratified sediment. Specifically, how strength contrasts in a layered specimen influence localization phenomena; in particular, do shear planes form in the top, middle, or basal part of a weak sediment package, or directly at layer boundaries? Therefore we study the micro-mechanics of shear zone development on a grain scale level.

We use a numerical shear box experiment utilizing the Discrete Element Method (DEM) to investigate the shear strength and deformation styles of stratified sediments. Two types of layered specimen were simulated: (1) A ’silt’-’clay’-’silt’ assemblage and (2) a ‘clay’-‘clay’-

'clay' package. To gain a deeper understanding of the micromechanical processes, we conducted parameter sensitivity studies on the coefficient of friction. Therefore we varied systematically the particle friction for each 'sediment' within the numerical shear box. We focus on (1) slip plane and shear zone evolution and on (2) friction, percentage of slipping grains (sliding fraction), magnitude of grain rolling and rotation, and on the number of neighbours each grain has (coordination number).

2 Methods

2.1 The Discrete Element Method

The Discrete Element Method is based upon numerical description of granular materials. The applied commercial 2D code PFC2D was developed by Cundall and Strack (1978). Here, spherical particles interact according to simple physical contact laws. Thereby, a particle assemblage of many particles (e.g. ~800 in our case; Table 1; Fig. 1) can reproduce deformation behaviour similar to various types of sediments, soils, and rocks. For example, numerical modelling of granular material with the Discrete Element Method was used to investigate features such as fault gouge mechanics (Morgan, 1999; Morgan and Boettcher, 1999), fault propagation (Schöpfer et al., 2006), comparative numerical and analogue direct/ring shear tests (Huhn et al., 2006), or particle shape influence on shear zone development and frictional strength (Kock and Huhn, 2006).

For each particle, microproperties such as coefficient of friction $\mu_{(P)}$ must be defined. These parameters control particle - particle interaction and are inherent to the modelling approach. In contrast, the overall mechanical and physical behaviour of the particle assemblage itself are the result of all particle interactions. Therefore, macroproperties (overall properties) of a particle assemblage have to be calculated, e.g. macroscopic friction $\mu_{(M)}$.

A complete review of the involved algorithms would exceed the scope of this paper. However, the numerical description of the code is completely represented by Cundall (1989), Cundall and Strack (1978; 1979; 1983) and Itasca (2004). Short overviews are given in other publications (Antonellini and Pollard, 1995; Kock and Huhn, 2006; Morgan and Boettcher, 1999). This granular modelling code (PFC2D) does not take fluids and grain fracture into account.

2.2 Modell

Consistent with analogue shear box experiments (e.g. Ask and Kopf, 2004; Kopf and Brown, 2003; Saffer et al., 2001; Saffer and Marone, 2003) and other numerical DEM simulations (e.g. Guo and Morgan, 2004; Huhn et al., 2006; Kock and Huhn, 2006; Morgan, 1999; Morgan and Boettcher, 1999) we developed a 2D numerical shear box (Fig. 1; Table 1). The lower and upper boundary wall consisted of 10 particles with a diameter of 20 µm, so the total box width was 200 µm. The lower wall remained fixed in x- and y-directions throughout all experiments. The upper wall could move in the x- and y-direction to induce shear ($\tau_{(M)}$) and normal stress ($\sigma_{N,(M)}$). The shear rate and the normal stress were held constant at 1µm/s and 5MPa, respectively, via servo algorithms applied to the upper wall. Thus, shear box height

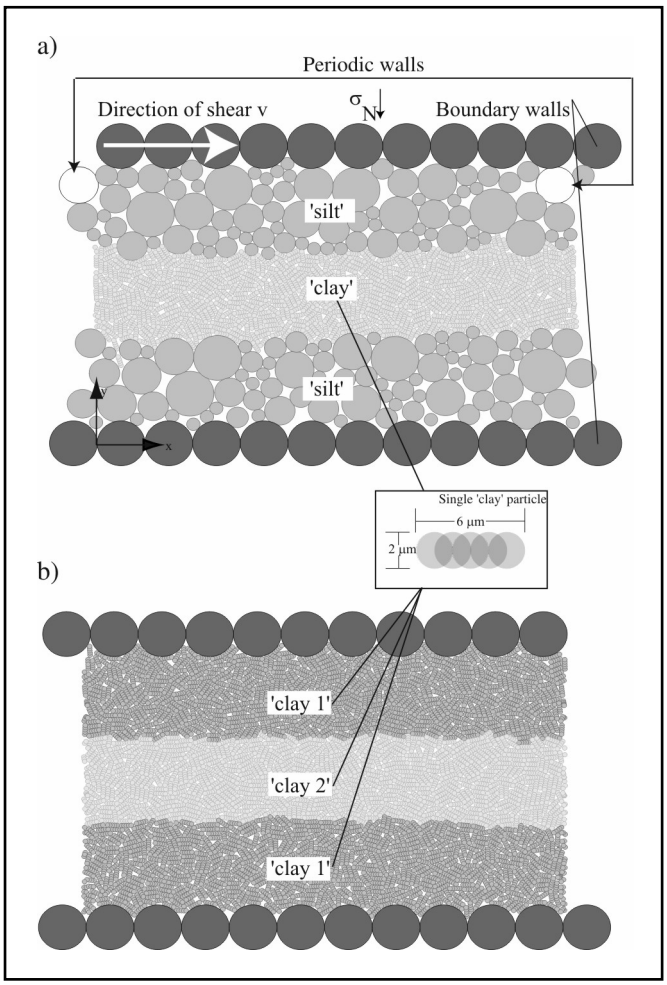

Fig. 1 Model of both 2D shear box experiments. The middle box shows 'clay' particles built of 5 spherical particles. The arrows show the periodic feature of the box: both white particles on either side are the same particle.

a) Indicated in medium grey is the 'silt', comprising of spherical particles. Dark grey are boundary particles 'walls'. In light grey appear the 'clay' particles.

b) Indicated in medium grey are the top and bottom layer 'clay'. Dark grey are boundary particles 'walls'. In light grey appear 'clay' particles of intermediate layer. 'Clay' particle shape and properties of all layers are equal, except particle friction for the intermediate layer.

was variable during each experimental run. Initial shear box height was 140 µm. To achieve large quantities of strain (200%) and keep computing time low, the left and right box boundaries were periodic, so that particles which moved out of the right side reappeared on the left.

Table 1: Properties and configuration of numerical models.

Shear box properties	Experiment I	Experiment II
Width [µm]	200	200
Height [µm]	140 (initial)	140 (initial)
Normal stress σ_N [Pa]	$5x10^6$	$5x10^6$
Shear velocity [µm/s]	6	6
Particle number: 'Silt'	162	0
Tabular particle number: 'Clay'	624	1872
Particle properties		
Normal stiffness k_N [N/m]	$1x10^9$	$1x10^9$
Shear stiffness k_S [N/m]	$1x10^9$	$1x10^9$
Density ρ [kg/m³]	*	*
Diameter [µm]: 'Silt' Diameter [µm]: 'Clay'	5.6 - 20 short axis: 2 long axis: 6	 short axis: 2 long axis: 6
Particle friction $\mu_{(P)}$ range:	0.05 - 1.0	0.05 - 1.0

* density is only relevant to compute the internal timestep and needs not to be realistic and therefore is scaled to an unrealistic high value to achieve a higher computing time.

As 'silt' grains appear approximately spherical in shape in nature (Bennett et al., 1991a), the numerical 'silt' is simulated by ideal spherical particles, whose diameters are log-normal distributed (e.g. Füchtbauer, 1988; Tucker, 1981) between 5.6µm to 20µm and a peak value at 10µm. In contrast, clay show a typical tabular, platy structure under natural conditions (Bennett et al., 1991a; Mitchell and Soga, 2005). Therefore numerous spherical particles were connected to simulate a tabular or stick-like shaped grain. These 'clay' sticks were constructed out of 5 spherical particles fixed relative to each other (Fig 1). This particle type has been successfully used to simulate normally consolidated 'clay' sediments (Kock and Huhn, 2006) and 'clay-silt' mixtures (Huhn et al., 2006).

These particles geometries were used to create two numerical materials (Table 1, Table 2):
(I) This 'sediment' consists of a numerical 'clay' layer sandwiched between two 'silt' layers (Fig. 1a). For this experiment we distinguished between to settings: (Ia) In the first case, the

microscopic coefficient of friction $\mu_{(P)}$ was varied stepwise from 0.01 to 1.0 for the 'silt' layers, while $\mu_{(P)}$ for the 'clay' remained constant (Experiments Ia-1 to Ia-9; Table 2). (Ib) In the second setting $\mu_{(P)}$ for 'silt' was held constant and varied stepwise for 'clay' from 0.01 to 1.0 (Experiment Ib-1 to Ib-9; Table 2). This experiment was used to study the deformational behaviour of 'sediments' which are stratified by distinct lithological boundaries. As a result of the experimental settings, there exist cases in which the particle coefficient of friction of 'silt' is smaller than that of 'clay'. These are the cases where particle friction contrast $\Delta\mu_{(P)}$ is negative (see Table 2). We realize that these cases may seem artificial, but they nonetheless offer insights into micromechanical behaviour of granular assemblies.

(II) To examine the deformation of sediments not stratified by lithology but rather by differences of material properties, we used a pure 'clay' assemblage (Fig. 1b). Hence, in this experiment a stratum of 'clay' was sandwiched between two 'clay' layers. Microproperties of all 'clay' particles were identical, except $\mu_{(P)}$ which was varied stepwise from 0.01 to 1.0 for the intermediate 'clay' layer, while $\mu_{(P)}$ for the upper and lower layer was held constant at 0.1 (Experiment II-1 to II-9; Table 2).

2.3 Analyse and interpretation techniques

Throughout the experiments up to shear strains of 200%, different material and macroscopic material properties were measured:

Displacement of each particle was recorded continuously and normalized gradients of these data were calculated and plotted with GMT (Wessel and Smith, 1991). These displacement gradients monitor internal deformation and mark the position and angle of slip planes and shear zones (Guo and Morgan, 2004; Huhn et al., 2006; Kock and Huhn, 2006; Morgan and Boettcher, 1999).

Macroscopic friction $\mu_{(M)}$ (defined as the ratio of measured shear stress $\tau_{(M)}$ and applied normal stress $\sigma_{N,(M)}$) was calculated at each 1% strain increment for the upper, intermediate, and bottom layers. To determine a relationship between shear strength and microproperties, average friction values from 0% to 200% strain were calculated. Note that the algorithm involved in calculating average friction values has to differ slightly for 'silt' and 'clay' particles. This is outlined in more detail in the appendix.

The percentage of contacts which are slipping was monitored at each 1% strain increment. Hence, its average value after 200% strain could be computed. Below, we use the term 'sliding fraction' for this parameter. Simultaneously, we recorded the angle of rotation for

each particle to calculate a) the portion of finite rolling of 'silt' grains and b) the amount of clay sticks which rotated more than 30°, 60°, 90°, or 180°.

Based on the slipping and rolling values, we are able to distinguish different deformation behaviours (sliding, rolling, and rotation).

The coordination number was computed throughout the experiment for all particles. This parameter is defined as the number of particle contacts of each particle. These values enable the identification of the evolution of typical microstructures which are associated with porosity changes.

3 Results

3.1 Localization features

Variation of $\mu_{(P)}$ for 'silt' in experiment Ia

Variation of $\mu_{(P)}$ of 'silt' particles resulted in different shear zone geometries (Fig. 2a,i-v).

Thus, negative friction contrast $\Delta\mu_{(P)} = -0.09$, when $\mu_{(P),'silt'} << \mu_{(P),'clay'}$, showed long shear planes mainly located in the upper silt layer (Fig. 2a,i), whereas only few short shear planes could be monitored inside the intermediate 'clays'. No internal deformation was observed in the lower 'silt', however the overall layer moved in shear direction. Shear planes in the upper 'silt' were inclined ~ ±25° from the horizontal. In some cases, single shear planes were connected. However, no coherent shear zone extending over the whole shear box could be observed.

An increase of $\Delta\mu_{(P)}$ to -0.05 resulted in an increase of deformation in the intermediate 'clay' layer (Fig. 2a,ii). Nevertheless, the majority of slip planes lie still in the top 'silt' and shear plane geometry was constant.

Further increase of $\Delta\mu_{(P)}$ to 0 led to a complete change of deformation (Fig. 2a,iii). In this case nearly all shear planes were located inside the 'clay' layer. There is no indication for internal deformation in the upper 'silt' layer, and even less in the lower one, while moving horizontally as a block. Shear planes in the 'clay' layer were narrower and shorter compared to previous experiments. Here, long shear zones extending over more than half of shear box width evolved (Fig. 2a,iii). The shear plane inclination distributed from -50° to +50°.

Successive increase of $\Delta\mu_{(P)}$ to 0.9 had no effect of localization features (Fig. 2a,iv-v), except that the border between 'silt' and 'clay' layers was more pronounced than in previous models.

Variation of $\mu_{(P)}$ for 'clay' in experiment Ib

Variation of $\mu_{(P)}$ of 'clay' (Table 2) caused also differences in localization of shear deformation (Fig. 2b,i-v).

In case of positive friction contrast $\Delta\mu_{(P)}$ ($\mu_{(P),'silt'} >> \mu_{(P),'clay'}$), shear planes exclusively localized in the intermediate 'clay' layer (Fig. 2b,i-ii). Shear planes were long and narrow with many interconnections resulting in a broad shear zone. In general, shear plane position and geometry were similar to experiment Ia-3 to Ia-9, where friction contrast was positive (Fig. 2a,iii-v).

An decrease of $\Delta\mu_{(P)}$ to 0 and to low negative values of -0.1 resulted in a shear plane localization shift towards the upper and also, to a lesser extent, lower 'silt' layer (Fig. 2b,iii-iv). When particle friction contrast $\Delta\mu_{(P)} = -0.8$ a long and broad shear plane was visible just on top of the 'clay', at the base of the 'silt' (Fig. 2b,v).

Fig. 2 (next page) Relative horizontal displacement plots. Red colours indicate maximum positive relative displacement, magenta indicates maximum negative displacement. Note that displacement is relative and not absolute, so that even for particles showing as magenta, absolute net displacement in positive x-direction > 0. Black bars indicate some selected slip planes. Slip plane notation after (Rutter et al., 1986). Black ellipse shows a stair step structure. Particle friction contrast $\Delta\mu_{(P)}$ is indicated above each plot.
a) Experiment Ia: Variation for the particle friction coefficient of 'silt' in the top and bottom layer. Particle coefficient of friction for 'clay' in the intermediate layer is constant with $\mu_{(P)}$=0.1. Specimen design is: 'Silt': top and bottom layer, 'clay': intermediate layer.
b) Experiment Ib: Variation for the particle friction coefficient of 'clay' in the intermediate layer. Particle coefficient of friction for 'silt' is constant in the top and bottom layer with $\mu_{(P)}$=0.2. Specimen design is: 'Silt': top and bottom layer, 'clay': intermediate layer.
c) Experiment II: Variation for the particle friction coefficient of 'clay' in the intermediate layer. Particle coefficient of friction for 'clay' is constant in the top and bottom layer with $\mu_{(P)}$=0.1. Specimen design is: 'clay': top, intermediate and bottom layer.

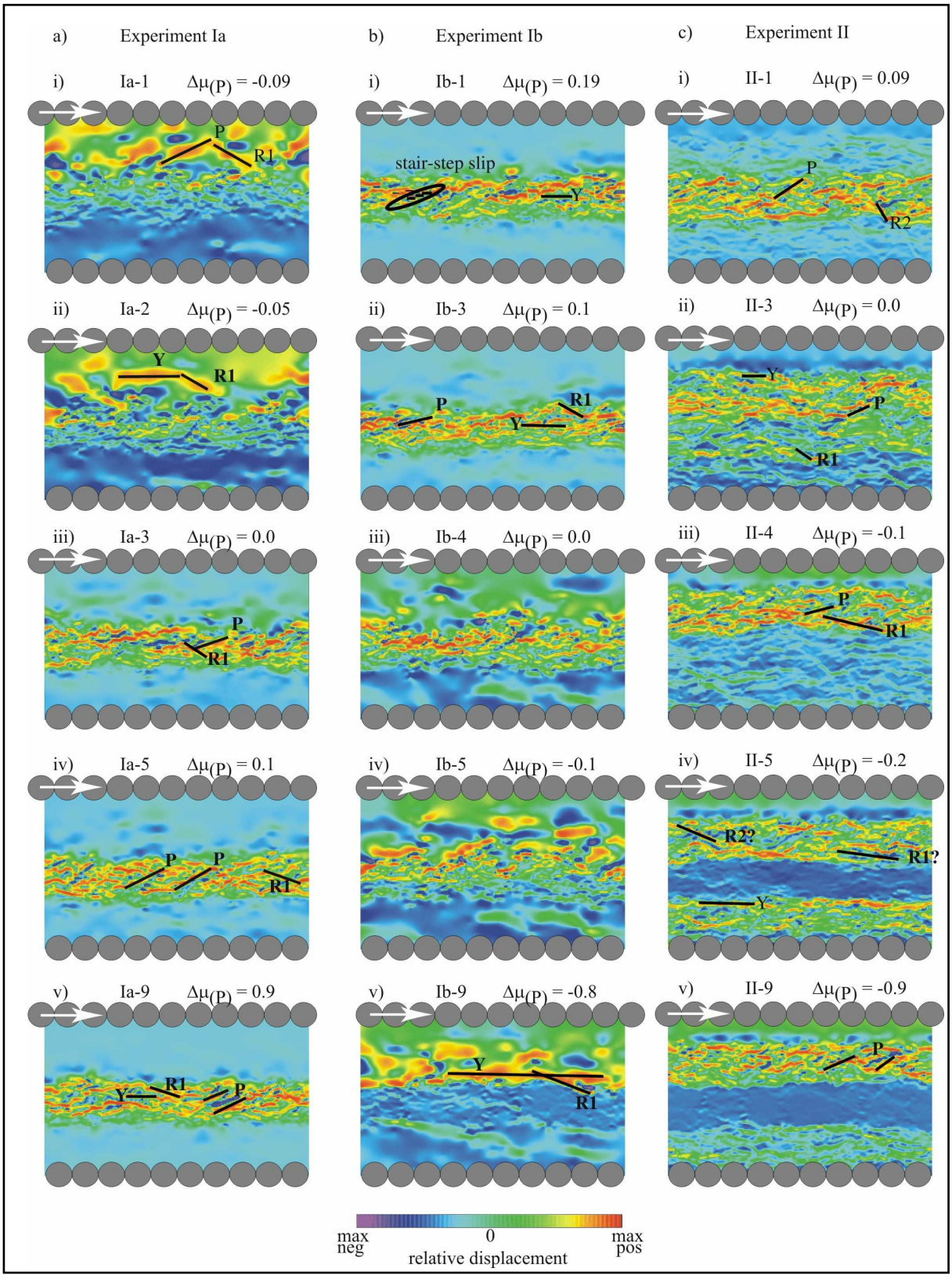
a) Experiment Ia
b) Experiment Ib
c) Experiment II
i) Ia-1 Δμ(P) = -0.09
i) Ib-1 Δμ(P) = 0.19
i) II-1 Δμ(P) = 0.09
P
R1
stair-step slip
Y
P
R2
ii) Ia-2 Δμ(P) = -0.05
ii) Ib-3 Δμ(P) = 0.1
ii) II-3 Δμ(P) = 0.0
Y
R1
P
R1
Y
Y
P
R1
iii) Ia-3 Δμ(P) = 0.0
iii) Ib-4 Δμ(P) = 0.0
iii) II-4 Δμ(P) = -0.1
P
R1
P
R1
iv) Ia-5 Δμ(P) = 0.1
iv) Ib-5 Δμ(P) = -0.1
iv) II-5 Δμ(P) = -0.2
P
P
R1
R2?
R1?
Y
v) Ia-9 Δμ(P) = 0.9
v) Ib-9 Δμ(P) = -0.8
v) II-9 Δμ(P) = -0.9
R1
Y
P
Y
R1
P
max neg
0
max pos
relative displacement

Variation of $\mu_{(P)}$ of the intermediate 'clay' in experiment II

In this experiment the particle coefficient of friction of the top and bottom layer of 'clay' was held constant at 0.1 (Table 2; Fig. 2c,i-v).

For the intermediate 'clay' layer positive particle friction contrast ($\mu_{(P),\text{intermediate 'clay'}} << \mu_{(P),\text{ top and bottom 'clay'}}$) resulted in a distinctly coherent shear zone located inside this layer (Fig. 2c,i). Its shape was in general comparable to that in experiment Ib-1 (Fig. 2b,i). Simultaneously, the top layer showed some weakly developed shear planes, so layer boundaries had no effect on localization.

The subsequent decrease of $\Delta\mu_{(P)}$ to 0.0 showed a broadening of shear plane localization into the upper layer where the majority of shear planes were located (Fig. 2c,ii). No distinct border in deformation behaviour between different 'clay' layers could be monitored.

Further decrease of $\Delta\mu_{(P)}$ to -0.1 resulted in a shear zone completely localized in the top 'clay' with few relative displacement respectively internal deformation in the intermediate and bottom layers (Fig. 2c,iii).

The subsequent decrease of $\Delta\mu_{(P)}$ to -0.2 and -0.9 showed a decrease of internal deformation in the intermediate layer (Fig. 2c,iv-v). Shear plane localization was mainly concentrated in the upper and to a lesser degree in the bottom layer.

3.2 Friction

Variation of $\mu_{(P)}$ for 'silt' in experiment Ia

As expected, variation of the microscopic particle coefficient of friction $\mu_{(P)}$ of the 'silt' particles influences the macroscopic coefficient of friction $\mu_{(M)}$ of the 'silt' layers themselves (Fig. 3a; Table 3). The increase from negative to positive friction contrasts resulted in an increase of $\mu_{(M),\text{'silt'}}$ from ~0.35 to a maximum of ~0.78 for the top and an increase from ~0.14 to a maximum of ~0.56 for the bottom layer. The increase of $\Delta\mu_{(P)}$ does not cause a change of the macroscopic friction for the 'clay', which stayed constant at ~0.37.

Variation of $\mu_{(P)}$ for 'clay' in experiment Ib

In this experiment, $\mu_{(M)}$ for the 'clay' ranged from ~0.34 to ~0.54 (Fig. 3b; Table 3). Here, the increase of friction contrast also resulted in variations of $\mu_{(M)}$ for 'silt' which ranged from 0.36 to 0.55 for the bottom and from 0.35 to 0.77 for the top layer.

Variation of $\mu_{(P)}$ for 'clay' in experiment II

Compared to the 'silt'-'clay'-'silt' sandwich, differences in macroscopic friction between 'clay' layers were small (Fig. 3b; Table 3). For positive particle friction contrast, macroscopic friction $\mu_{(M)}$ of the intermediate layer ranged from ~0.33 to ~0.35 and was lower than for the top and bottom layer. Then, with decreasing $\Delta\mu_{(P)}$, macroscopic friction increased to ~0.51, so that it was higher compared to the top and bottom layers. In contrast, the decrease of $\Delta\mu_{(P)}$, caused only a slight increase of $\mu_{(M)}$ for the top and bottom layers from ~0.36 to ~0.38. Thus, macroscopic friction was always highest in those layers where $\mu_{(P)}$ was lowest.

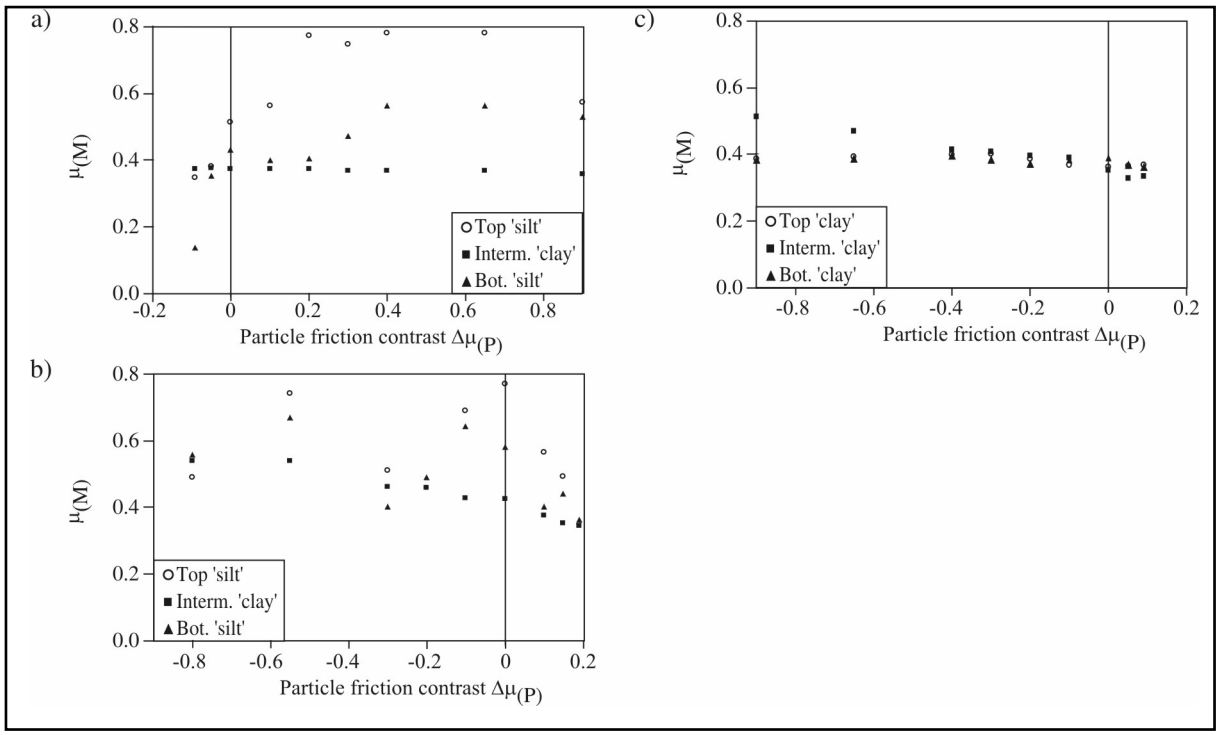

Fig. 3 Macroscopic friction $\mu_{(M)}$ vs. particle friction contrast $\Delta\mu_{(P)}$. $\mu_{(M)}$ is the average macroscopic friction from 0% to 200% strain, defined as the ratio of shear stress vs. normal stress. Circles denote $\mu_{(M)}$ for top layer, squares for intermediate layer, and triangles for bottom layer.
a), b), and c): same as Fig. 2.

3.3 Sliding fraction, rolling and coordination number

Variation of $\mu_{(P)}$ of 'silt' in experiment Ia

Effects on the 'silt' layers

The gradual increase of $\Delta\mu_{(P)}$ led to a decrease of sliding fraction of both 'silt' layers from ~50% to ~2% (Fig. 4a). The difference between the top and bottom 'silt' layer was negligible (~3%), except for $\Delta\mu_{(P)} \leq 0$.

Increasing $\Delta\mu_{(P)}$ caused a decrease in rolling, so that fewer 'silt' particles rotated to higher degrees (Fig. 5a; Table 3). For example at $\Delta\mu_{(P)} = -0.05$, after 200% strain 65% of the particles rolled to angles >30° and at $\Delta\mu_{(P)} = 0.9$ only 16% rolled to angles >30° after 200% strain. Furthermore, increasing $\Delta\mu_{(P)}$ led to a decrease of average coordination numbers from 4.8 to 4.1 (Fig. 6a; Table 3).

Effects on the 'clay' layer

The variation of $\Delta\mu_{(P)}$ had no significant effect on sliding fraction of the intermediate 'clay' layer where sliding fraction varied around 26%. However, if $\Delta\mu_{(P)} < 0.0$ ($\mu_{(P),\text{'silt'}} << \mu_{(P),\text{'clay'}}$), number of contacts slipping in the intermediate 'clay' layer was lower than in both 'silt' layers. Correspondingly, the magnitude of rotation of 'clay' particles in the intermediate layer stayed almost constant (Fig. 5b; Table 3).

The coordination number of the intermediate 'clay' layer was only affected for $\Delta\mu_{(P)} < 0.0$. It increased to 5.3 (Fig 6a; Table 3) compared to an average value of 5.0 and 5.1 calculated in all other experiments.

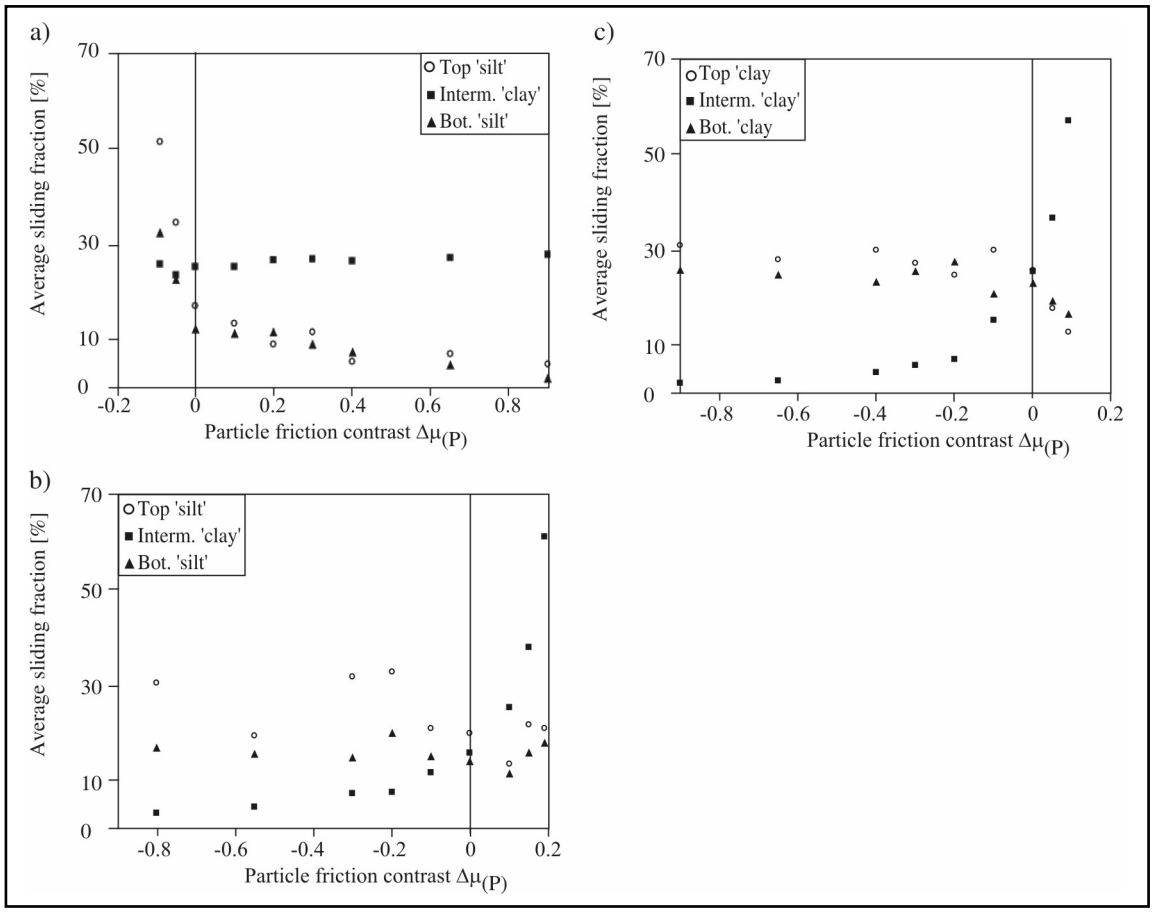

Fig. 4 Average sliding fraction vs. particle friction contrast $\Delta\mu_{(P)}$. Average sliding fraction is the percentage of interparticle contacts which slide calculated from 0% to 200 % strain. Circles denote sliding fraction for top layer, squares for intermediate layer, and triangles for bottom layer.
a), b), and c): same as Fig. 2.

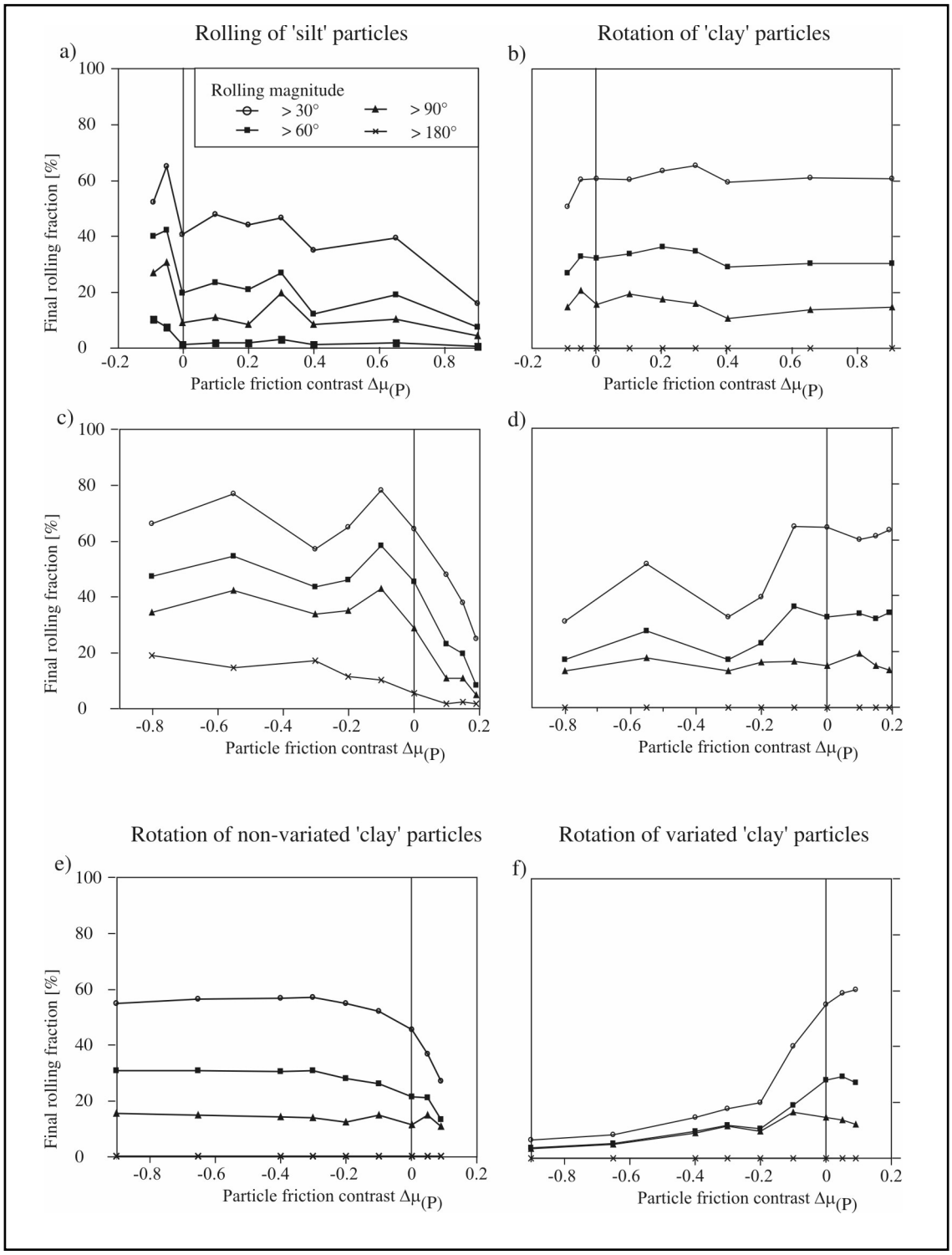

Fig. 5 Final (200% strain) rolling magnitude and fraction vs. particle friction contrast $\Delta\mu_{(P)}$. At 0% strain, all particles had rolled 0°. At 200% strain: circles denote percentage of particles which rolled to angles >30°, squares denote percentage of particles which rolled to angles >60°, triangles denote percentage of particles which rolled to angles >90°, 'x' denote percentage of particles which rolled to angles >180°.
a), b): same a) in Fig. 2; c), d): same as b) in Fig. 2; e), f): same as c) in Fig. 2

Variation of $\mu_{(P)}$ for 'clay' in experiment Ib

Effects on the 'clay' layer

Increase of $\Delta\mu_{(P)}$ led to a increase of sliding fraction for 'clay' from ~3% to ~61% (Fig. 4b; Table 3). The increase of particle friction contrast caused a general increase in rotation magnitude (Fig. 5d; Table 3). The coordination number increased gradually from 4.4 to 5.3 when $\Delta\mu_{(P)}$ was increased (Fig. 6b; Table 3).

Effects on the 'silt' layers

In experiment Ia, $\Delta\mu_{(P)}$ had only a significant effect on the layers whose particle coefficient of friction was varied. In contrast, in experiment Ib, variation of $\Delta\mu_{(P)}$ also influenced the micromechanical properties of the neighbouring layers (Fig. 4b; Table 3).

In contrast to all previous experiments, sliding fraction showed no systematic trend in relation to $\Delta\mu_{(P)}$, rather it was highly variable. However, if $\Delta\mu_{(P)} < 0.0$, sliding fraction of 'silt' layers was always higher than that of the intermediate one. The magnitude of rolling for 'silt' decreased rapidly when $\Delta\mu_{(P)} > 0.0$ (Fig. 5c; Table 3). When $\Delta\mu_{(P)} < 0.0$, rolling varied around a mean percentage for each threshold angle.

Similarly the change of $\Delta\mu_{(P)}$ had an effect on the coordination number of 'silt' (Fig. 6b; Table 3). Overall, the average coordination number increased from 4.1 to 4.9 when $\Delta\mu_{(P)}$ was increased.

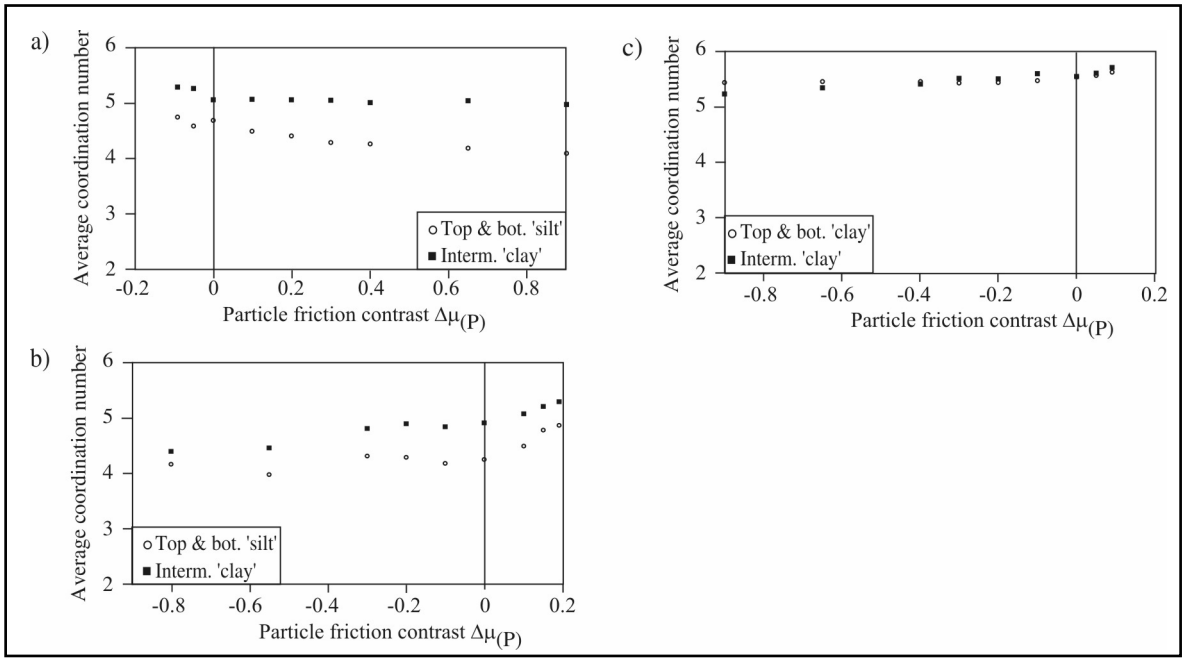

Fig. 6 Average coordination number vs. particle friction contrast $\Delta\mu_{(P)}$. Average coordination number is the average number of contact points per particle averaged from 0% to 200% strain. Circles denote top and bottom layer, squares denote intermediate layer.
a), b), and c): same as Fig. 2.

Variation of $\mu_{(P)}$ of the intermediate 'clay' (experiment II)

Effects on the intermediate 'clay' layer

The sliding fraction increased with increasing particle friction contrast from ~2% to ~57% (Fig. 4c; Table 3). Similarly, rotation magnitude increased from 8% to 60% (Fig. 5f; Table 3). Furthermore, increasing $\Delta\mu_{(P)}$ resulted in a increase of average coordination number from 5.2 to 5.7 for the modified layer.

Effects on the top and bottom 'clay' layers

An increase of $\Delta\mu_{(P)}$ caused an decrease in sliding fraction to ~13%. For $\Delta\mu_{(P)} < 0.0$ sliding fraction of the top and bottom layer was always greater than for the intermediate layer and highly variable (Fig. 4c; Table 3). Correspondingly, rotation magnitude decreased for positive particle friction contrast and stayed almost constant for negative particle friction contrast (Fig. 5e; Table 3). Coordination numbers for the top and bottom 'clay' layers showed a very small increase from 5.4 to 5.6 (Fig. 6c; Table 3) once $\Delta\mu_{(P)} > 0.0$.

4 Discussion

4.1 Localization patterns

Our results showed typical deformation structures also observed in analogue tests (Maltman, 1994a; Marone, 1998; Scholz, 2002). Specifically, we interpret the slip planes observed (see Fig. 2, section 3.1) to be similar to R_1, R_2, P, and Y fractures (e.g. Maltman, 1994b; Scholz, 2002; Fig. 2).

Slip plane coinciding to P and R_1 shears are shown in the top 'silt' layers in experiment Ia and Ib (Fig. 2a,i-ii; Fig. 2b,iv-v). These fractures only appeared in the 'silt' when particle friction contrast $\Delta\mu_{(P)}$ was negative. These slip planes are not very well pronounced which may be partly due to the low layer height. However, similar structures have been observed in other numerical studies (Kock and Huhn, 2006; Morgan and Boettcher, 1999) and are commonly defined as Riedel structures and comparable to results from natural specimen (Huhn et al., 2006).

P and R_1 fracture types were more pronounced in the 'clay' layers in all experiments. P-fractures extending nearly over the entire height of the 'clay' layer started to form at positive particle friction contrasts (Fig. 2a,iii-v; Fig. 2b,i-ii; Fig. 2c). As in nature (Rutter et al., 1986), this is an indication for particle alignment. An example of this is illustrated in Fig. 7a, where particle alignment and orientation enhanced slip and led to fractures along domains of similar preferred grain orientation.

Usually, Y-shears are interpreted to accommodate large amounts of slip (Rutter et al., 1986; Scholz, 2002). Since our models achieved a strain of 200% we would expect well pronounced Y-shear planes in all experiments (Fig. 2). With the exception of experiment Ib (Fig. 2b,v), this was not the case. We assume that on a grain scale level, a single Y-plane may be exchanged for a multitude of parallel oriented stair step slip planes (e.g. Fig 2c,i). Each step was oriented parallel to the shear box width, making up very small Y-shear planes. The complete step-like structure however seemed to be parallel to the P orientation (Fig 2c,i; black ellipse) which is interesting since Y-planes are attributed to deflect small scale (Rutter et al., 1986) and large scale (Maltman, 1994a) movement in the P-direction. On our microscopic scale, these stair-case structures indicate slip along or slip of few 'clay' particles (Fig. 7b). This means that the mode of slip (Y or P) was controlled by few particles at the grain scale level where long Y-planes only developed if all the small scale Y-planes at each particle could connect.

Similar to natural materials (Rutter et al., 1986), R_2 slip planes were seldom in our models. One example for the R_2 orientation is found in experiment 2 (Fig. 2c,i). Morgan and Boettcher (1999) found R2 structures in DEM models with spherical particles, so the 'silt' layer height in our models may be too small to reproduce such features. However, in a similar experiment with a larger shear box we observed these features (Kock and Huhn, 2006). In the 'clay' layer, slip is clearly dominated by deformation structures analyzed before, so there seems to be no geometric need for R2 fractures.

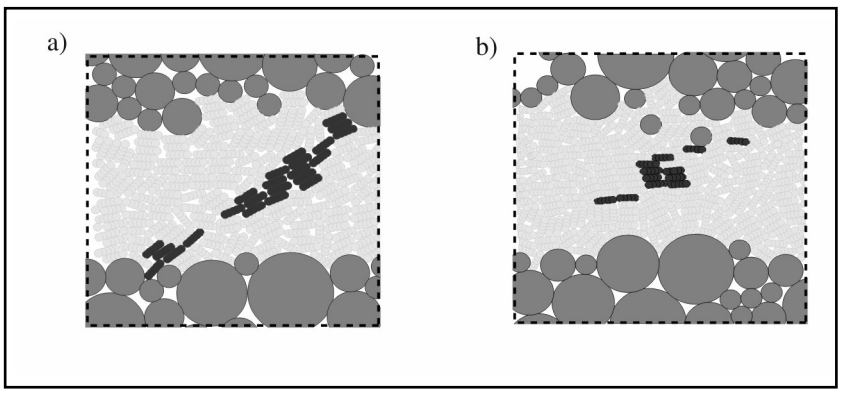

Fig. 7 Close-up particle configuration for selected models after 200% strain. Dark grey particles: 'silt'; medium grey particles: 'clay'. a) Black particles show particle alignment corresponding to P-shears in Fig. 2a,v; experiment Ia-9. b) Black particles show particle alignment corresponding to stair-step structure in Fig. 2b,i; experiment Ib-1.

4.2 Micromechanics

Deformation modes

Deformation at interparticle contacts may occur in two ways for spherical particles: contact sliding or rolling. The extent to which sliding is active depends on $\mu_{(P)}$ (Morgan, 1999). For spherical particles, sliding decreases with increasing $\mu_{(P)}$ while rolling increases. In case of tabular 'clay' particles rolling is replaced by rotation which is difficult to achieve for an elongated particle (Mitchell and Soga, 2005). It is most effective only during the initial stages of deformation by microstructure breakdown. After microstructure breakdown, which depends on particle shape and sphericity, sliding is the dominant deformation mechanism (Kock and Huhn, 2006).

The different amount of sliding, rolling, and rotation controls the observed localization features. Our results indicate that this relationship can be explained by particle friction contrasts and shape. In the 'silt'-'clay'-'silt' sandwiched layers, when $\Delta\mu_{(P)} < 0.0$, sliding fraction was highest in the top 'silt' layer. That means that sliding for spherical particles with low particle friction is a more favoured deformation mode than 'clay' sliding and rotation.

When particle friction contrast was zero, sliding fraction was highest in the 'clay' layer (experiment Ia-3) or differences between sliding fractions were small (experiment Ib-4). Here, sliding and rotation of 'clay' particles were the dominant deformation mechanisms. This trend continued when friction contrast was positive, so that particle friction of 'clay' was lower than for 'silt'. In fact, as indicated by very low sliding fraction and low rolling magnitudes, relative deformation inside the top 'silt' layer was almost non-existent in these cases (Fig. 2a,iii-v; Fig. 2b,i-ii). This resulted in a complete decoupling from the rest of the material. The 'silt' layer slid like a rigid body over the intermediate 'clay' layer.

Another indication for the fact that the 'silt' layer behaved like a rigid body is the decrease of coordination number with increasing particle friction. Thornton (2000) argued that the stability of a particle assemblies increased with increasing $\mu_{(P)}$. The number of contacts required for a stable configuration was lowered while the coordination number was reduced. This also explains one major difference between experiment Ia and Ib when friction contrast was negative: The long slip plane that developed at the base of the 'silt' layer (Fig. 2b,v) shows that the 'clay' acts as a rigid body so that the 'silt' layer could effectively slide over it. In experiment Ia, particle friction of 'clay' was too low to produce a stable and rigid layer, so there do appear some slip planes (Fig. 2a,i) in it.

Since in pure 'clay' experiment the particle shape was identical for all layers, only 'clay' sliding and rotation did play a role during shear. Localization consequently occurred in layers where $\mu_{(P)}$ is lowest, and where sliding fraction and rotation magnitude are highest. When sliding fraction was > ~30% for a layer, localization occurred (Fig. 4c). Furthermore, when more than 40% of particles rotated more than 30°, localization occurred in these layers (Fig. 5e-f).

Sliding and rotation are dominant during different stages of deformation. Rotation is initially important, when 'clay' microstructure disaggregates. After that, particle alignment has progressed to such an extent that particle sliding is enhanced as the dominating process: The alignment of particles leads to structures which are also observed in nature, such as domains of preferred orientation (Bennett et al., 1991a; Mitchell and Soga, 2005).

Why does localization occur in high strength layers?

Surprisingly, in some experiments deformation was also localized in layers where the measured macroscopic coefficient of friction $\mu_{(M)}$ was higher than in the surrounding material. These cases are parts of experiment Ia where the macroscopic friction $\mu_{(M)}$ of the bottom 'silt' layer was lowest and localization nonetheless concentrated in the top 'silt' and the 'clay' (Fig. 2a,i-ii). At first sight, this contradicts the fact that in natural materials localization should concentrate in the mechanically weaker layer.

For experiment Ia, we think localization of slip planes did not happen in the bottom 'silt' layer, because the sample effectively had decoupled once deformation reached the intermediate 'clay' layer. The upper part of the whole assemblage thus slid over the lower part with the slip planes in the top 'silt' and 'clay' layer acting as interfaces. Thus, shear stress transmission to the bottom layer lowered. Consequently, since friction $\mu_{(M)}$ is defined as the ratio shear stress $\tau_{(M)}$ and applied normal stress $\sigma_{N,(M)}$, overall friction was low.

Nevertheless, in case of negative particle friction contrast, deformation not only localized in the 'silt', but also in the 'clay' which showed the strongest macroscopic friction. We assume this happened because 'clay' microstructure breakdown is different in stratified sediment compared to pure 'clay' material during the initial stages of deformation: In a pure 'clay' material, microstructure breakdown is associated with particle alignment and the resulting enhancement of sliding (Experiment II; Kock and Huhn, 2006; Lambe and Whitman, 1969; Mitchell and Soga, 2005). This does not necessarily happen in stratified sediment. When 'silt'

particles slide, the ‘clay’ particles can easily move into the gaps between ‘silt’ particles. For negative particle friction contrasts (Fig. 8a) the boundary between layers is blurred much more than for positive (Fig. 8b). When particle friction contrast is positive, the ‘silt’ becomes more stable, sliding is reduced, and the amount of gaps where ‘clay’ particles can move into become fewer.

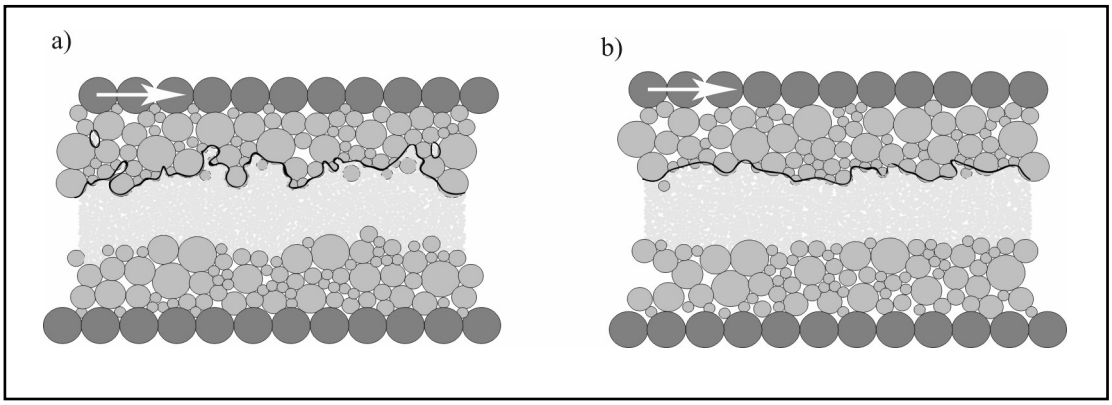

Fig. 8 Particle configuration after 200% strain for selected model runs. Black line indicates top layer boundary. Light grey particles: ‘clay’; medium grey particles: ‘silt’; dark grey particles: ‘walls’. a) $\Delta\mu_{(P)}$ = -0.09; experiment Ia-1: After 200% strain, layer boundaries are blurred. ‘Clay’ particles have slid into gaps between ‘silt’ particles. b) $\Delta\mu_{(P)}$ = 0.9; experiment Ia-2: After 200% strain, layer boundaries are still mostly intact.

4.3 Implications for natural materials

Experiment (I) showed that deformation primarily took place in the ‘clay’ layers. In these cases, displacement was distributed throughout the layer. On grain-scale level in natural sheared clays, we would thus expect a multitude of possible slip planes with minimal displacement rather than a narrow slip plane where a large part of displacement accumulated. This network of slip planes is similar to the microscopic appearance in scaly clays (e.g. Vanucchi et al., 2003).

There are several experiments where shear was located not exclusively in the ‘clay’ layer, but where displacement was localized at least partly or almost exclusively in the top ‘silt’ layer (Fig. 2a,i-ii, Fig 2b,iii-iv, Fig. 2b,v). In the former case, displacement and shear were distributed across the layer boundary and within the layers. In general, natural situations where $\mu_{(P),\text{‘silt’}} < \mu_{(P),\text{‘clay’}}$ may be sparse, but scenarios where loose soil overlies cemented clay or welded volcanic ash may be conceivable. To this regard, Sperrevik et al. (2000) showed that development of clay smears depends on the competence contrast between sand and clay. This may be applicable to our results although their testing setup is different from ours in the respect that they use a vertical slab of clay in a loose sand as their soil specimen. The latter

case represents an end-member of our experiments and its resemblance in natural systems is rare. However, cases where the contact between layers acts as the weak part during shear have been described in the literature (Hatzor and Levin, 1997).

One of the most interesting features of experiment II is its sensitivity to small changes of particle properties. The shift from negative to positive particle friction led to completely changed localization features (Fig 2c,i-iii), although absolute change of particle friction was small. For natural clay that indicates that even small changes in e.g. mineral composition, cementation, etc. could result in highly different displacement and localization patterns. That may explain deformation processes where shear localization occurred only in defined areas of a complex clayey lithology, such as the Barbados prism décollement (Labaume et al., 1997; Maltman et al., 1997) or for microscopic scale S-C band formation in clays (Labaume et al., 1997; Takizawa and Ogawa, 1999).

5 Conclusions

We conducted numerical DEM simulations on two types of layered specimen: (1) A 'silt'-'clay'-'silt' assemblage and (2) a 'clay'-'clay'-'clay' package.

Our results indicate that localization is not a simple function of macroscopic frictional strength, but a complicated mechanism on the grain scale level. Particle sliding, rolling and rotation are observed modes of deformation. The amount to which each of these deformation modes occurs is governed by the particle friction contrast. Particle friction contrast between layers determines where localization will occur, because precedence of deformation modes changes:

For negative particle friction contrast, 'silt' sliding is a more favoured deformation mode than 'clay' sliding and rotation, although this situation hardly shows in nature. For positive particle friction contrast, sliding and rotation of 'clay' particles are the dominant deformation mechanisms, which results in a complete decoupling from the rest of the material.

For stratified 'clay' there are threshold levels for sliding and rotation which determine where localization occurs: Sliding fraction has to be > ~30% and more than 40% of particles have to rotate more than 30° for deformation to localize in a layer.

Furthermore, there were two cases where macroscopic friction was very low in the bottom layer, but no deformation was observed. We assume that the material decoupled in one of the upper layers, so that shear stress transmission to lower layers was prohibited and friction values were low.

Observed localization structures showed remarkable similarity to natural sediments. Classical Riedel structures on the grain scale level allowed observing deformation microscopically. In some cases features that might develop into Y-shears were observed, while P- and R1 type shear planes were abundant in all models. Additionally, the 'clay' type material shows a distinct connection between slip planes and particle alignment.

Comparing the model with nature showed in general some interesting correlations to features observed in scaly clays and similarities to S-C band formation. This implies that the micromechanical behaviour we observed is applicable. Nevertheless, there is a wide range of features during sediment deformation which could not be captured by our models. Grain breakage, fluid involvement and 3-dimensionality certainly influence deformational behaviour of rocks and need further analysis.

Acknowledgements

Funding for this research has been received through Deutsche Forschungsgemeinschaft via the Research Center Ocean Margins (RCOM). This is RCOM publication # xxx.

We thank reviewers. We owe many thanks to our colleague Achim Kopf from the Research Center Ocean Margins for advice and discussions on an earlier version of the manuscript.

Appendix

Since the macroscopic coefficient of friction $\mu_{(M)}$ is defined as the ratio of measured shear stress $\tau_{(M)}$ and applied normal stress $\sigma_{N,(M)}$, the average stress tensor for the complete particle assemblage $\bar{\sigma}_{ij}$ had to be calculated. In a granular material stresses only exist in the particles and the average stress tensor $\bar{\sigma}_{ij}$ can be computed by summing all particulate stress tensors scaled by their volume with (Itasca, 2004):

$\bar{\sigma}_{ij} = \frac{1}{V}\sum_{Np}\sigma_{ij}^{(p)}V^{(P)}$, where

$\bar{\sigma}_{ij}$ (i,j =1,2): average stress tensor of the particle assemblage, V :assemblage volume, Np : particle number, $\sigma_{ij}^{(p)}$ (i,j =1,2): particle stress tensor and $V^{(P)}$: particle volume. Then, $\tau_{(M)} = \bar{\sigma}_{12}$.

This relation poses no problems as long as single particles are not connected to form a rigid, greater particle (in this appendix called a 'clump'). However, the averaging procedure becomes unstable once particles are connected and overlap as the 'clays' in our experiments do. Simple averaging does not work since particle stresses of the single particles building up the clump are not referenced to the clump centre of rotation, but still to their own particle

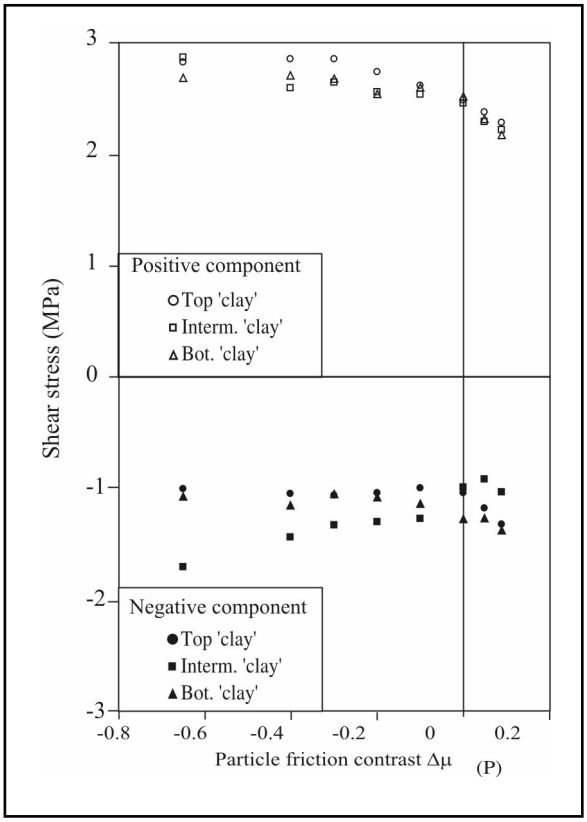

Fig. 9 Positive and negative components of the average stress tensor for all model runs of experiment II. Positive component shows a slight decrease with increasing particle friction contrast. Negative component stays almost constant for the top and bottom layer, but shows a strong decrease for the intermediate layer with decreasing particle friction contrast.

centre. The effect of simple averaging leads to the following phenomenon:

An increase in particle friction also means a decrease in coordination number and an increase in layer stability (Thornton 2000). Considering the particle shear stress ($\sigma_{12}^{(p)}$) it is evident that it may have either a positive or negative sign, which contributes to clump rotation in the clockwise or counter clockwise direction, respectively. Since the enhanced stability works in all directions, this does not pose a problem as long as the material is in equilibrium. But once the material is compacted and shear stress is induced one direction is favoured (Fig. 9): The absolute positive values were always higher than the absolute negative values of $\overline{\sigma}_{12}$.

This illustrates the sense of shear, since shear in the positive x-direction leads to clockwise clump rotation and thereby to high positive values. Additionally, the positive values showed a slight decrease with increasing particle friction contrast and were nearly the same for all layers. The negative values however, were almost constant only for the top and bottom 'clay' layer. For the intermediate 'clay' layer the negative values decreased strongly with decreasing particle friction contrast. Thus, the averaging procedure would lead to decreasing macroscopic friction while particle friction increased. To overcome this drawback we further on used a different approach where we ignored the direction of shear stress for the single 'clay' particles building a clump. Specifically we now calculate $\overline{\sigma}_{12}$ as the average of the absolute positive and negative values. These values are used in Fig. 3 for the 'clay' layers.

The whole phenomenon of one direction becoming favoured may be related to the development of contact force distribution between all particles. Rothenburg and Bathurst (1992a) observed that during biaxial compaction the number of vertical contacts remained almost constant whereas the number of horizontal contacts decreased. In our experiments the material was forced to move in positive x-direction, which may result in anisotropy of contact force distribution. Further studies in this direction are needed.

Chapter V

Comparative numerical and analogue shear box experiments and their implications for the mechanics along the failure plane of landslides

Published: Katrin Huhn, Ingo Kock & Achim J. Kopf, Norwegian Journal of Geology 86, 209 - 220

Abstract

It has long been known that failure of soils is controlled by intrinsically weak mineral phases (such as clays) and transient pore pressure fluctuations. Both factors may be involved in triggering of slope failure; however, it is unclear to what extent each of them contributes. To shed light on this problem, we compare geotechnical shear tests on dry mineral standards (clays, quartz) and numerical 'shear box' experiments using the Discrete Element Method (DEM) on dry particle assemblages. The role of fluid is additionally monitored by adding water in the analogue tests (humid to fully saturated conditions). A series of geotechnical shear tests (up to 40 MPa normal stress) and numerical 'shear box' models in a fluid-free environment indicate that sediment composition (namely the presence of clay minerals) is a major factor in shear strength or frictional stability of granular materials. Because μ is further affected by fluid saturation, an effect that is maximized in swelling clays, added humidity or aqueous fluid cause μ to decrease by a factor of 4 in the analogue tests. However, our data suggest that mineralogical control alone may be sufficient to trigger slope instability, for instance owing to the concentration of clay minerals in zones of weakness. Fluids may enhance the effect by lowering effective stresses.

1 Introduction

A thorough understanding of processes occurring at the basal shear zone of gravitational mass movements is fundamental to identify why some slopes destabilize while others do not. Slope failure occurs if applied forces which are acting to produce shear, e.g. sedimentary loading, tectonic processes, or gravity, exceed the resisting force or the shear strength of a potential basal shear zone embedded in the slope material. Shear strength of granular materials is derived from a number of primary factors, such as sediment/mineral composition, texture, humidity, or pore fluid effects (e.g. Brace and Byerlee, 1966; Byerlee, 1978; Dieterich and Conrad, 1984; Horn and Deere, 1962; Krantz, 1991; Lambe and Whitman, 1969; Lohrmann et al., 2003; Marone, 1998; Morgan, 1999). While mineral composition and texture/porosity are directly linked to parameters such as coefficient of friction (μ) or cohesion (C), other factors are transient and less easily identified and quantified. However, the presence of fluids and their variation in time and space, as attested by pore pressure fluctuations, have been shown to play a major role on faulting (see benchmark work by Hubbert and Rubey, 1959). In recent time, excess pore pressure has also been put forward to be a major player in triggering landslides. Processes responsible for transient pore pressure increase are mineral dehydration processes, hydrocarbon formation, rapid sedimentation, tectonic loading, or gas hydrate dissociation. Therefore it is now widely accepted that slope destabilization is closely related to the presence of mechanically weak layers, a rapid increase of pore pressure, or a combination of both (e.g. Hampton et al., 1978; Loseth, 1999).

To gain a deeper insight into the role of physical material parameters for the shear strength of granular materials, a growing number of geotechnical experiments and numerical studies on soils have been developed (e.g. Kopf and Brown, 2003; Lohrmann et al., 2003; Marone, 1998; Morgan, 1999; Saffer et al., 2001). Geotechnical laboratory tests suggest that the composition and texture of sediments are crucial for shear strength whereas frictional stability is a function of the change in friction coefficient (μ) at a given effective stress and shear rate (e.g. Kopf and Brown, 2003; Lohrmann et al., 2003; Marone, 1998; Saffer et al., 2001; Scholz, 1998). The most likely explanation for this observation is a change in active particle surface area, textural evolution, and particle migration. Furthermore, particle size distribution has a significant effect on shear strength and frictional behaviour of granular assemblages of ideal spherical ‘grains’ shown also by numerical shear box experiments (e.g. Morgan, 1999; Morgan and Boettcher, 1999). Besides, arbitrarily shaped particles, e.g. triangular and rounded particles, determine the macroscopic deformation behaviour and the magnitude of the

coefficient of friction under shear stress (Guo and Morgan, 2004). However, replacement of clays in shear zones, mineral transformation, lithification processes by precipitation, and - most importantly - complete water saturation of a fine-grained soil have been found to cause a decrease in frictional strength, as indicated by either unstable stick slip or conditionally stable behaviour (e.g. Dieterich and Conrad, 1984; Moore and Saffer, 2001).

Although there are advantages and shortcomings in both soil mechanical tests and their numerical simulations, geotechnical tests prevent a direct observation of the temporal and spatial evolution of shear zones during the experiment. Information about grain interaction and particle behaviour along the shear plane itself is limited to investigations after the experiment was stopped. Simultaneously, numerical shear box experiments do not allow the presence of pore fluids and fluid-grain interaction up to now. Hence, we combine standard soil mechanical tests with numerical shear box experiments using a new simulation technique in geosciences - the Discrete Element Method (DEM; Cundall and Strack, 1979). DEM is based on a granular approach which has been successfully utilized to simulate the behaviour of non-cohesive systems in discrete shear experiments under high stress conditions (e.g. Guo and Morgan, 2004; Morgan and Boettcher, 1999).

Our paper focuses on how sediment composition controls the shear strength of clay-rich sediments. The main hypothesis to test is whether mineralogy alone may account for weakening of sediments or whether pore pressure plays an important key role. We present preliminary results of recent DEM experiments examining the influence of the concentration of elongate particles, simulating a ‘clay’ sediment, to get a better understanding of laboratory measurements of shear strength. The comparison of dry DEM and analogue shear tests indirectly allows us to assess the role of pore pressure (as also measured with complementary analogue experiments).

This combination will bring us a step closer to understanding the trigger mechanisms of slope destabilisation and enable an improvement of both experiment configurations and interpretations.

2 Methodical background

2.1 Geotechnical (analogue) shear tests

2.1.1 Sample selection and preparation:

Mineral standards of smectite, illite, kaolinite, and chlorite (WARDs) were size-separated in order to remove contaminations of quartz and heavy minerals, especially since earlier deformation tests led to overestimated frictional strength of illite clay due to >25% contamination in the WARDs illite shale (Marone et al., 2001). For that purpose, the material was ground, rehydrated, and spun down using a centrifuge twice. Semiquantitative XRD analyses at Missouri University (M. Underwood, unpublished data) revealed that >96% of the residue consisted of smectite, illite, and kaolinite. Samples were then measured as pure end members as well as mixtures of the clay with quartz standard. The quartz end member is a mesh 140 silt (grain size <0.105 mm) from FISHER. The sediment samples underwent several procedures:

(1) The size-separated fine fraction of the clay standards was dried for >72 hrs. at 120°C (see discussion in Moore and Lockner, 2004), powdered, and then dried again to remove laboratory humidity. The samples were then immediately placed into the shear box and loaded to the desired normal stress (1, 2, and 5 MPa). Interaction between dry sample and humid air in the air-conditioned laboratory was minimized due to rapid sample transfer and immediate testing. This procedure allows to simulate arid to humid conditions/light rainfall in the laboratory.

(2) Another split of the same size-separated clay standard was rehydrated in pore fluids of variable ion contents. Salinity ranged from 0% (de-ionised water), 0.5x seawater concentration (50% de-ionised water and 50% seawater), seawater, and 1.5x seawater (i.e. brine-like fluid produced by evaporation on a hot plate). An aliquot of each clay mineral was rehydrated in the solution (>72 hrs.) prior to consolidation and shear. This procedure allows us to simulate conditions of heavy rainfall to the marine realm in the laboratory.

2.1.2 Geotechnical procedures:

Two different types of shear tests were carried out: Ring shear tests were conducted in a standard Wykeham - Farrance Bromhead ring-shear apparatus (WF 25850) at progressive loading stages up to normal stresses of 2.5 MPa (for details, see Bishop et al., 1971, and Fig. 1a). All residual tests were conducted at slow displacement rates of between 0.001 and 0.01 mm/s to maintain conditions as near to undrained as possible (in the case of the water-

saturated samples). Given that the sample chamber contains two rings fitting snugly into each other (see Figs. 1 and 6), dry tests were not affected by room humidity.

Direct shear tests were conducted in a modified GEOCOMP direct shear apparatus, in which the initially 30 to >70 mm-thick samples were carefully loaded to different normal stress levels of up to 40 MPa for testing. During shearing of the then ~15 mm-thick sample, pore pressure across the fault zone was monitored via three porous ports that penetrate the lower half (~10 mm) of the sample and tap into the level of the shear zone.

2.1.3 Scanning Electron Microscopy (SEM):

Selected samples were studied microscopically after the shear tests by SEM. The system used is a FEI Quanta 600 which operates in both regular high-vacuum mode, low-vacuum mode (to eliminate charging) and environmental mode. The latter was used for the majority of the clay-bearing samples. Voltage ranged from ~500 V to ~3 kV during our investigations. The environmental mode allowed 100% relative humidity and gave tolerable results even for specimens sheared after full seawater saturation. For the latter samples, small fragments were analysed to gain quality images. Coating of the samples was not necessary.

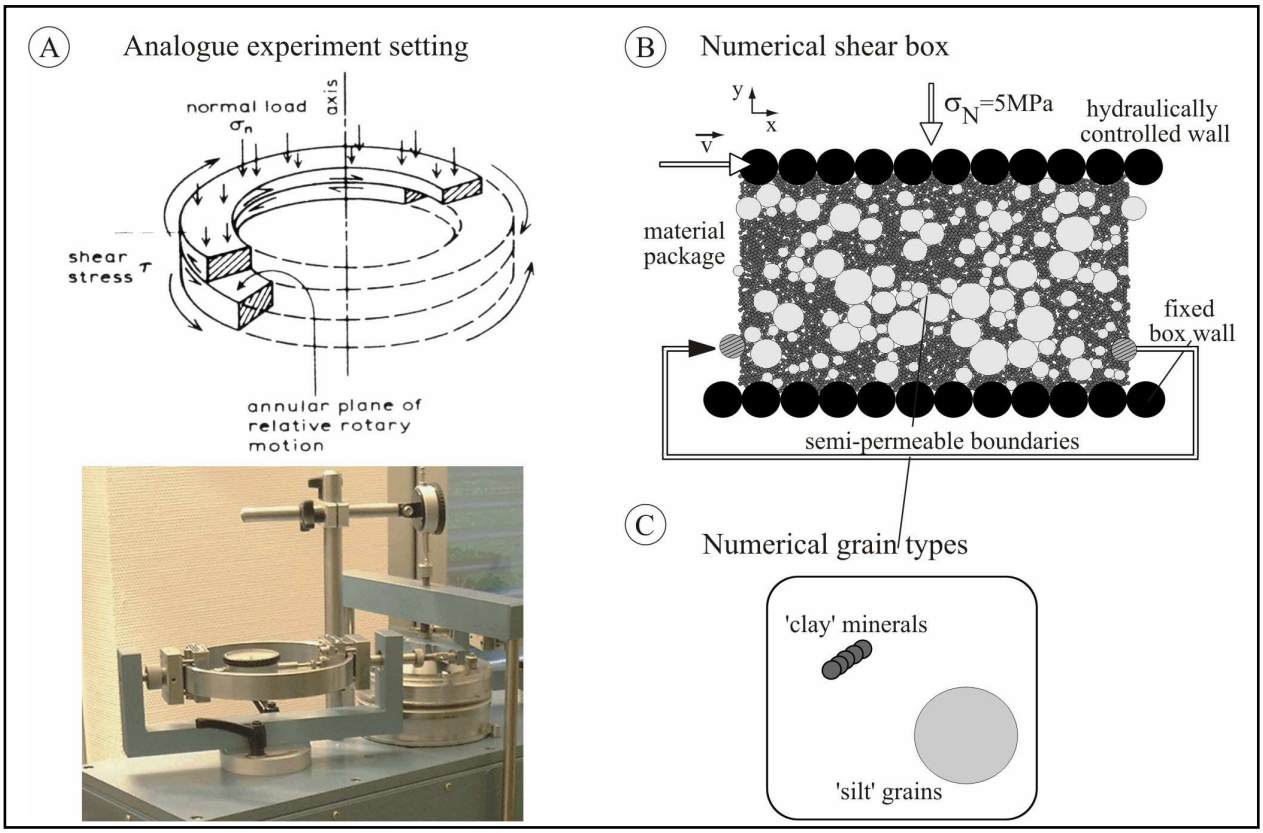

Fig. 1 Experimental configurations of (A) analogue ring shear test and (B) numerical shear box models. (C) shows the two general types of 'sediment' grains – ideal spherical 'silt' particles and tabular 'clay' minerals.

2.2 Numerical shear box experiments

We use the commercial DEM code PFC (Particle Flow Code, Itasca Consulting Group, Itasca, 2004) to build a numerical shear box model in accordance with analogue shear box experiments.

2.2.1 Theoretical background of the Discrete Element Method:

The DEM is based on a granular model approach. Materials are built up by an assemblage of spherical particles, e.g. discs, spheres, or cylinders, which interact at common contact points in accordance with simple physical contact laws (e.g., Burbridge and Braun, 2002; Cundall and Strack, 1979; Mora and Place, 1998; Morgan, 1999). In the case of elastic-frictional contact laws, particles deform elastically under a defined load at a contact point generating a repulsive normal force (F_N) perpendicular to their contact plane. This normal force can be calculated from the particle normal stiffness value (k_N) and the magnitude of elastic deformation which is estimated from the amount of particle overlapping (Cundall and Hart, 1989; Cundall and Strack, 1979; Mindlin and Deresiewics, 1953; Morgan and Boettcher, 1999). This concept applies to shear forces (F_S) as well. FS increases until it exceeds the critical shear force (F_{Smax})

(1) $$F_{S\,max} = C + \mu\sigma_N$$

which leads to frictional sliding. In this case, slip along the contact occurs and F_S drops. σ_N defines acting normal force, C the cohesion, and μ the coefficient of friction for each single particle. The progressive breaking of contacts along discrete planes reproduces fracture and fault propagation (Strayer and Suppe, 2002). The critical shear force leading to faulting is analogous to the critical shear stress that governs material strength (τ_{crit}) through the Mohr-Coulomb criterion (2) $$\tau_{crit} = C + \mu\sigma_N$$

in natural systems (e.g. Morgan and Boettcher, 1999). At the end of each time step, summation of all inter-particle contact forces (F_N) acting on a single particle enables the calculation of particle acceleration and thereby the new position of this particle using the 2. Newtonian equation of motion (Cundall and Strack, 1979).

As a consequence of the particle approach, material properties are attributed to each individual particle (μ_P) determining particle-particle interactions (Cundall and Strack, 1979). Hence, macro-properties of a material package, e.g. "overall" coefficient of friction of a particle assemblage (μ), have to be calculated from shear box experiments (e.g. Morgan,

1999). As we used cohesionless, elastico-frictional particles (C=0), the strength of the numerical assemblage is defined primarily by the coefficient of particle friction.

In addition, we implemented 'electro-static' forces as a function of particle distance to simulate interactions between 'clay' minerals equivalent to their geochemical or mineralogical behaviour in nature (e.g., Matthes, 1983). These 'electro-static' or so-called *van der Waals* forces are proportional to:

$$(3) \qquad \sim \frac{1}{r^6}$$

where r is the distance between the concerned particles (e.g. Gerthsen et al., 1982). As these 'electro-static' forces decrease with the power of 6 with particle distance they are relatively weak compared to frictional forces (e.g. Aplin et al., 1999; Chen and Anandarajah, 1996). In addition, *van der Waals* forces can be approximated from the particle size if diameters are large compared to the distance between linked particles (Amahdi, 2004). Therefore, we calculate 'electro-static' forces only at direct contact points particularly between 'clay' minerals where particles interact. In this case, inter-particle bonds are generated (e.g. Itasca, 2004) which transmit *van der Waals* forces and moments between concerned 'clay' particles. These bonds break up in accordance with the Mohr-Coulomb brittle criteria if the critical contact force is reached. As we are using only one type of 'clay' particles up to now, the shear as well as normal forces are $F_{N,S\text{-}bond}=1e^8$ N for these bonds. Simultaneously, normal and shear stiffness of these bonds are given as $K_{N,S\text{-}bond}=1e^8$ N/m^2 .

2.2.2 Model configuration:

We developed a numerical shear box in accordance with analogue experiments which mirrors a 2d cross section to the 3d ring shear apparatus (Fig. 1b). Our model consisted of a fixed bottom wall and a free upper wall. Both are built of equal-sized discs with a diameter of 0.02mm which were fixed relative to each other. The total length of this box was 0.2mm with a mean height of 0.14mm. Approximately 5000 particles depending on the 'sediment' composition were generated randomly within the shear box to create a heterogeneous material layer. Afterwards this particle assemblage was compacted due to a constant downward movement of the upper wall. As the main aim of this project was to investigate deformation processes at basal shear zones of slides the upper wall was hydraulically operated to provide a constant normal stress (σ_N) of 5MPa during the whole experiment run.

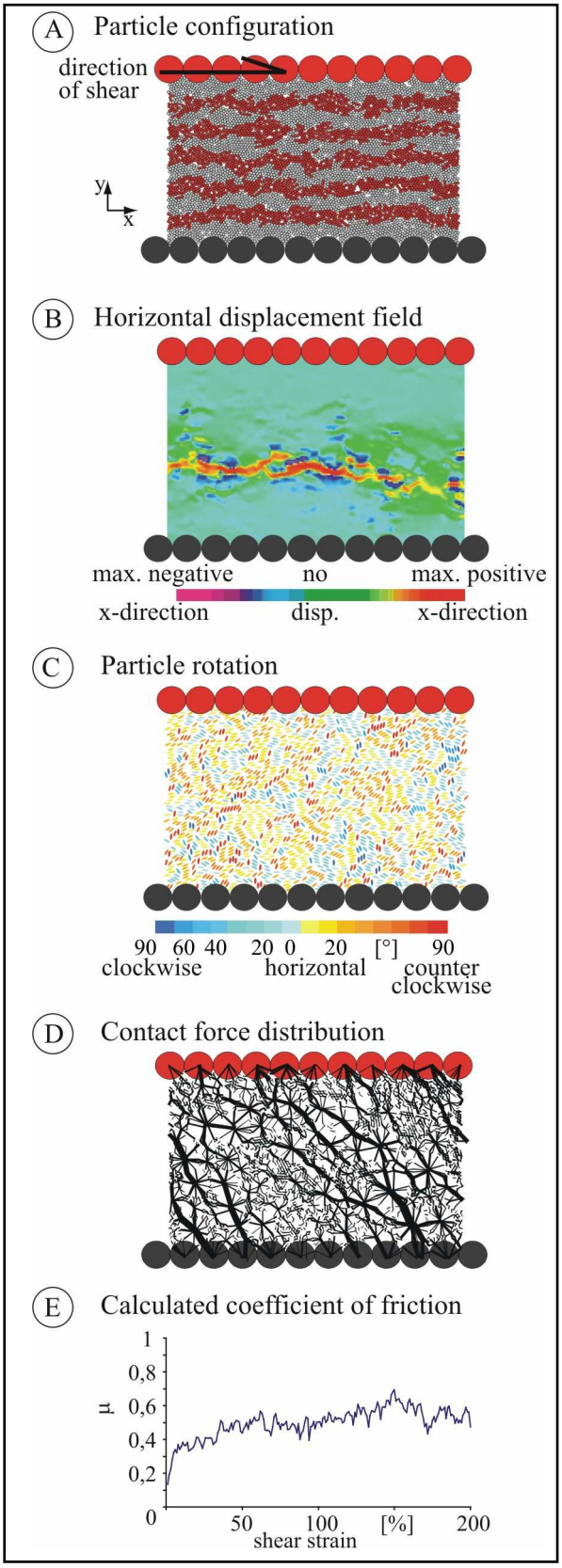

Fig. 2 Four types of experimental analyses (A) – (D) are displayed from different model runs showing typical features. Evolution of coefficient of friction can be calculated from observed force and stresses (E).

Shearing was induced by moving the upper wall with a constant velocity in positive x-direction (Fig. 1b). In addition, we defined semi-permeable boundaries at both sidewalls of the box. Here, particles could leave the shear cell through the right wall and turn back into the cell exactly at the same depth position on the left border. An 'artificial twin-grain' has to be simulated on the left hand side as long as the original particle exists on the right boundary column of the cell (Fig. 1b). For this reason, the outer three particles at both sides are not taken into account for interpretation to eliminate boundary effects. This model configuration enabled the calculation of large strain rates equivalent to the deformation rates that can be reached with analogue ring shear tests.

In this type of simulation particle fracture was not allowed. In addition, fluids are not taken into account. Restrictions based on these model assumptions will be discussed below.

As one aim of this project was to investigate the influence of material composition or texture on the shear strength of sediments, two types of grain were used: ideal spheres and elliptically shaped particles (Fig. 1c). Ideal spherical grains with diameters of 0.0056mm - 0.02mm and a log normal distribution with a peak at 0.01mm were used to simulate fine to medium 'silts' according to natural systems

(e.g. Füchtbauer, 1988; Leeder, 1999). Besides, five spherical particles with diameters of 0.002mm were combined to create tabular elliptical particles with an eccentricity of 0.33 to simulate 'clay'-shaped grains (Fig. 1c). Up to now, we used only one type of elliptical particle which corresponds to the upper limit of clay size distribution in natural systems (e.g. Füchtbauer, 1988). An implementation of further eccentricities and/or particle sizes to simulate different types of 'clay' minerals would require an exponential increase of computer calculation time. However, the major aim of these first experiments is to study the general influence of material composition on the shear strength of 'sediments'.

Density of 2100kg/m^3 and a shear and normal stiffness of $k_{N,S}$=1e^9 N/m^2 were used for all particles which has been successfully utilized to simulate deformation behaviour of marine sediments (e.g. Huhn, 2001; Zhou et al., 2002). Coefficient of friction for 'clay' particles was defined as μ_P=0.1 and for the 'silt' fraction we used μ_P=0.6 as experimentally determined from natural materials (e.g. Kopf and Brown, 2003; Lohrmann et al., 2003). In addition, an experiment with μ_P=0.2 for 'silts' was carried out to enable an identification of influences of the particle shape for the friction coefficient of the material package. The time step increment and the displacement increment per time step were defined by the software itself such that a disturbance of a given particle only propagates to its immediate neighbours.

2.2.3 Model analysis:

We first identified the location of potential thrusts and shear planes from the relative displacements of coloured marker layers in imitation of analyses of analogue sandbox experiments (e.g. Mulugetta, 1988; Fig. 2a). Simultaneously, relative particle displacements in the x-direction were measured in increments of 0.1% shear strain. Based on these data, the horizontal displacement field was calculated within the entire shear cell for each strain increment using the processing, gridding, and mapping algorithms by GMT (Wessel and Smith, 1991; Fig. 2b). The displacement gradient enables identification of areas of high and low relative particle movement to identify the position of localized deformation or the location of shear zones, respectively. In addition, information about the sense of shear can be extracted from these data (Fig. 2b). In the same way total horizontal displacement field over 200% strain can be calculated by comparing the initial particle configuration with the final situation (see below). Particle rotation can be calculated during the experiment which in particular supplies information about the grain behaviour in the immediate neighbourhood of

a shear zone (Fig. 2c). Contact forces can be visualised as bars connecting the involved couple of particles where bar thickness scales with the force magnitudes (Fig. 2d).

$$(4) \qquad \sigma_{ij} = \left(\frac{1-n}{\sum_{N_P} V_P} \right) \sum_{N_P} \sigma_{ij}^{(P)} V_P \,,$$

where $\sigma_{ij}^{(P)}$ gives the stress tensors for a single grain, V_P is the particle volume, N_P is the particle number, and n defines the porosity in between the shear cell. μ was then calculated with

$$(5) \qquad \mu = \frac{\tau}{\sigma_N},$$

where σ_N is the normal stress and $\tau = \sigma_{12}$ defines the horizontal shear stress component of the stress tensor.

The complete analytical routine was carried out for each experiment each 0.1% strain to obtain comparable results. However, we show only selected parameters to monitor typical features which are fundamental for our discussion.

3 Experimental results and observations

3.1 Geotechnical shear tests and SEM observations

3.1.1 Results from laboratory shear experiments:

Both ring shear tests and direct shear tests were carried out on dry samples, humid samples, and water-saturated samples. The results differ significantly, as can be seen in Figure 3.

Direct shear tests have been carried out at variable normal stresses as two series of experiments. First, tests at different humidities have been performed at 10, 20, and 30 MPa for illite. Second, water-saturated direct shear tests at 5-40 MPa were carried out for illite as well as for other minerals (smectite, kaolinite, quartz), which are shown together with the ring shear data as a function of normal load (Fig. 3b). During the tests, the clay-dominated samples predominantly show a generally well developed peak and subsequent lower residual shear strength profile (i.e. strain weakening behaviour). The pure clay mineral standards show a gentle increase within the μ range up to 30 MPa. Smectite remains low (μ of 0.11 at 10, 20, and 30 MPa), while illite and chlorite increased more significantly to values near μ=0.26-0.27 at 30 MPa (Figs. 3b and 4). The strain weakening behaviour is seen in the full test protocol of a direct shear experiment on illite clay (Fig. 4, inset). It can also be seen from the main panel

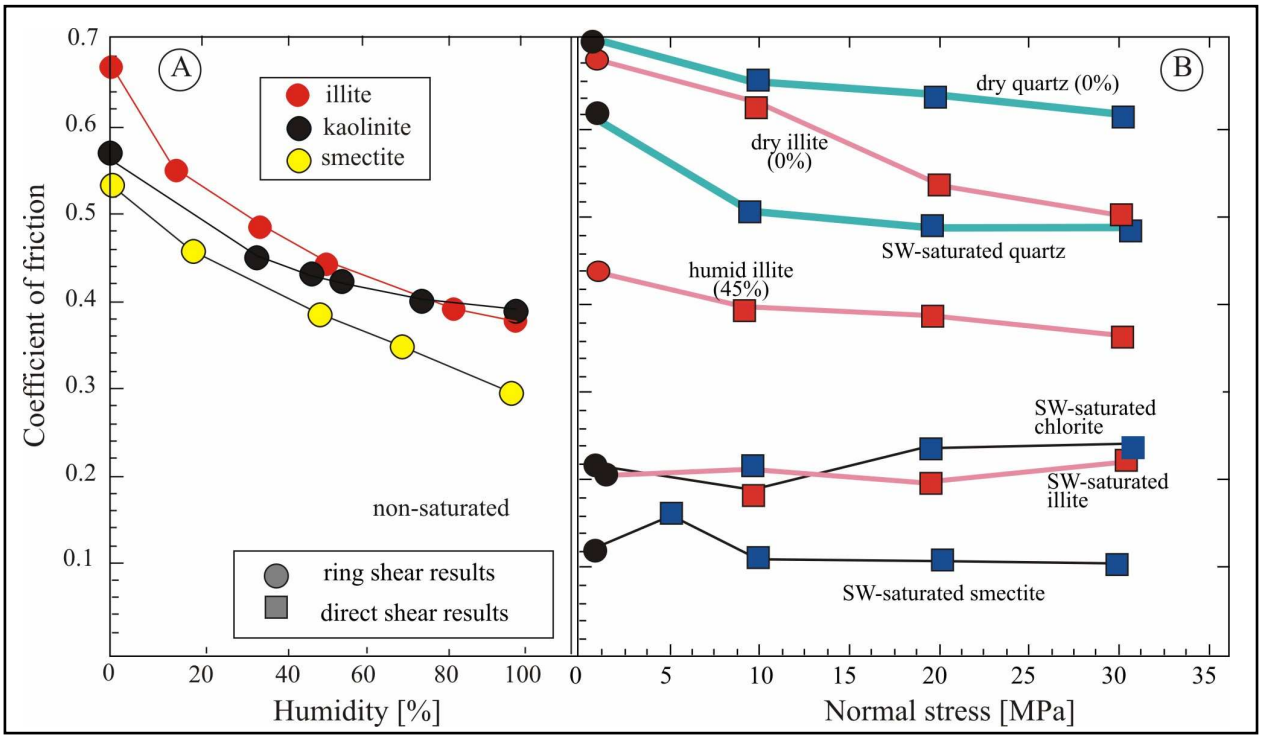

Fig. 3 (A) Coefficient of friction of different clay mineral powders at 1 MPa normal stress, plotted versus humidity (in % water content in the air prior to loading the sample into the shear apparatus). (B) Friction coefficient of different mineral standards versus normal stress of different specimen. Please note that water saturation (SW) is variable for the different curves (dry = 0%, humid = 45%, SW = fully saturated in aqueous fluid).

that pore pressure changes occur upon rapid changes in shear rate at undrained conditions and shear enhanced compaction of the specimen. In contrast to the clay minerals, quartz shows strain hardening behaviour, but a decrease with increasing normal stress to values of μ=0.48 to 0.5 (Fig. 3b).

Both data sets (i.e. Figs. 3a and 3b) indicate that dry clay mineral powders have significantly higher friction coefficients than their humid counterparts. While for quartz, μ drops only slightly, for the various

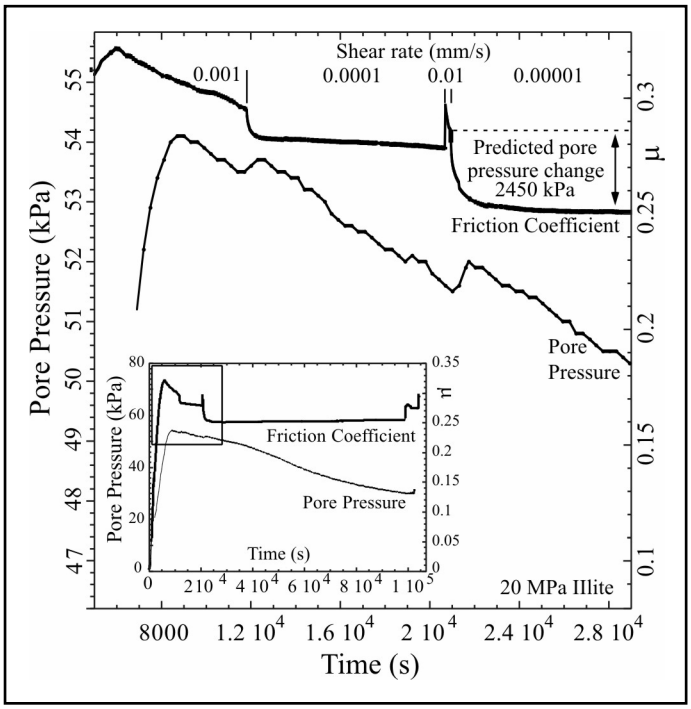

Fig. 4 Protocol of direct shear experiment of saturated illite at 20 MPa normal stress, showing pore pressure (left y-axis) and friction coefficient (right y-axis) vs. time (i.e. displacement of shear box). Inset shows entire test and location of the expanded region. In order to account for the drop in frictional resistance across the 0.0001 to 0.00001mm/s-transition, the pore pressure would have to increase by 2.45 MPa (from Kopf and Brown 2003).

clay minerals, it is roughly 50% lower in humid condition than in a totally dry powder sheared after treatment in the oven. If the sample is fully saturated in seawater (SW), the values drop again by 50% in clays. If the sample is fully saturated in seawater (SW), the values drop again by 50% in clays, while those of quartz drop only by about 0.1 (see Fig. 3b). When testing mixtures of dry smectite and dry quartz, we get minor changes in μ, most likely because in the absence of water as well as air humidity, the friction coefficients of either mineral are not dissimilar and evidently very high (0.69 for qtz, 0.54 for sm; Fig. 3). Our results are illustrated in Figure 5, dropping almost gradually from the quartz endmember via μ=0.66 (70%sm), 0.58 (50%sm) and 0.55 (70%sm) towards the smectite endmember. We will return to these changes in the discussion when comparing them to DEM results.

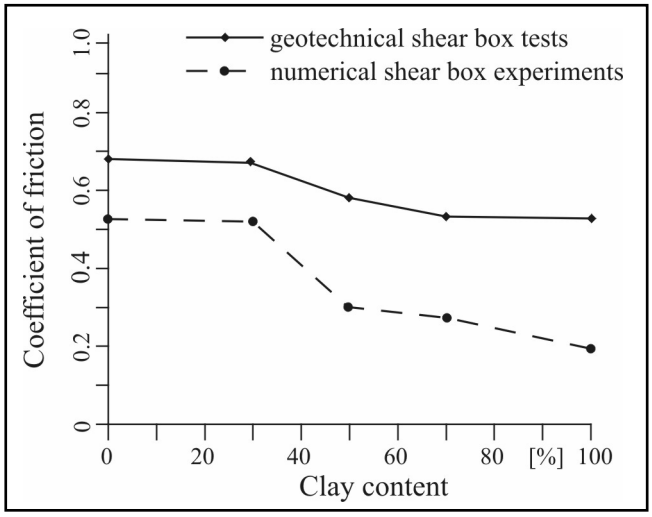

Fig. 5 Comparison of geotechnically measured (black line) and numerically calculated (dashed line) coefficients of friction as a function of sediment composition or clay concentration.

3.1.2 Results from SEM:

Fabric studies in granular mixtures of sediments reveal shear bands, slickensides, and other indicators of slip. These fabrics are most profoundly developed in the water-saturated samples, and are seen to a much lesser extent in the humid set of samples. For the fully dry samples, which were found non-cohesive at all, no deformation texture was observed. In fact, the specimens were too frail to be taken out of the annular shear cell in a non-destructive manner. No SEM study could be performed on these samples. For the ring shear samples, where specimen thickness rarely exceeds 4mm after the experiment, the shear plane is almost impossible to preserve for SEM study, even in the humid and saturated samples. Also, it is often located in the uppermost part of the sample. Hence, we were left with macroscopic study of the ring shear samples after testing. The observations indicate that completely dry clay samples are nearly white while humid ones (98%) are beige to grey (Fig. 6), with the little water adsorbed having migrated into the shear surface (Fig. 6). The remainder of the sample, usually located in the lower part of the annular shear cell, has less fluid than the shear

plane itself. We interpret this observation as a preferred transport of desorbed fluid into the pervasive shear plane.

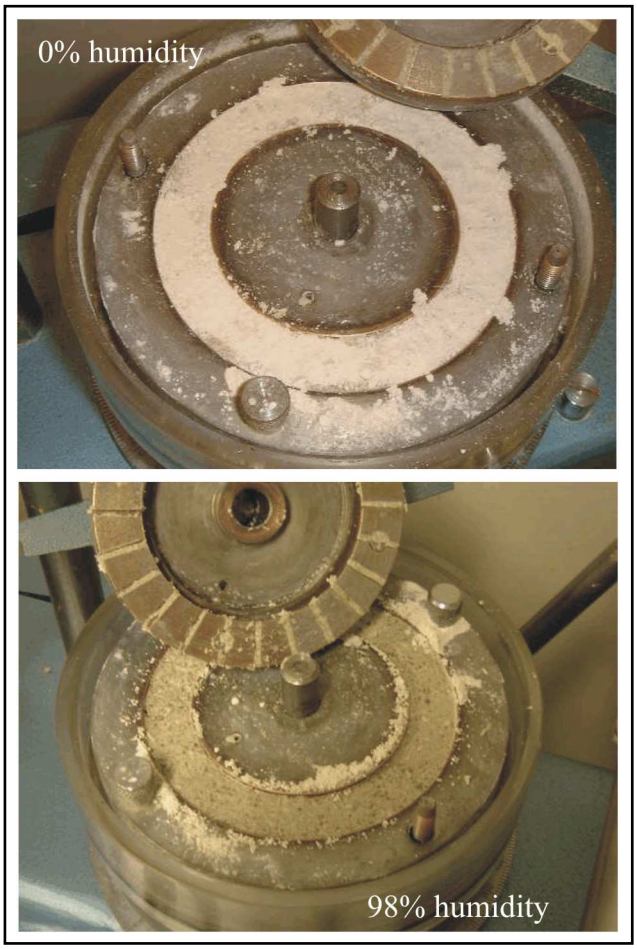

Fig. 6 Results from low stress ring shear tests of dry (upper panel) and humid (lower panel) illite; view on top of the shear surface. Please note the change to darker colours in the lower panel (98% humidity test) where water adsorbed to the clays is migrating into the shear surface.

The direct shear samples are more suitable for fabric studies because the device is capable of applying normal loads of up to 40 MPa onto the specimen. Figure 7c shows the longitudinal cross section of a specimen after an experiment at 20 MPa normal stress. Both the central (=main) shear plane and Riedel shear surfaces can be studied with the naked eye. When using the SEM, such features can also be revealed for the humid and dry samples, where displacement of individual minerals or particles is not aided by the presence of large amounts of fluid. Of course, the localization of shear to boundary and Riedel shears is characteristic for watersaturated samples as well (e.g. Moore and Lockner, 2004). Figure 7b shows two examples of dry smectite sheared at normal stresses of 10 MPa. Despite the poor fabric alignment (lower panel), thin Riedel shears can be seen. The individual micro shear zones do not exceed 10 µm in thickness.

3.1.3 Results from numerical shear box experiments:

We carried out a series of experiments to investigate the influence of material composition: beginning with a homogenous ‚silt' material which was only built up of ideal spherical particles, we increased stepwise the amount of tabular 'clay' minerals up to 100% 'clay' (Figs. 5 and 8).

In all experiments an increase in coefficient of friction was observed just after applying shear strain. At the latest after 20% shearing µ reaches the mean friction value (Fig. 8a). Such

typical strain hardening behaviour could also be identified from dry geotechnical shear tests. In contrast, a peak friction and subsequent lower residual shear strength profile monitoring a typical strain weakening behaviour similar to a saturated or at least humid sediment analogue experiment, could not be measured (Fig. 4).

The comparison of two pure 'silt' experiments with μ_P=0.6 and μ_P=0.2 revealed a mean 'overall' friction of μ=0.52 (Fig. 8a). Embedding a small amount of 'clay' fraction of approximately 30% into the 'silt sediment' did not influence the frictional strength at all ($\mu \approx 0.52$). In contrast, a further increase of 'clay' up to 50% caused a significant change in coefficient of friction. Thus, μ=0.3 was measured for mixtures of 50% 'silt' and 50% 'clay'. This trend continued while increasing the amount of 'clay'. For the shear test of 100% 'clay', the lowest coefficient of friction of μ=0.18 was calculated. These numerical results confirm observations from analogue experiments (Fig. 5).We will come back to this in the discussion.

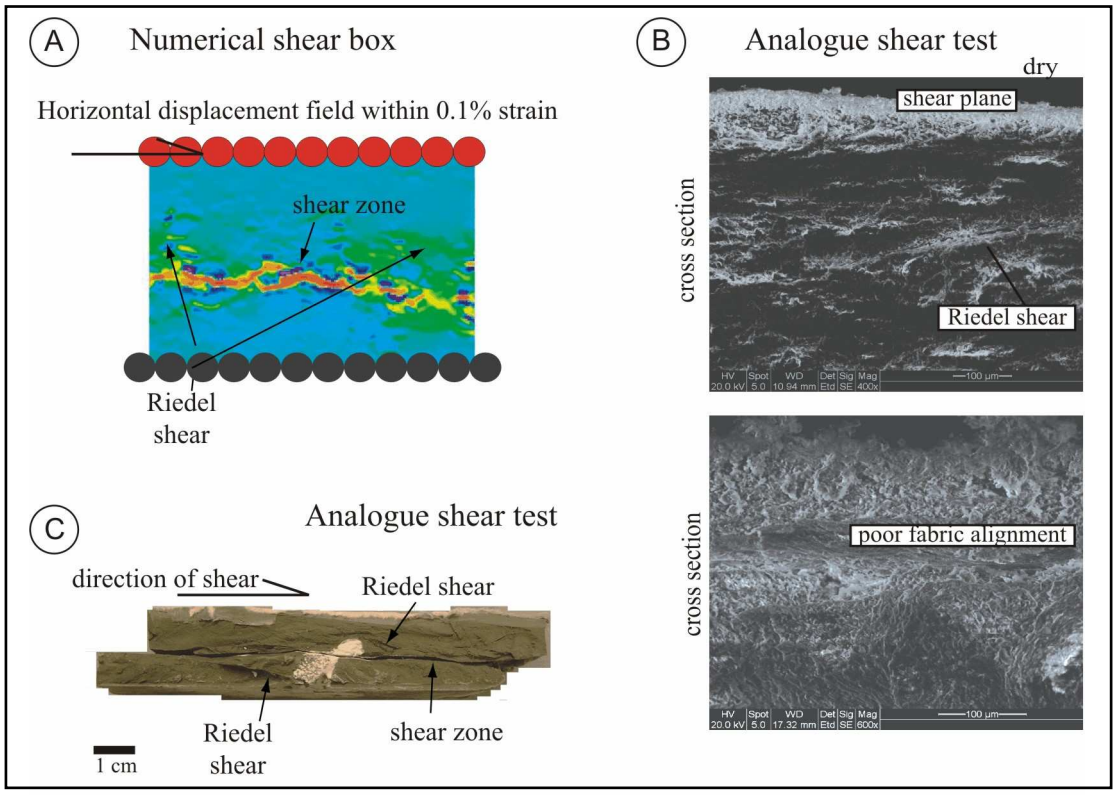

Fig. 7 Similarities between the geometry and internal structure of natural shear zones from geotechnical experiments and simulated shear zones from DEM experiments. (A) shows the horizontal displacement field within one iteration step. (B) SEM photographs of dry smectite clay sheared at 10 MPa normal load. Note the thin Riedel shear planes branching off the main shear surface in the upper portion of the picture. Fabric alignment, however, is generally poor. (C) longitudinal section through a 10 cm-long sample after a direct shear experiment. Note main shear surface as well as Riedel planes at angles of approx. 30° relative to the main plane. The white patch in the centre is artificial quartz powder used for pore pressure measurements.

Furthermore, a direct relationship between amount of 'clay' and fluctuations in friction coefficient is observed. An increase of tabular 'clay' particles caused a decrease of variations in coefficient of friction (Fig. 8a). Pure 'silt sediments' are characterized by a high fluctuation of friction during shearing whereas pure 'clays' show only small changes in friction values. Here, μ propagates fast against a mean coefficient of friction.

Investigation of the horizontal displacement fields revealed that 'sediment' composition also influences the spatial evolution and/or the geometry of shear zones (Fig. 8b, c). Thus, a shear zone thickening with a simultaneous lateral shortening could be observed in pure 'silts'. A mean shear zone thickness of approximately 0.03mm could be calculated (Fig. 8b). In contrast, 'clays' showed a localization of deformation along long narrow failure planes which extended over the entire shear cell (Fig. 8b). Here, shear zone thickness of <0.01mm could be measured. Furthermore, detailed analyses of localized deformation after 200% strain mirrored a variation of the vertical position as well as the geometry of the shear zones (Fig. 8c). In the case of pure 'silt', no distinct shear zone could be observed. Even adding a small amount of 'clay' (30%) caused a significant change in the horizontal displacement field. Here, a broad shear band evolved in the centre of the shear box. A further increase of the tabular particle fraction resulted in an upward migration of the shear zone within the shear cell except for the experiment with 70% 'clay' where the shear zone developed in the lowest part of the shear cell. Simultaneously, an increase of the amount of 'clay' caused a thinning of the shear zone. In experiments with more than 50% tabular shaped particles failure planes are localized along thin localized shear zones (Fig. 8c).

Furthermore, shear zones often coincide with tabular shaped particles in experiments with more than 50% 'clay'. From this one may conclude that tabular 'clay' particles determine the position and geometry of shear planes. The comparison of two pure 'silt' experiments with μ_P=0.2 and μ_P=0.6 indirectly allows us to assess the role of particle shape. Both models showed similar fluctuations in coefficient of friction whereas in both cases an absolute mean friction value of μ=0.52 could be measured (Fig. 8). Furthermore, both materials are characterized by an identical deformation behaviour.

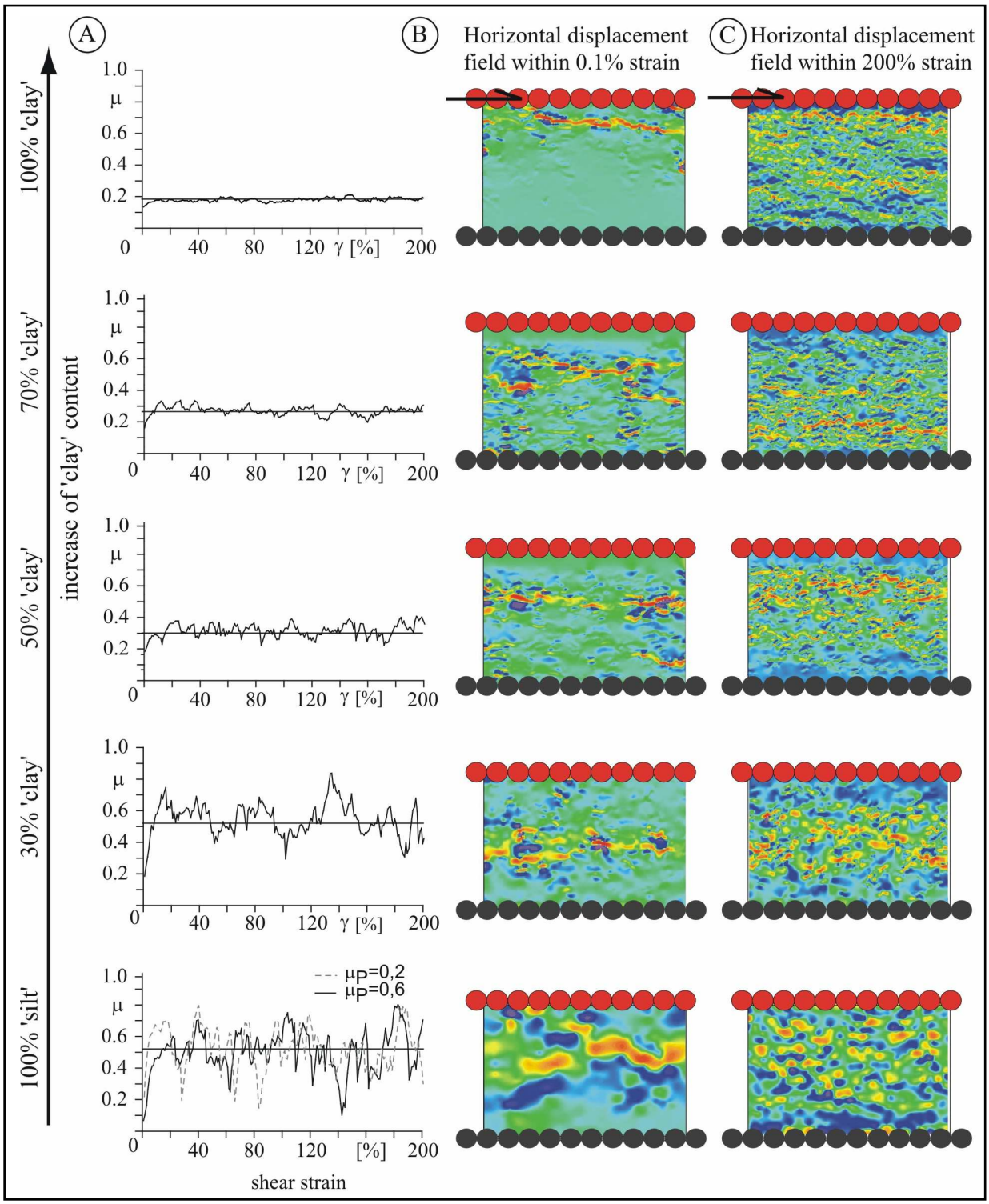

Fig 8 Experimental results of numerical shear box tests. (A) shows the calculated coefficients of friction as a function of ‘clay’ content. (B) displays examples of the horizontal displacement field of each experiment run during one iteration step or 0.1% strain respectively and equivalent (C) after 200% strain.

4 Discussion

Both experimental settings, numerical as well as analogue, supplied comparable results of coefficient of friction for dry 'sediments' under low vertical load (normal stress = 5 MPa). In all dry experiments a typical strain hardening behaviour, characterized by a slight increase in the coefficient of friction pushing towards a mean friction value, could be observed (Fig. 4, 8).

However, numerical models provided much lower coefficients of friction compared to analogue shear tests for dry material assemblages (Fig. 3, 5, 8). Furthermore, the difference between measured and simulated friction values increased with increasing clay concentration of the material package (Fig. 5). In case of pure 'clay sediments', calculated coefficient of friction is comparable to geotechnically measured values for saturated illite or smectite. Thus, tabular particles with μ_P=0.1 and an eccentricity of 0.33 seem to simulate the frictional behaviour of partly saturated clay minerals (Fig. 3;Horn and Deere, 1962; Saffer et al., 2001; Saffer and Marone, 2003) although fluids are not included in these numerical simulations. The main contrast of DEM frictional behaviour is the roughness of the particles. Similarly, geotechnical analogue work demonstrated that in addition to fluid lubricants, low mineral roughness causes an appreciate decrease in μ (see detailed discussion in Horn and Deere, 1962).

We change particle shape or particle eccentricity to raise the overall frictional strength of the material package. For instance, the overall friction strength of μ=0.52 was calculated for the pure 'silt' experiment with ideal spherical particles with μ_P=0.2. This confirms the key role of particle shape, and hence overall roughness, for the frictional strength.

Thus, both analogue shear tests as well as numerical shear box models support the hypothesis that material composition plays a key role for the frictional strength of sediments (Fig. 5). Both techniques showed a decrease in coefficient of friction with increasing amount of clay. In addition in both cases a small increase of clay content (30%) had no significant influence on the frictional strength of material packages. Only when clay concentration reaches 50% a distinct decrease of friction strength is observed (Fig. 5). These results confirm that the evolution of shear zones or failure planes is directly connected to the presence of clays. This finding is also verified by DEM experiments on a micro-scaled level where failure is localized at the position of 'clay' minerals. Furthermore, these observations support earlier work where

the presence of clay minerals has been causally connected to slope instability (e.g. for the Storegga slide off Norway; see Solheim et al., 2005).

Our two sets of experiments also show textural similarities. A narrow shear zone could be identified in the upper part of the numerical shear cell in the case of pure ‘clay’, equivalent to what was observed in the geotechnical shear tests, especially the direct shear experiments (Fig. 7a, b). In addition, both experiments display thin Riedel shear planes in ‘smectite’.
Furthermore, DEM experiments revealed a downward migration of the shear zone to lower parts of the ‘sediment’ layer with increasing ‘silt’ concentration. Simultaneously, the thickness of the shear zone increases. Such shear zone dilation was only monitored for pure ‘silt’ layers. This correlates with former numerical DEM shear box experiments on ideal spherical particles (Morgan and Boettcher, 1999).
Numerical tests also reveal a direct interaction between the position of clay minerals in the material matrix and the location of shear planes. The tabular ‘clay’ particles determined the position of localized deformation. In addition, an increase of 'clay' minerals results in smoother deformation in both experimental settings, proving the hypothesis of the dominant role of clay. Translated to slope stability issues, clay minerals appear to be the major controlling parameter for the mechanical stability of slopes and/or the possible failure of slope sediments.

As has been shown earlier (Hubbert and Rubey, 1959), geotechnical shear tests further demonstrate the key role of fluids for the frictional strength of clay sediments. An increase in humidity caused a remarkable decrease in the coefficient of friction. Here, smectite is identified as most sensitive compared to illite, which shows the lowest decrease in frictional strength (Fig. 3a). In contrast, silt is mostly unaffected by an increase of pore fluids (see also Horn and Deere, 1962). However, coefficients of friction less than $\mu=0.25$ were only measured for wet sediments from geotechnical tests. Hence, the degree of fluid saturation can be also classified as an important parameter for the destabilisation of slope materials (Fig. 3).

5 Conclusion & Outlook

Both geotechnical and numerical shear box tests reveal the mineralogy, in particular the presence of clay minerals, as the most important factor controlling the frictional stability or shear strength of sedimentary materials. Our experiments support the hypothesis that failure of slopes requires the existence of clay-rich layers with a clay content of >50% embedded in

the sediments. In addition, geotechnical tests verify influences of pore fluids which are essential to reduce the coefficient of friction of clay minerals. In contrast, silt is mostly unaffected by fluid saturation or by an increase of humidity. Thus, submarine continental slopes comprising fully saturated sediments are more in favour than their continental counterparts.

Future research aims to bring analogue and numerical shear tests closer together focuses on taking the DEM shear box into the 3rd dimension. Besides, we will implement fluids enabling investigation of influences of pore fluid saturation on the coefficient of friction and the deformational behaviour of soils.

Acknowledgements

We thank our colleagues from the Research Center Ocean Margins (RCOM) for fruitful discussions on sediment physics and material behaviour. Kevin Brown is acknowledged for sharing his laboratory at SCRIPPS Institution of Oceanography for the direct shear tests. Funding for this research has been received through Deutsche Forschungsgemeinschaft via the RCOM. This is RCOM publication RCOM0394.

Chapter VI

1 Summary

The results from the previous chapters illustrate that DEM simulations on the particle scale level do capture a wide range of features also observed in nature and laboratory: Namely localization, frictional strength, dilation and contraction. The prove that micromechanical deformation behaviour from DEM simulations is applicable to natural and laboratory conditions.

The research conducted in Chapters II-IV provide insight into complex micromechanical processes for a granular sample subject to shear. Regarding the relevance to natural conditions and comparable analogue studies, it was demonstrated that boundary surface and host rock roughness, grain shape, the stratigraphic sequence and the composition of mixed 'silt'/'clay' samples have a significant influence on deformation behaviour of soils and fault gouge. A direct comparison was undertaken in Chapter V as a proof of concept.

1.1 Conclusions

The most important insight of this thesis is that even slight changes of the aforementioned parameters control micromechanical deformation processes on the grain-scale level. The different micromechanical behaviour then leads to the variation of localization, frictional strength, dilation and contraction on the macro scale:

(1) Especially the study presented in Chapter II was successful in quantifying the influence of boundary roughness on macroscopic deformation behaviour. One of the most interesting micromechanical results is the existence of threshold values of roughness, below and above which extremely localized displacement occurs, albeit with different deformation mechanisms. In between these thresholds, deformation becomes distributed. As a result of these different deformations mechanisms, frictional strength varies significantly:

- Low roughness leads to a boundary detachment with no internal sample deformation, since no force transmission from the boundary onto the sample is active. Boundary and sample are mechanically decoupled. Friction of both sample and boundary is consequently low.
- High roughness leads to a concentrated shear zone at the boundary and internal deformation migrates into the sample. Force transmission works best in the areas adjacent to the boundary. Complete decoupling was not observed, but friction of the boundary is low while interior friction is the highest observed.

- Intermediate roughness leads to distributed deformation inside the complete sample, so the whole particle assembly can be viewed as a shear zone. Force transmission onto the sample is active; sample and boundary are completely coupled. This leads to intermediate frictional strength of the sample, but to highest friction for the boundary.

Consequences for natural, laboratory and numerical tests were already discussed in Chapter II. From these, it can be concluded that failure of weak layers is not a simple mechanism. Although the concept of weak layers is valid, failure does not necessarily occur inside these layers, but also at the boundaries. For laboratory tests that means, that a geotechnical assessment of weak layers should also include analysis of host rock properties, in this case roughness in relation to grain size distribution of sample. Failure of weak layers is most likely to occur at the boundary between a weak layer and the host rock, especially if host rock roughness is very high or very low, since frictional strength at the boundary/layer interface is lowest (for natural example see also Strasser et al., in press).

(2) The difference between microscopic deformation of approximately spherical and platy grains, i.e. silt and clay, has long been evident. The study in Chapter III therefore concentrated on grain shape parameters and their relation to deformation behaviour. Two parameters, sphericity and roughness were investigated.

As for boundary roughness, different particle sphericity and roughness lead to fundamentally different deformation mechanisms. These parameters control microfabric development and interparticle sliding, mainly by their different interlocking and rotational capability.

- Increasing roughness caused increasing particle interlocking. Microfabric breakdown is prohibited, since slip and rotation are obstructed by interlocking particles. Particles cannot rotate to preferred orientations so that friction is high and volume strain is positive.
- Increasing roughness of particles precludes shear zone development, because particle domains of similar orientation cannot evolve due to interlocking.
- Decreasing sphericity caused increasingly complex initial microfabrics. Disintegration or breakdown of such microfabrics with increasing strain is caused by particle rotation to preferred angles. These preferred angles favour low friction since slip occurs more easily.
- Increasing particle sphericity leads to increasing shear zone localization and vertical dilation.

- Although some of our numerical experiments show remarkable resemblance to analogue experiments, no particle shape could be found numerically which led to exactly the same stress-strain response as in laboratory.

Altogether, it is reasonable to conclude that the shape of 'clay' particles does have a significant influence on the mechanical strength of weak layers. In our case, however, the mechanical weakness can only be accounted for with smooth, elongated grains. Once grains become irregular and rough, shear strength increases and deformation becomes distributed. Without the ability to bend and break, grain interlocking for our numerical particles becomes the limiting mechanism by which shear strength increase works.

(3) Despite detailed microscopic studies of natural and laboratory shear zones, it remains unclear if shear is localized predominantly above, below or directly on layer boundaries. Therefore, experiments with numerical sandwich layers were conducted, where the particle coefficient of friction was varied. Two types of layered specimen were studied: (1) A 'silt'-'clay'-'silt' assemblage and (2) a 'clay'-'clay'-'clay' package.

- The particle friction contrast controls if particles slide, roll or rotate. Thus, particle friction contrast governs which deformation mode is dominant. Depending on dominant deformation mode, displacement localizes differently. Hence, localization is a complicated mechanism on the grain scale level which depends on particle friction contrast.
- Sliding of 'silt' particles is dominant over 'clay' particle sliding and rotation when particle friction contrast is negative. This situation hardly shows in nature, since particle coefficient of friction for natural silt is usually higher than for natural clay. Sliding and rotation of 'clay' particles are the dominant deformation mechanisms when particle friction contrast is positive. This results in a complete decoupling of material located on top of the shear zone.
- There are threshold levels for sliding and rotation of 'clay' particles which determine where localization occurs: If more than ~30% of contacts between particles are sliding and if more than 40% rotate to angles greater than 30°, then deformation localizes inside a layer.
- Observed localization structures showed remarkable similarity to natural sediments. Along with classical Riedel structures on the grain scale level (Y-, P- and R_1 type shear planes), some interesting correlations to scaly clays and similarities to S-C band formation

could be observed. Additionally, the ‘clay’ type material shows a distinct connection between slip planes and particle alignment.

Although the variation of the particle coefficient of friction led to values which may seem unrealistic, valuable insights into detailed micromechanical processes in a granular sample were gained. The more realistic settings consequently showed localization features and mechanical strength comparable to natural conditions. It is especially interesting to note that it is the contrast between particle friction and not the absolute particle friction of different layers which most influences localization. Deformation (localization and strength) inside a weak sediment package thus may vary greatly when grain properties change vertically and horizontally.

(4) Research on a well-established relationship validates the use of DEM simulations: the dependence of frictional strength on clay mineral fraction (Chapter I). Comparative geotechnical and numerical measurements were taken to analyze deformation behaviour of weak layers with a mixed mineralogy to emphasize the study of advantages and disadvantages of both methods. Furthermore, the possibility of combining geotechnical and numerical methods to achieve a better understanding of microscopic deformation processes was tested.

a. The presence and in particular the concentration of ‘clay’ minerals controls shear stability in both laboratory and numerical shear box tests. Thus, failure of weak layers is most likely with a ‘clay’ content > 50%.
b. Pore fluids are effective in lowering friction of clay-mineral-rich sediments; in particular if clay mineralogy is different. For example, illite requires a larger degree of fluid saturation to reach as low a friction as smectite. Here, laboratory tests are significantly advantageous over numerical simulations, which in our cases do not account for fluids.
c. The influence of parameters controlling frictional strength can be classified by combining laboratory and numerical experiments.
d. Shear plane monitoring is difficult to mirror in laboratory tests, while the DEM allows a direct monitoring of the shear localization in all materials.

1.2 Synthesis

A major goal of this study was to shed light on the question why destabilization and failure occurs, when other parts of - for example a submarine slope - remain stable. Therefore, the target of this study was not only the analysis of parameters which influence deformation, but

also to establish a ranking order, or quantification. Within the limits of the numerical model, this is possible. Thus, the following order is based on conclusions from numerical models alone, and the transition to natural conditions has to be made carefully.

From a purely numerical point of view, two first order influences on deformation are certainly grain roughness and particle friction contrast. The difference of mechanical strength and localization features between smooth and rough grains is enormous (Chapter III): (1) A complete sign inversion from negative to positive occurs for volume change and porosity. (2) Average friction increases roughly by a factor of 6. (3) Displacement undergoes transition from localized to distributed. (4) Rotation and microfabric development change from abundant to non-existent. Similarly, if particle friction contrast changes from negative to positive (Chapter IV): (1) Localization features completely switch to other layers. (2) Macroscopic frictional strength begins to converge or diverge. (3) Other micromechanical parameters also converge or diverge when the turning point of zero particle friction contrast is approached.

In contrast to that, the change of grain sphericity, boundary roughness and 'clay' mineral fraction only leads to a gradual change of deformation behaviour. For example, the decrease of grain sphericity leads to gradually enhanced localization and increasingly negative volume strain (Chapter III).

Therefore, it can be argued that grain roughness and particle friction contrast exhibit more influence on deformation compared to grain sphericity, boundary roughness and 'clay' mineral fraction. However, it is necessary to scale this ranking to natural conditions is necessary. Since modelling grain breakage and grain bending has not been taken into account in this study, interlocking rough grains were not able to break. If this were be the case, the influence of grain roughness would decrease. Furthermore, for particle friction contrast models, there exist some cases which are hardly realized in nature: Particle friction for 'silt' is seldom lower than for 'clay'. So when only natural circumstances are taken into account (particle friction is positive for the 'clay' layer sandwiched between 'silt' layers), a slightly different ranking ensues:

Without grain breakage, influence of grain roughness is difficult to rank. Since the models operated under relatively low stress conditions, where grain breakage should be minimal (see Chapter I), I would surmise that roughness would still be a first order influence even with

grain breakage. However, under a higher stress regime where grain breakage would be abundant, this influence would become smaller.

'Clay' mineral fraction has a great impact on deformation. Although changes are only gradual when 'clay' fraction increases, these are very systematic. Frictional strength increases from 0.2 to 0.5 and localization features change significantly from distributed, wide shear planes to a narrow localized shear zone.

The influence of boundary roughness is slightly smaller, but still shows a very systematic relationship to internal friction (which increased from 0.2 to 0.6). Localization also changes with increasing roughness, but altogether the influence of boundary roughness is smaller than for 'clay' mineral fraction.

In our simulations the influence of grain sphericity is relatively small: Frictional strength is almost the same for the three different sphericities: Volume strain, porosity, localization, rotation and domain evolution are only slightly enhanced with decreasing sphericity.

The influence of sediment layering is difficult to place into this ranking. For a sandwiched 'clay' layer, deformation always localizes in the 'clay' under realistic conditions. For experiment (2) in Chapter IV, where one 'clay' layer is sandwiched by two other 'clay' layers with only slightly different particle properties, particle friction contrast has a great influence on frictional strength and localization. Here, particle friction contrast possibly results even from very low differences in surface properties. In these cases, the sign inversion still has a high impact on deformation and frictional strength (see Chapter IV).

The previous paragraphs and chapters show that the process of rock failure is a complex and complicated mechanism, even on a microscopic scale and with the simplifications of a numerical model. The ranking presented above sheds some light on this process and thus can help to answer the question why failure occurs at some places while others remain stable. It was not possible to test all parameters and there still remain many unanswered questions.

1.3 Outlook

Future work should directly take up where the previous studies left off. It should concentrate on two main objectives: (1) Continuation to quantify parameters not previously investigated, and (2) extension of the model to reduce its limitations.

(1) The relation between normal stress and frictional strength, which has been observed for other numerical models and analogue shear tests (Chapter I), could not be quantified in our models. It would be interesting to study the effect of increasing normal stress on

micromechanical deformation processes. It may be conceivable that for example the rotation of single ‘clay’ particles and the development of ‘clay’ microfabric are significantly altered. This would lead to highly different localization features on the grain scale level and also to variations of dilation and contraction of the evolving shear zone.

In our models, grain fracture of sample and boundary particles has not been studied. For fault gouge, it is known that grain fracture and the associated change of grain size distribution significantly influences deformation (Chapter I). For the spherical ‘silt’ particles, integration of particle fracture is not possible. For the ‘clay’ particles on the other hand, incorporating of grain fracture is desirable and possible. The subsequent reduction of grain size would possibly decrease void ratio and enhance stable sliding. As an in-between step, ‘clay’ particle bending might be introduced.

The study of deformation history of numerical samples would also be interesting. It may be important to analyze if a healing effect, which can often be observed for natural materials when deformation is on hold, can also be observed in numerical specimen. It might be possible that, once the outer shear stress is zero, some particles are still able to move a little bit into voids. Thereby, contact networks could be reset and reactivation of shear could lead to stick-slip behaviour. This would also provide an opportunity to study rate- and state-dependent friction laws on the grain-scale level.

(2) A necessary step is the implementation of our models into 3-D. Other authors have observed that comparability to natural samples is enhanced when simulations were conducted in 3-D (Hazzard and Mair, 2003, Chapter I). This would offer the possibility of introducing more realistic ‘clay’ particle geometries, instead of the simple tabular shape. The goal here would be to realize a geometry closer to natural grains. Furthermore, parameters such as a realistic porosity and permeability could be simulated.

To further deepen our understanding of granular shear, fluids must be implemented at some point. Despite the obvious effect of reduction of normal stress to effective stress, more important features such as excess pore pressure evolution could then be studied. For failure processes, it might be particularly interesting if a sudden increase in hydrostatic pressure would result in any change of excess pore pressure amount or distribution, a topic still much debated in the community.

Furthermore, implementation of all physical processes related to cohesion is desired. That this is possible has already been demonstrated (Chapter I). Cohesion would considerably influence

peak strengths of materials, compaction development and the evolution of an initial microfabric during sedimentation.

References

Abe, S., Dieterich, J.H., Mora, P. and Place, D., 2002. Simulation of the Influence of Rate- and State-dependent Friction on the Macroscopic Behaviour of Complex Fault Zones with the Lattice Solid Model. Pure and Applied Geophysics, 159: 1967 - 1983.

Abe, S. and Mair, K., 2005. Grain fracture in 3D numerical simulations of granular shear. Geophysical Research Letters, 32(L05305): doi:10.1029/2004GL022123.

Aharonov, E. and Sparks, D., 2004. Stick-slip motion in granular layers. Journal of Geophysical Research, 109(B09306): doi:10.1029/2003JB002597.

Amahdi, G., 2004. London-van der Waals surface energy between particles. Lecture, http://www.clarkson.edu/fluidflow/courses/me637/5_vanderWaals.pdf.

Amontons, G., 1699. Mémoires de l'Académie Royale A. 257-282.

Anandarajah, A., 1994. Discrete Element Method for simulating behaviour of cohesive soil. Journal of Geotechnical Engineering, 120(9): 1593 - 1613.

Anandarajah, A., 1997. Influence of Particle Orientation on One-Dimensional Compression of Montmorillonite. Journal of Colloid and Interface Science, 194: 44 - 52.

Anandarajah, A., 1999. Multiple time-stepping scheme for the discrete element analysis of colloidal particles. Powder Technology, 106(2): 132-141.

Anandarajah, A. and Lavoie, D., 2002. Numerical simulation of the microstructure and compression behaviour of Eckernförde Bay sediments. Marine Geology, 182(1-2): 3-27.

Anthony, J.L. and Marone, C., 2005. Influence of particle characteristics on granular friction. Journal of Geophysical Research, 110(B08409): doi:10.1029/2004JB003399.

Antonellini, M.A. and Pollard, D.D., 1995. Distinct element modelling of deformation bands in sandstone. Journal of Structural Geology, 17(8): 1165-1182.

Aplin, A.C., Fleet, A.J. and Macquaker, J.H.S., 1999. Muds and Mudstones: Fluid-Flow Properties. Geological Society of London, Special Publications, 158: 45-60.

Ask, M.V.S. and Kopf, A., 2004. Constraints on the state of in situ effective stress and the mechanical behaviour of ODP Leg 186 claystones in the Japan Trench forearc. The Island Arc, 13(1): 242-257.

Aydin, A., Borja, R.I. and Eichhubl, P., 2006. Geological and mathematical framework for failure modes in granular rock. Journal of Structural Geology, 28(10.1016/j.jsg.2005.07.008): 83-98.

Beeler, N.M., Tullis, T.E., Blanpied, M.L. and Weeks, J.D., 1996. Frictional behaviour of large displacement experimental faults. Journal of Geophysical Research, 101(B4): 8697-8715.

Bennett, R.H., Bryant, W.R. and Hulbert, M.H. (Editors), 1991b. Microstructure of Fine-Grained Sediments. Frontiers in Sedimentology. Springer-Verlag, New York, 582 pp.

Bennett, R.H., O'Brien, N.R. and Hulbert, M.H., 1991a. Determinants of Clay and Shale Microfabric Signatures: Processes and Mechanisms. In: R.H. Bennett, Bryant, W. R., Hulbert, M. H. (Editor), Microstructure of Fine-Grained Sediments. Frontiers in Sedimentology. Springer-Verlag, New York, pp. 582.

Berthe, D., Choukroune, P. and Jegouzo, P., 1979. Orthogneiss, mylonite and non-coaxial deformation of granites: The example of the South-American shear zone. Journal of Structural Geology, 1(31-42).

Biegel, R.L., Sammis, C.G. and Dieterich, J.H., 1989. The frictional properties of a simulated fault gouge having a fractal particle size distribution. Journal of Structural Geology, 11(7): 827 - 846.

Biegel, R.L., Wang, W., Scholz, C.H. and Boitnott, G.N., 1992. Micromechanics of Rock Friction 1. Effects of Surface Roughness on Initial Friction and Slip Hardening in Westerly Granite. Journal of Geophysical Research, 97(B6): 8951-8964.

Bishop, A.W., Green, G.E., Garga, V.K., Andresen, A. and Brown, J.D., 1971. A new ring shear apparatus and its application to teh measurement of residual strength. Géotechnique, 21(4): 273-328.

Blenkinsop, T.G., 1991. Cataclasis and Process of Particle Size Reduction. Pure and Applied Geophysics, 136(1): 59-86.

Bos, B., Peach, C.J. and Spiers, C.J., 2000. Frictional-viscous flow of simulated fault gouge caused by the combined effects of phyllosilicates and pressure solution. Tectonophysics, 327(3-4): 173-194.

Bowden, F.P. and Tabor, D., 1950. The friction and lubrication of Solids Part 1. Oxford University Press, London.

Bowden, F.P. and Tabor, D., 1964. The friction and lubrication of solids Part II. Oxford University Press, London.

Brace, W.F. and Byerlee, J.D., 1966. Stick-slip as a mechanism for earthquakes. Science, 153: 990-992.

Burbridge, D.R. and Braun, J., 2002. Numerical models of the evolution of accretionary wedges and fold-and-thrust belts using the distinct element method. Geophysical Journal International, 148: 542 - 561.

Byerlee, J.D., 1978. Friction of Rocks. Pure and Applied Geophysics, 116: 615 - 625.

Campbell, C.S., Cleary, P.W. and Hopkins, M., 1995. Large-scale landslide simulations: Global deformation, velocities and basal friction. Journal of Geophysical Research, 100(B5): 8267-8283.

Canals, M. et al., 2004. Slope failure dynamics and impacts from seafloor and shallow sub-seafloor geophysical data: case studies from the COSTA project. Marine Geology, 213: 9-72.

Chambon, G., Schmittbuhl, J. and Corfdir, A., 2006. Frictional response of a thick gouge sample: 1. Mechanical measurements and microstructures. Journal of Geophysical Research, 111(B09308): doi:10.1029/2003JB002731.

Chen, J. and Anandarajah, A., 1996. Van der Waals Attraction between Spherical Particles. Journal of Colloid and Interface Science, 180: 519 - 523.

Cheng, Y.P., Bolton, M.D. and Nakata, Y., 2004. Crushing and plastic deformation of soils simulated using DEM. Geotechnique, 54(2): 131 - 141.

Cloos, M. and Shreve, R.L., 1988. Subduction-Channel Model of Accretion, Melange Formation, Sediment Subduction, and Subduction Erosion at Convergent Plate Margins: 1. Background and Description, 2. Implications and Discussion. Pure and Applied Geophysics, 128(3-4).

Coulomb, C.A., 1785. Theorie des machines simples, en ayant egard au frottement de leurs parties, et la roideur des cordages. Mem. Math. Phys. Paris: 161 - 342.

Cundall, P.A., 1987. Distinct Element Models of Rock and Soil Structure. In: E.T. Brown (Editor), Analytical and Computational Methods in engineering Rock Mechanics. Allen and Unwin, London.

Cundall, P.A., 1989. Numerical experiments on localization in frictional materials. Ingenieur-Archiv, 59: 148-159.

Cundall, P.A. and Hart, R.D., 1989. Numerical Modeling of Discontinua. In: G.G.W. Mustoe, M. Henriksen and H.-P. Huttelmaier (Editors), Proceedings, 1st U.S. Conference on Discrete Element Method. CSM Press.

Cundall, P.A. and Strack, O.D.L., 1978. BALL - A program to model granular media using the distinct element method, Technical Note, Advanced Technology Group. Dames and Moore, London.

Cundall, P.A. and Strack, O.D.L., 1979. A discrete numerical model for granular assemblies. Géotechnique, 29(1): 47-65.

Cundall, P.A. and Strack, O.D.L., 1983. Modeling of microscopic mechanisms in granular material. In: J.T. Jenkins, Satake, M. (Editor), Mechanics of Granular Materials: New Models and Constitutive Relations. Elsevier Science Publishers B.V., Amsterdam.

Dahlen, F.A., 1984. Noncohesive Critical Coulomb Wedges: An Exact Solution. Journal of Geophysical Research, 89(B12): 10125-10133.

Dieterich, J.H., 1981. Constitutive Properties of Faults with Simulated Gouge. In: N.L. Carter, M. Friedman, J.M. Logan and D.W. Stearns (Editors), Mechanical Behaviour of Crustal Rocks The Handin Volume. Geophysical Monograph Series. AGU, Washington, D.C., pp. 103 - 120.

Dieterich, J.H. and Conrad, G., 1984. Effect of humidity on time- and velocity-dependent friction in rocks. Journal of Geophysical Research, B89: 4196 - 4202.

Djéran-Maigre, I., Tessier, D., Grunberger, D., Velde, B. and Vasseur, G., 1998. Evolution of microstructures and of macroscopic properties of some clays during experimental compaction. Marine and Petroleum Geology, 15(2): 109-128.

Füchtbauer, H. (Editor), 1988. Sedimente- und Sedimentgesteine. E.Schweizbart'sche Verlagsbuchhandlung, Stuttgart, 1141 pp.

Gao, J. et al., 2004. Frictional Forces and Amontons' Law: From the Molecular to the Macroscopic Scale. Journal of Physical Chemistry B, 108: 3410 - 3425.

Gerthsen, C., Kneser, H.O. and Vogel, H., 1982. Physik. Springer Verlag, Berlin.

Gu, Y. and Wong, T.-F., 1994. Development of Shear Localization in Simulated Quartz Gouge: Effect of Cumulative Slip and Gouge Particle Size. Pure and Applied Geophysics, 143(1/2/3): 387-423.

Guo, Y. and Morgan, J.K., 2004. Influence of normal stress and grain shape on granular friction: Results of discrete element simulations. Journal of Geophysical Research, 109(B12305): doi10.1029/2004JB003044.

Hampton, M.A. et al., 1978. Quantitative study of slope instability in the Gulf of Alaska., Offshore Technology Conference, pp. 2307-2318.

Hampton, M.A., Lee, H.J. and Locat, J., 1996. Submarine landslides. Reviews of Geophysics, 34(1): 33-59.

Hatzor, Y.H. and Levin, M., 1997. The shear strength of clay-filled bedding planes in limestones - back-analysis of a slope failure in a phosphate mine, Israel. Geotechnical and Geological Engineering, 15: 263-282.

Hazzard, J.F. and Mair, K., 2003. The importance of the third dimension in granular shear. Geophysical Research Letters, 30(13): 1708, doi:10.1029/2003GL017534.

Heiling, D., 1988. Ton- und Siltsteine. In: H. Füchtbauer (Editor), Sedimente und Sedimentgesteine. E. Schweizbart'sche Verlagsbuchhandlung, Stuttgart, pp. 1141.

Hiltmann, W. and Stribrny, B., 1998. Tonmineralogie und Bodenphysik. Handbuch zur Erkundung des Untergrundes von Deponien und Altlasten, 5. Springer-Verlag, Berlin, 297 pp.

Horn, H.M. and Deere, D.U., 1962. Frictional chracteristics of minerals. Geotechnique, 12: 319 - 335.

Hubbert, M.K. and Rubey, W.W., 1959. Role of fluid pressure in mechanics of overthrust faulting: 1. Mechanics of fluid filled porous solids and its application to overthrust faulting. Geological Society of America Bulletin, 70: 115 - 166.

Huhn, K., 2001. Analyse der Mechanik des Makran Akkretionskeils mit Hilfe der Finiten und der Diskreten Elemente Methode sowie analoger Sandexperimente, Geoforschungszentrum Potsdam.

Huhn, K., Kock, I. and Kopf, A., 2006. Comparitve numerical and analogue shear box experiments and their implications for the mechanics along the failure plane of landslides. Norwegian Journal of Geology, 86(3): 209-220.

Itasca, 2004. PFC 2D 3.1 Manual. Itasca Consulting Group, Inc., Minneapolis.

Iverson, N.R., Baker, R.W. and Hooyer, T., 1997. A ring-shear device for the study of till deformation: Tests on tills with contrasting clay contents. Quaternary Science Research, 16: 1057-1066.

Jaeger, H.M., Nagel, S.R. and Behringer, R.P., 1996. Granular solids, liquids and gases. Reviews of Modern Physics, 68(4): 1259-1273.

Jensen, R.P., Bosscher, P.J., Plesha, M.E. and Edil, T.B., 1999. DEM Simulation of granular media - structure interface: effects of surface roughness and particle shape. International Journal for Numerical and Analytical Methods in Geomechanics, 23: 531-547.

Knuth, M., Marone, C. and Kirby, B., in press. Friction of sheared granular layers: the role of particle dimensionality, surface roughness, and material properties. Geochemistry, Geophysics, Geosystems.

Kock, I. and Huhn, K., 2006. Influence of particle shape on the frictional strength of sediments - a numerical case study. Sedimentary Geology, doi:10.1016/j.sedgeo.2006.07.011.

Kopf, A. and Brown, K.M., 2003. Friction experiments on saturated sediments and their implications for the stress state of the Nankai and Barbados subduction thrusts. Marine Geology, 202(3-4): 193-210.

Köster, H.M. and Schwertmann, U., 1993. Beschreibung einzelner Tonminerale. In: K. Jasmund, Lagaly, G. (Editor), Tonminerale und Tone: Struktur, Eigenschaften, Anwendung und Einsatz in Industrie und Umwelt. Steinkopff, Darmstadt, pp. 490.

Koyi, H., 1997. Analogue Modelling: From a qualitative to a quantitative technique - a historical outline. Journal of Petroleum Geology, 20(2): 223-238.

Krantz, R.W., 1991. Measurements of friction coefficients and cohesion for faulting and fault reactivation in labratory models using sand and sand mixtures. Tectonophysics, 188(1-2): 203-207.

Kuhn, M.R., 2003. An experimental method for determining the effects of strain gradients in a granular material. Communications in Numerical Methods in Engineering: 573 - 580.

Labaume, P. et al., 1997. Scaly fabrics in sheared clays from the décollement zone of the Barbados accretionary prism. In: T.H. Shipley, Y. Ogawa, P. Blum and J.M. Bahr (Editors), Proc. ODP, Sci. Results, College Station, TX (Ocean Drilling Program), pp. 59-78.

Lagaly, G. and Köster, H.M., 1993. Tone und Tonminerale. In: K. Jasmund, Lagaly, G. (Editor), Tonminerale und Tone: Struktur, Eigenschaften, Anwendung und Einsatz in Industrie und Umwelt. Steinkopff, Darmstadt, pp. 490.

Lambe, T.W. and Whitman, R.V., 1969. Soil mechanics. Series in Soil Engineering. John Wiley & Sons, Inc., New York, 553 pp.

Leeder, M., 1999. Sedimentology and Sedimentary Basins - From turbulence to tectonics. Blackwell Publishing, Oxford, 608 pp.

Liu, H.H., Kou, S.Q., Lindqvist, P.-A. and Tang, C.A., 2004. Numerical studies on the failure process and associated microseismicity in rock under triaxial compression. Tectonophysics, 384(1-4): 149-174.

Liu, S.H., Sun, D.A. and Wang, Y., 2003. Numerical Study of soil collapse behaviour by discrete element modelling. Computers and Geotechnics, 30(5): 399-408.

Lockner, D.A. and Beeler, N.M., 2002. Rock failure and Earthquakes. In: W. Lee, Kanamori, H., Jennings, P., Kisslinger, C. (Editor), International handbook of earthquake and engineering seismology. International Geophysics. Elsevier, pp. 1200.

Logan, J.M., Friedman, M., Higgs, N., Dengo, C. and Shimanoto, T. (Editors), 1979. Experimental studies of simulated fault gouge and their application to studies of natural fault zones. Proc. Conf. VIII - Analysis of Actual fault zones in bedrock US Geol. Surv. Open-file Report 79-1239.

Logan, J.M. and Rauenzahn, K.A., 1987. Frictional dependence of gouge mixtures of quartz and montmorillonite on velocity, composition, and fabric. Tectonophysics, 144(1-3): 87-108.

Lohrmann, J., Kukowski, N., Adam, J. and Oncken, O., 2003. The impact of analogue material properties on the geometry, kinematics, and dyncamics of convergent sand wedges. Journal of Structural Geology, 25: 1691-1711.

Loseth, T.M., 1999. Submarine Massflow Sedimentation, Berlin. Springer Verlag, 156 pp.

Lupini, J.F., Skinner, A.E. and Vaughan, P.R., 1981. The drained residual strength of cohesive soils. Geotechnique, 31(2): 181-213.

Mair, K., Frye, K.M. and Marone, C., 2002. Influence of grain characteristics on the friction of granular shear zones. Journal of Geophysical Research, 107(B10): 2219, doi:10.1029/2001JB000516.

Maltman, A., 1994a. Deformation structures preserved in rocks. In: A. Maltman (Editor), The geological deformation of sediments. Chapman & Hall, London, pp. 392.

Maltman, A. (Editor), 1994b. The geological deformation of sediments. Chapman & Hall, London, 362 pp.

Maltman, A., Labaume, P. and Housen, B., 1997. Structural geology of the décollement at the toe of the Barbados accretionary prism. In: T.H. Shipley, Y. Ogawa, P. Blum and J.M. Bahr (Editors), Proc. ODP, Sci. Results, College Station, TX (Ocean Drilling Program), pp. 279-292.

Marone, C., 1998. Laboratory-derived friction laws and their application to seismic faulting. Annual Review of Earth and Planetary Sciences, 26: 643-696.

Marone, C. and Cox, S.J.D., 1994. Scaling of Rock Friction Constitutive Parameters: The Effects of Surface Roughness and Cumulative Offset on Friction of Gabbro. Pure and Applied Geophysics, 143(1/2/3): 61-87.

Marone, C., Hobbs, B.E. and Ord, A., 1992. Coulomb Constitutive Laws for Friction: Contrasts in Frictional Behaviour for Distributed and Localized Shear. Pure and Applied Geophysics, 139(2): 195-214.

Marone, C., Raleigh, C.B. and Scholz, C.H., 1990. Frictional Behaviour and Constitutive Modelling of Simulated Fault Gouge. Journal of Geophysical Research, 95(B5): 7007 - 7025.

Marone, C., Saffer, D.M., Frye, K.M. and Mazzoni, S., 2001. Laboratory results indicating intrinsically stable frictional behaviour of illte clay. EOS Trans. AGU (Supplement), 82(47): 1248 - 1249.

Matthes, S., 1983. Mineralogie. Springer Verlag, Berlin, 461 pp.

Means, W.D., 1976. Stress and Strain. Springer Verlag, New York, 338 pp.

Mindlin, R.D. and Deresiewics, H., 1953. Elastic spheres in contact under varying oblique forces. Journal of Applied mechanics, 20: 327-344.

Mitchell, J.K. and Soga, K., 2005. Fundamentals of Soil Behaviour. John Willey & Sons, Hoboken, New Jersey, 577 pp.

Moore, D.E. and Lockner, D.A., 2004. Crystallographic controls on the frictional behaviour of dry and water-saturated sheet structure minerals. Journal of Geophysical Research, 109(B03401): doi::10.1029/2003JB002582.

Moore, J.C. and Saffer, D.M., 2001. Updip limit of the seismogenic zone beneath the prism of southwest Japan: An effect of diagenetic to low-grade metamorphic processes and increasing effective stress. Geology, 29: 183 - 186.

Mora, P. and Place, D., 1994. Simulation of the Frictional Stick-Slip Instability. Pure and Applied Geophysics, 143(1/2/3): 61-87.

Mora, P. and Place, D., 1998. Numerical simulation of earthquake faults with gouge: toward a comprehensive explanation for the heat flow paradox. Journal of Geophysical Research, 103(B9): 21067 - 21089.

Morgan, J.K., 1999. Numerical simulations of granular shear zones using the distinct element method 2. Effects of particle size distribution and interparticle friction on mechanical behaviour. Journal of Geophysical Research, 104(B2): 2721-2732.

Morgan, J.K. and Boettcher, M.S., 1999. Numerical simulations of granular shear zones using the distinct element method 1. Shear zone kinematics and the micromechanics of localization. Journal of Geophysical Research, 104(B2): 2703-2719.

Morrow, C.A., Moore, D.E. and Lockner, D.A., 2000. The effect of mineral bond strength and adsorbed water on fault gouge frictional strength. Geophysical Research Letters, 27(6): 815-818.

Morrow, C.A., Radney, B. and Byerlee, J., 1992. Frictional Strength and the Effective Pressure Law of Montmorillonite and Illite Clays. In: B.a.W. Evans, T. (Editor), Fault mechanics and transport properties of rocks; a festschrift in honor of W. F. Brace. Academic Press, San Diego, pp. 524.

Mueth, D.M. et al., 2000. Signatures of granular microstructure in dense shear flows. Nature, 406: 385-389.

Müller-Vonmoss, M. and Kohler, E.E., 1993. Geotechnik und Entsorgung. In: K. Jasmund, Lagaly, G. (Editor), Tonminerale und Tone: Struktur, Eigenschaften, Anwendung und Einsatz in Industrie und Umwelt. Steinkopff, Darmstadt, pp. 490.

Mulugetta, G., 1988. Modelling the geometry of Coulomb thrust wedges. Journal of Structural Geology, 10: 847 - 859.

Ng, T.-T., 1994. Numerical simulations of granular soil using elliptical particles. Computers and Geotechnics, 16: 153-169.

Ng, T.-T., 2004. Shear strength of assemblies of ellipsoidal particles. Géotechnique, 54(10): 659-669.

Oda, M. and Iwashita, K., 1999. Mechanics of Granular Materials. A. A. Balkema, Rotterdam/Brookfield, 383 pp.

Persson, B.N.J., 1998. Sliding Friction: Physical Principles and Applications. Nanoscience and Technology. Springer, Berlin Heidelberg, 462 pp.

Place, D. and Mora, P., 2000. Numerical Simulation of Localization Phenomena in a Fault Zone. Pure and Applied Geophysics, 157(1821 - 1845).

Radjai, F., Wolf, D.E., Jean, M. and Moreau, J.-J., 1998. Bimodal Chracter of Stress Transmission in Granular Packings. Physical Review Letters, 80(1): 61 - 64.

Riedel, W., 1929. Zur Mechanik geologischer Brucherscheinungen. Zentrallblatt für Geologie, Mineralogie und Paläontologie, 1929B: 354-368.

Rothenburg, L. and Bathurst, R.J., 1992a. Effects of particle shape on the micromechanical behaviour of granular materials. In: H.H. Shen, Satake, M., Mehrabadi, M., Chang, C. S., Campbell, C. S. (Editor), Advances in Micromechanics of Granular Materials. Elsevier, Potsdam, NY, USA, pp. 462.

Rothenburg, L. and Bathurst, R.J., 1992b. Micromechnical features of granular assemblies with planar elliptical particles. Géotechnique, 42(1): 79-95.

Rothenburg, L. and Bathurst, R.J., 1993. Influence of particle eccentricity on micromechanical behaviour of granular material. Mechanics of Materials, 16: 141-152.

Rutter, E.H., Maddock, R.H., Hall, S.H. and White, S.H., 1986. Comparative Microstructures of Natural and Experimentally Produced Clay-Bearing Fault Gouges. Pure and Applied Geophysics, 124: 3-30.

Saffer, D.M., Frye, K.M., Marone, C. and Mair, K., 2001. Laboratory results indicating complex and potentially unstable frictional behavior of smectite clay. Geophysical Research Letters, 28(12): 2297-2300.

Saffer, D.M. and Marone, C., 2003. Comparison of smectite- and illite-rich gouge frictional properties: application to the updip limit of the seismogenic zone along subduction megathrusts. Earth and Planetary Science Letters, 25(1-2): 219-235.

Sammis, C.G. and Biegel, R.L., 1989. Fractals, Fault-Gouge and Friction. Pure and Applied Geophysics, 131(1/2): 255-271.

Sammis, C.G., King, G. and Biegel, R.L., 1987. The kinematics of gouge deformation. Pure and Applied Geophysics, 125(5): 777-812.

Sammis, C.G., Osborne, R.H., Anderson, J.L., Banerdt, M. and White, P., 1986. Self-Similar Cataclasis in the Formation of Fault Gouge. Pure and Applied Geophysics, 124(1/2): 53-78.

Sammis, C.G. and Steacy, S.J., 1994. The Micromechanics of Friction in a Granular Layer. Pure and Applied Geophysics, 142(3/4): 777-794.

Scholz, C.H., 1998. Earthquakes and friction laws. Nature, 391(1): 37 - 42.

Scholz, C.H., 2002. The mechanics of Earthquakes and Faulting. Cambridge University Press, Cambridge, 471 pp.

Schöpfer, M.P.J., Childs, C. and Walsh, J.J., 2006. Localization of normal faults in multilayer sequences. Journal of Structural Geology, 28(5): 816-833.

Scott, D.R., Marone, C. and Sammis, C.G., 1994. The apparent friction of granular fault gouge in sheared layers. Journal of Geophysical Research, 99(B4): 7231-7246.

Solheim, A., Berg, K., Forsberg, C.F. and Bryn, P., 2005. The Storegga slide complex: repetitive large sliding with similar cause and development. Marine and Petroleum Geology, 22: 97 - 108.

Sperrevik, S., Faerseth, R.B. and Gabrielsen, R.H., 2000. Experiments on clay smear along faults. Petroleum Geoscience, 6(2): 113-123.

Stöcker, H. (Editor), 1994. Taschenbuch der Physik. Verkag Harri Deutsch, Frankfurt am Main, 874 pp.

Strasser, M. et al., in press. Quantifying subaqueous slope stability during seismic shaking: Lake Lucerne as model for ocean margins. Marine Geology.

Strayer, L.M. and Suppe, J., 2002. Out-of-plane motion of a thrust sheet during along-strike propagation of a thrust ramp: a distinct-element approach. Journal of Structural Geology, 24(4): 637-650.

Takizawa, S. and Ogawa, Y., 1999. Diltant clayey microstructure in the Barbados décollment zone. Journal of Structural Geology, 21: 117-122.

Terzaghi, K., 1925. Erdbaumechanik. Franz Deuticke, Vienna.

Thornton, C., 2000. Numerical simulation of deviatoric shear deformation of granular media. Geotechnique, 50(1): 43-53.

Tucker, M.E., 1981. Sedimentary Petrology. Geoscience Texts, 3. Blackwell Scientific Publications, Oxford, 252 pp.

Vanucchi, P., Maltman, A., Bettelli, G. and Clennell, B., 2003. On the nature of scaly fabric and scaly clay. Journal of Structural Geology, 25: 673-688.

Varnes, D.J., 1978. Slope movement types and processes. In: R.L. Schuster and R.J. Krizek (Editors), Landslides: Analysis and Control. National Academy of Sciences, pp. 12-33.

Wang, W. and Scholz, C.H., 1994. Wear processes during frictional sliding of rock. Journal of Geophysical Research, 99(B4): 6789 - 6799.

Weltje, G.J. and Prins, M.A., 2003. Muddled or mixed? Inferring paleoclimate from size distributions of deep-sea clastics. Sedimentary Geology, 162: 39-62, doi:10.1016/S0037-0738(03)00235-5.

Wessel, P. and Smith, W.H.F., 1991. Free software helps map and display data. EOS Trans. AGU, 72: 441.

Zhou, Y.C., Xu, B.H., Yu, A.B. and Zulli, P., 2002. An experimental and numerical study of the angle of repose of coarse spheres. Powder Technology, 125(1): 45-54.

Acknowledgements

I would not have been able to complete this thesis without the support and help from many people.

Above all, I would like to thank Prof. Dr. K. Huhn who gave me the chance to do this thesis. Thank you for the support and the lively discussions, a considerable amount of advice and constructive suggestions, but also enough freedom to find my own way during the last three and a half years.

I am very grateful to Prof. Dr. A. Kopf for fruitful discussions and suggestions concerning my manuscripts, for collaborating on one manuscript, for readily agreeing to be second reviewer for this thesis and, of course, a nice POS336 cruise.

I owe many thanks to Dr. M. Seyferth who, at the beginning of this work, got me on the right track with PFC2D.

I would like to thank all my colleagues from the Geosciences Department and the Research Center Ocean Margins who provided answers to my questions and who are interested in sediment mass transport processes: Sebastian Krastel, Till Hanebuth, Matthias Lange, Silvia Stegmann, Jan-Berend Stuut and all the other ‘slopers’.

Many thanks to all my friends, colleagues and fellow Ph.D. students: Johanna Schwarz, Stephan Steinke, Sebastian Müller, Sven & Ole Frehers, Melanie Reichelt, Frank Strozyk, Xin Li, Carola Ott, Astrid Laupichler and, of course, my favourite flatmate Linus Müller.

Funding was provided by the Deutsche Forschungsgemeinschaft via the Research Center Ocean Margins (RCOM).

Thanks to my parents who supported me all along.

This thesis is dedicated to my wife, Bettina Kock.

Appendix

A. The Discrete Element Method

The Discrete Element Method (DEM) is a numerical modelling technique based upon description of granular materials. It was developed by Cundall and Strack (1978) and further enhanced and modified by Cundall and Strack (1979; 1983), Cundall (1989). To date, other numerical approaches to model granular assemblies exist (Oda and Iwashita, 1999). However, in this study the current 2D version of the numerical code originally developed by Cundall and Strack (1978 is used. The code is called Particle Flow Code, PFC2D 3.1, and is distributed by Itasca, Inc. (Itasca, 2004).

A material modelled by PFC2D consists of numerous circular, 2-dimensional particles. Between these particles contacts may exist and particles interact according to simple laws between their respective contacts. There are basically two laws which are applied: (1) The force-displacement law is applied to each contact between particles. (2) The law of motion is applied to each particle. These two numerical laws represent a calculation cycle which is executed at each timestep in the model, beginning with the force-displacement law. The complete procedure is described in the following sections. When not cited otherwise, all information of sections A.1 to A.8 are from Cundall and Strack (1978; 1979; 1983), Cundall (1989) and Itasca (2004).

A.1 Particle properties

Each particle has a finite set of properties assigned. These properties govern the interaction between particles according to the laws described in the later sections. At the same time, each particle has derived properties which are calculated from these laws. Assigned properties of particles are the normal stiffness K_N, the shear stiffness k_S, particle coefficient of friction $\mu_{(P)}$, initial position $\vec{p}$, particle radius $r_{(P)}$ and a density ρ. The derived properties and how they are calculated is described in the next two sections.

A.2 The force-displacement law

The force-displacement law describes the relation between forces acting on the contact between particles to resulting displacement due to these forces.

The force calculation between two particles utilizes a soft-contact approach, which means that particles are allowed to overlap one another at particle contacts. In Fig. 1a, a contact between two balls is shown. The amount of overlap ΔD is scaled by shear and normal stiffnesses of both balls. It is important to note that there is a difference between the overlaps calculated for

normal and shear forces. For normal force calculation the complete overlap ΔD is used. Note that in the following equations (a1 –a4) force magnitudes are calculated. Then, the normal force between contacts can be calculated by

(a1) $F_N = K_N \Delta D_N$.

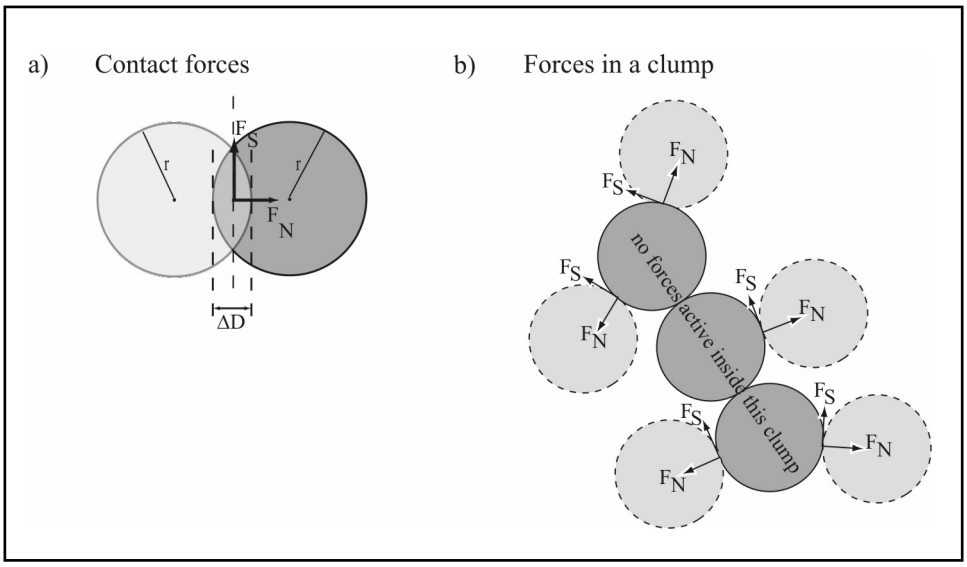

Fig. 1 Forces between DEM particles. a) Forces between two adjacent particles are scaled by overlap. b) Forces inside a 'clump' are nor calculated, while forces acting on a 'clump' from outside are not affected and thus are computed.

The shear force is calculated in a similar fashion. However, shear forces can add up when the contact still exists after one calculation cycle. Therefore, shear force has to be calculated incrementally. Hence, the overlap has also to be calculated incrementally, as the difference of overlap between two timesteps. The difference of overlap between two timesteps depends on shear velocity v_S, so that

(a2) $\Delta D_S = \frac{v_S}{dt}$.

Then, shear force increment can be calculated with:

(a3) $\Delta F_S = k_S \Delta D_S$.

Total shear force, then simply is computed by adding shear force increment to the existing shear force from the previous timestep:

(a4) $F_S = F_S + \Delta F_S$.

Furthermore, at each contact the normal and shear forces also have a direction. Thus, a force vector consisting out of normal and shear components exists, which represents all single forces resulting from all contacts:

(a5) $F_i = F_{N,i} + F_{S,i}$

where the index *i* refers to right-handed Cartesian coordinate system axes.

This force vector then can be applied to a particle. The force and moment applied to a particle *P* resulting from *n* contacts of other particles can be expressed as

(a6) $F_{(P),i} = \sum_n F_i$ and

(a7) $M_{(p),i} = \sum_n F_{S,i} * r_{(p)}$.

A.3 The law of motion

The resulting force vector from the force-displacement law has to be applied to a particle with a motion law. This law relates forces to translational and rotational particle displacement. For translational motion the governing equation is Newton's second law:

(a8) $F_{(P),i} = m(\ddot{x}_i - g_i)$,

where m is the total mass of the particle and g_i are body accelerations, e.g. gravity. After solving for acceleration $\ddot{x}_i$, velocity $\dot{x}_i$ can be computed easily by integrating over a given, finite timestep dt. The calculation of dt is presented in section A.5.

The solution for rotational motion is equally simple. The governing equation is:

(a9) $M_{(P),i} = I_i \dot{\omega}_i$.

Here, I_i are the moments of inertia and $\dot{\omega}_i$ the angular accelerations. Solving for $\dot{\omega}_i$ and integrating over timestep dt gives angular velocity ω_i.

The resulting velocities are applied to each particle. After that, particle positions are updated. Thus, contacts are broken and newly build and the calculation cycle begins anew with the force-displacement law.

A.4 The slip condition

As shown in eq. (a4), shear forces F_S accumulate at each particle contact. To model real materials, at some point the particles must be allowed to slip past one another. This is done via a slip condition. The used slip condition resembles the Mohr-Coulomb criterion for cohesionless soils:

(a10) $F_{S,\max} = \mu_{\min,(P)} \left| F_{N,i} \right|$.

$F_{S,\max}$ is the maximum allowable shear force at a contact point and $\mu_{\min,(P)}$ the minimum particle coefficient of friction of the two particles. When $F_S > F_{S,\max}$, slip is allowed to occur.

A.5 Time step determination and damping

For the integration scheme in section A.3 a timestep dt has to be computed. The timestep has to be chosen in such a way that the force-displacement law and the law of motion can only be applied once to all particles during one calculation cycle. The critical timestep is the minimum of

$$dt = t_{crit} = \left\{ \begin{matrix} \sqrt{m / k_{trans}} \\ \sqrt{I / k_{rot}} \end{matrix} \right\}. \quad \text{(a11)}$$

Here, m and I are mass and moment of inertia, respectively and k_{trans} and k_{rot} denote translational and rotational stiffness, which have to be computed separately.

Without any damping force, such an elastic DEM model would oscillate. To prevent this, a damping force which scales with acting particle force is applied to the force of each particle.

A.6 Clump principle

In PFC2D single particles can be combined to produce a cluster of particles. These clusters are termed clumps. Clumps are rigid, which means that particles belonging to a clump can not move relative to each other and contact forces between them are not calculated (Fig. 1b). Therefore, it is possible for particles of a clump to overlap. Contacts with particles not belonging to the clump are not affected, so forces in this case are calculated (Fig 1b).

The properties of the single particles comprising a clump are incorporated into a clump. This includes for example simple properties like mass and centre of mass. However, moments and products of inertia and the equations of motion have to be modified for a clump (see Itasca, 2004 for more details).

A.7 Stress calculation

To calculate stress in a particle assembly, two steps are necessary: (1) Compute each particle's stress tensor and (2) compute stress in the assembly with a meaningful averaging procedure.

The stress tensor $\sigma_{ij}^{(P)}$ for a particle *(P)* depends on the location $x_i^{(C)}$ and magnitude $F_j^{(C)}$ acting at all contact points N_C of the particle:

$$\sigma_{ij}^{(P)} = -\frac{1}{V^{(P)}} \sum_{Nc} x_i^{(C)} F_j^{(C)}, \quad \text{(a12)}$$

where $V^{(P)}$ is the volume of the particle and indices *i,j* are 2D directions.

The average stress tensor $\sigma_{ij}^{(M)}$ in a particle assembly can be found by integrating all particle stress tensors over defined volume *V* with:

(a13) $\sigma_{ij}^{(M)} = \frac{1}{V}\int_V \sigma_{ij}^{(P)} dV$.

This integral can be replaced by a sum over all particles inside this volume, since stress in a granular material exists only in particles; the volume increment *dV* then becomes particle volume $V^{(P)}$:

(a14) $\sigma_{ij}^{(M)} = \frac{1}{V}\sum_{Np} \sigma_{ij}^{(P)} V^{(P)}$,

where N_P is the number of particles. This expression is the same as in Chapter IV where the quotient $\frac{1}{V}$ is expressed with $\frac{1-v}{\sum_n V^{(P)}}$, where *v* is porosity.

Both expressions are used for stress calculation in the manuscripts.

A.8 List of symbols used

F : force; in [N]

L : load; in [N]

σ_N : normal stress; in [Pa]

σ_c : critical normal stress; in [Pa]

$\sigma_{N,(M)}$,

$\sigma_N{}^{(M)}$: macroscopic normal stress acting on particle assemblage; in [Pa]

σ'_N : effective normal stress; in [Pa]

p_w : pore pressure; in [Pa]

Δu: excess pore pressure; in [Pa]

τ : shear stress; in [Pa]

τ_c, τ_{crit} : critical shear stress; in [Pa]

τ_0 , C: cohesion; in [Pa]

$\tau_{(M)}$, $\tau^{(M)}$: macroscopic shear stress acting on particle assemblage; in [Pa]

ΔA : area, here: area of real contact; in [m²]

e sphericity; dimensionless

ϕ : friction angle; in degree [°]

μ , μ_C : coefficient of friction; dimensionless

$\mu_{(M),interior}$,

$\mu_{(M)}$, $\mu^{(M)}$: overall, macroscopic coefficient of friction of particle assembly; dimensionless

$\mu_{(M),basal}$: macroscopic coefficient of friction of shear box walls; dimensionless

$\mu_{(P)}$, μ_P: coefficient of friction of an individual grain or particle; dimensionless

$\Delta\mu_{(P)}$: particle coefficient of friction contrast; dimensionless

$\overline{\sigma}_{ij}^{(M)}$ average stress tensor of defined volume in particle assembly; i,j = 1,2

$\sigma_{(p),ij}$ stress tensor for a single particle; i,j = 1,2

$V_{(P)}$ particle volume; in [m³]

δV normalized volume strain; dimensionless

V instantaneous volume of particle assembly; in [m³]

V_0 initial volume of particle assembly; in [m³]

$\delta\nu$ normalized porosity change; dimensionless

ν instantaneous 2D porosity of defined volume in particle assembly; in [m³]

ν_0 initial 2D porosity of defined volume in particle assembly; in [m³]

R_1, R_2,P,

Y, X : shear plane geometry after Logan et al. (1979) and Riedel (1929)

$F_{(P),N,S}$ interparticle force; normal and shear; in [N]

$k_{(P),N,S}$ particle stiffness; normal and shear; in [N/m]

$\Delta D_{N,S}$ particle overlap, normal and shear; in [m]

$F_{(P),Net}$ total net force acting on one particle; in [N]

$M_{(P),Net}$ total net moment acting on one particle; in [Nm]

$m_{(P)}$ particle mass; in [kg]

$I_{(p)}$ particle moment of inertia; in [kgm²]

$\ddot{x}$ translational acceleration; in [m/s²]

$\dot{\omega}$ rotational acceleration; in [rad/s²]

dt timestep; in [s]

$\rho_{(P)}$ particle density; in [kg/m³]

n particle number; dimensionless

F_{smax} maximum shear force; in [N]